Advances in Natural Quasicrystals and Quasicrystal Tilings

Chaney C. Lin

A Dissertation
Presented to the Faculty
of Princeton University
in Candidacy for the Degree
of Doctor of Philosophy

Recommended for Acceptance
by the Department of
Physics
Advisers: L. S. Hollister, P. J. Steinhardt, & S. Torquato

June 2017

Abstract

The first part of this dissertation reports recent progress on natural quasicrystals. We present new evidence from a fragment of the quasicrystal-bearing CV3 carbonaceous chondritic meteorite Khatyrka that shows cross-cutting relationships and redox reaction between Al-Cu-bearing alloys and silicate phases. The new evidence establishes that the Al-Cu-bearing alloys (including quasicrystals) formed in outer space during a complex, multi-stage process. Some Al-bearing grains (including some quasicrystals) formed as a direct result of an impact in space a few 100 Ma. Most other Al-bearing grains (including quasicrystals) existed prior to the impact and thus formed in space at an earlier time. We also present the discovery of two new quasicrystals, including a second distinct Al-Cu-Fe icosahedral phase in Khatyrka—the first quasicrystal found in nature prior to discovery in the lab—and a synthetic Al-Fe-Cu-Cr-Ni icosahedral phase—the first quasicrystal to be synthesized in a laboratory shock experiment.

In the second part of this dissertation, we explore how different local isomorphism (LI) classes of quasicrystals vary in their structural and physical properties. We examine the continuum of LI classes of pentagonal quasicrystal tilings obtained by direct projection from a five-dimensional hypercubic lattice.

Our initial focus is on hyperuniformity, the suppression of long-wavelength density fluctuations relative to typical structurally disordered systems. We study how the degree of hyperuniformity [$\overline{\Lambda}(\infty)$] depends on LI class. The results show that $\overline{\Lambda}(\infty)$ is dominantly determined by the local distribution of vertex environments, and also exhibits a non-negligible dependence on the restorability. Among the pentagonal quasicrystal tilings, the Penrose tiling is the most hyperuniform [smallest $\overline{\Lambda}(\infty)$]. The difference in the degree of hyperuniformity is expected to affect physical characteristics, such as transport properties.

We then turn to a study of photonic quasicrystal heterostructures derived from the continuum of pentagonal quasicrystal tilings. We demonstrate that, with the

exception of the Penrose LI class, all other LI classes result in degenerate, effectively localized states, with precisely predictable and tunable properties (frequencies, frequency splittings, spatial configurations). A relationship between the degeneracy of these states and the number of certain vertex environments is discussed, and potential applications for these states are described.

Acknowledgements

I first wish to thank my advisers: I thank Paul Steinhardt for taking me in as his student and putting up with me over the years, for being an incredible colleague and friend and tireless defender on my behalf, and for his enlightened wisdom, endless patience, and sense of humor. I thank Lincoln Hollister for supporting me in research and in life, for being an amazing mentor to me and to Paul, for never failing to make me laugh even in the most challenging of times, for wonderful conversations about everything under the sun, for letting me squat in his outer office before he was kicked out to the other side of the hall, and for always bringing me staff-meeting cookies. I thank Sal Torquato for the guidance, feedback, and expertise provided throughout the research process, for playing such an important role in the expeditious handling of the JPCM paper, for always having puns at the ready, and for making a fruitful nickel wager with Paul. I thank Luca Bindi for his boundless enthusiasm, for his ability to find new minerals, and for miraculously calling in to meetings even when severely injured or hospitalized.

I thank Marian Florescu for guiding and mentoring me from afar, Dan Marlow for graciously serving on my committee, and Angela, Anthony, Barbara, Jessica, Kate, and the rest of the Physics Department staff for keeping me informed of deadlines, processing reimbursements, and maintaining and running Jadwin Hall.

I thank those who have contributed to work presented in this thesis: Glenn MacPherson, Chi Ma, Chris Andronicos, Paul Asimow, Oliver Tschauner, and the Chukotka expedition team. For beneficial conversations and technical help, thanks to Nan Yao, John Schreiber, Fan Wu, Jerry Poirier, Andrew Higgins, Ruth Aronoff, David Huse, Ge Zhang, JaeUk Kim, Erdal Oguz, Duyu Chen, Ian Cosden, Robert Knight, David Luet, Josko Plazonic, and the CSES team.

For various modes of support, I especially thank Bin, Bo, Cheng, Elliot, Huan, Jake, Jeff, Jimmy and Nancy, Jun, Kenan and Lauren, Ling, Marc, Matt, Rick, Scott,

Siwei, and Yu. For always being honest, open-minded, and reliable, I thank Akshay, Bobby, Liangsheng, Vedika and David, and Hue-Sun. For welcoming me into their lives and making me feel like family, I thank Shaomei and Charles; Poker, Hsinwei, Shihan, Meiying, and Hubert; Lotus, Rui, and Dajun; Olga; Noah, Lyn, and Ivor; Lea and Daniel.

Finally, for their unconditional love, I thank Mom and Dad, Sunny, Uncle Paul and Aunt Jane, Goose, Snowman, and Engelbert.

To Engelbert,

for teaching me what truly matters.

Advances in Natural Quasicrystals and Quasicrystal Tilings

List of Tables

List of Figures

Chapter 1

Introduction

1.1 Shechtman's Al-Mn alloy

The field of crystallography was forever changed in 1984, when Dan Shechtman and his colleagues reported the observation of an unusual diffraction pattern from a grain of a rapidly quenched Al-Mn alloy [1]. The diffraction pattern consisted of sharp spots arranged with icosahedral point group symmetry, which consists of six independent axes of five-fold rotational symmetry, ten of three-fold symmetry, and fifteen of two-fold symmetry.

At the time, solid-state materials were predominantly categorized as either crystalline or amorphous. A crystalline material can be described as the perfect space-filling repetition of a suitably decorated unit cell, with a diffraction pattern that is composed of sharp, delta-function ("Bragg") peaks. An amorphous material can be described as a random arrangement of some basic set of units (e.g., atoms, molecules, tiles), with a diffraction pattern that consists of broad, diffuse rings.

While the diffraction pattern of Shechtman's Al-Mn alloy had sharp spots indicative of crystals, its icosahedral symmetry was not a permissible crystallographic

point group symmetry. Only one-, two-, three-, four-, and six-fold axes are allowed in crystals; the observed five-fold axes are forbidden [2].

Thus, Shechtman's Al-Mn alloy appeared to be neither amorphous nor crystalline. This created immense intrigue among the solid state and materials science communities, with everyone wondering: *Is this a new state of matter*?

1.2 Three models for the Al-Mn alloy

There were three leading models that were proposed to describe and understand the new observations.

One model, suggested by Dan Shechtman and Ilan Blech and further developed by Peter Stephens and Alan Goldman, is the "icosahedral glass" model [3, 4]. An icosahedral glass is a dense random packing of icosahedra connected to one another vertex-to-vertex. Starting with one icosahedron, additional icosahedra are attached, one at a time, to a randomly chosen vertex, such that the icosahedra never overlap. The icosahedra represent atomic clusters that have local icosahedral symmetry. The resulting diffraction pattern (using the point pattern obtained by placing points on the vertices) for the icosahedral glass has icosahedral symmetry and sharp diffraction peaks with finite width.

A second model (or set of models) is based on standard ideas in crystallography. One possibility is that the Al-Mn alloy is a crystal with a large unit cell. The atomic basis would consist of thousands of atoms that are arranged with near-icosahedral symmetry [5]. Another possibility is that the alloy is a multiple-twinned crystal, with crystallites made of icosahedral clusters [5, 6, 7]. The most notable and most vocal proponent for explaining the peculiar alloy as a complex crystal was Linus Pauling.

Finally, there is the model proposed by Paul Steinhardt and his student Dov Levine [8], which explains that the alloy is a new solid state of matter that they

called the "quasicrystal state", the theory of which they had been developing since 1981, before the Al-Mn pattern was observed [9]. A quasicrystal can be seen as a space-filling arrangement of two or more fundamental repeating units (e.g., tiles, atoms, molecules), with the arrangement exhibiting long-range orientational order and quasiperiodic translational order [10, 11, 12, 13]. The diffraction pattern of a quasicrystalline point pattern is composed of a dense set of Bragg peaks, arranged with a crystallographically forbidden point group symmetry. Quasicrystals are generalizations of the Penrose tiling in two-dimensions [14].

1.3 Thermodynamically stable quasicrystal

All of these models could produce the icosahedral pattern of Shechtman's Al-Mn alloy, so it remains debatable which one is best. However, in 1987, a discovery was made that decisively favored the quasicrystal model. An-Pang Tsai et al. [15] grew an Al-Cu-Fe phase with a diffraction pattern exhibiting icosahedral symmetry and resolution-limited peaks. The icosahedral phase was grown by conventional solidification, i.e., cooling an alloy melt at a rate of $\sim 10^{\circ}\mathrm{C\ h^{-1}}$ [16]. After heating, then annealing for two days, there were no other phases observed besides the icosahedral phase. Upon further heating, differential thermal analysis showed only one endothermic peak—corresponding to the latent heat of fusion at the melting point of the icosahedral phase—which indicated that the phase was stable and did not undergo any phase transitions until it melted. The phase was later shown to have composition $Al_{63}Cu_{24}Fe_{13}$ [17]. Based on the experimental evidence, the icosahedral phase synthesized by Tsai et al. is considered to be the first practically perfect quasicrystal that is thermodynamically stable at finite temperature. After this discovery, it was generally accepted that the quasicrystal model provided the simplest explanation

for Shechtman's icosahedral Al-Mn alloy. This culminated in Dan Shechtman being awarded the Nobel Prize in Chemistry "for the discovery of quasicrystals" in 2011.

Despite Tsai et al.'s discovery, quasicrystals continued to be viewed as a peculiar state of matter that could only be synthesized under highly controlled laboratory conditions. Though it was accepted that quasicrystals were thermodynamically stable at finite temperature, it was debatable whether quasicrystals were global minima in the energy landscape at low temperatures and, hence, ground states on the same footing as crystals. An entropic theory was proposed, based on random arrangements of tiles, in which the quasicrystalline state maximizes the entropy but is not the ground state [18]. There was support for this entropic viewpoint from the fact that, while several hundred more quasicrystals were discovered in the laboratory [13, 19], no natural specimen had been found, thus suggesting that quasicrystals are unstable over geologic time scales.

The opposing view was that quasicrystals can be ground states and as robust as crystals, and that nature may have already produced quasicrystals that man simply had not yet found or characterized. The discovery of such a specimen, at the very least, would indicate that quasicrystals are stable on geologic time scales and would point to exotic, previously unrecognized geological processes.

1.4 Natural quasicrystals

We now turn to an overview of the first study presented in this thesis. In Chapter 2, we report on the current status of the search for natural quasicrystals by the Princeton-Florence group led by Paul Steinhardt and Luca Bindi, including a history of the search in detail. The major events of the search are as follows: The search began in 1999 [9] and circuitously led to the discovery of the first natural quasicrystal (called "icosahedrite") in 2009 [20, 21], which was later determined to have originated from

the Khatyrka meteorite, a CV3 carbonaceous chondrite [22, 23]. Icosahedrite has the same composition and symmetry as the Al-Cu-Fe alloy synthesized by Tsai et al. in 1987 [15]

The occurrence of Al-Cu alloys in nature runs counter to all previously known stellar and geologic processes for two main reasons: (i) metallic Al is not expected to occur naturally because of its extremely strong affinity to oxygen, and (ii) Al and Cu are highly dissimilar in their cosmochemical properties and how they condense. Because of the difficulty in developing an explanation for how these alloys formed naturally, there have remained skeptics who believe that icosahedrite and the other Al-Cu alloys were produced by anthropogenic means, despite much evidence pointing to the contrary.

However, in Chapter 2, we present new evidence showing cross-cutting relationships and redox reactions between Al-Cu-Fe alloys and silicate melt. This new evidence firmly establishes that the Al-Cu-bearing alloys (including quasicrystals) formed in outer space during a complex, multi-stage process. The results also include the discovery of a second distinct icosahedral phase of Al-Cu-Fe that is the first quasicrystal found in nature prior to discovery in the lab. We also discuss a laboratory shock experiment that resulted in the first shock-induced synthesis of a quasicrystal.

Chapter 2 is based on work published in [24] (with Lincoln Hollister, Glenn MacPherson, Luca Bindi, Chi Ma, Chris Andronicos, and Paul Steinhardt)[1], [25] (with Chi Ma, Luca Bindi, and Paul Steinhardt)[1], [26] (with Luca Bindi, Chi Ma, and Paul Steinhardt)[1], and [27] (with Paul Asimow, Luca Bindi, Chi Ma, Oliver Tschauner, Lincoln Hollister, and Paul Steinhardt)[2].

[1]C.L. performed research and analyzed data in [24, 25, 26], led the writing of [24], and wrote parts of [25, 26].

[2]P.A. and P.S. designed the experiment reported in [27], motivated in part by results obtained by C.L. et al. that were later reported in [24]. P.A. and O.T. carried out the experiment. C.L. performed the initial survey studies of the run products by SEM and was advised by L.B., L.H., and P.S. During the survey studies, C.L. discovered Khatyrka-like features, as well as grains whose compositions had ratios of Al/Cu and Cu/Fe similar to those of known quasicrystals. The grains were observed to be quasicrystalline by EBSD (C.M.) and XRD (L.B.).

1.5 Local isomorphism classes of quasicrystals

There are uncountably many, physically distinct quasicrystals, which have the same symmetry, same fundamental repeating units (e.g., tiles, clusters of atoms or molecules), and same support for their diffraction patterns, but which have different space-filling arrangements of the repeating units and different peak intensities for their diffraction patterns [8, 10, 11, 12]. These distinct quasicrystals are said to belong to different *local isomorphism* (LI) *classes*.

In Chapters 3 and 4, we present two numerical studies of the continuous set of LI classes of pentagonal quasicrystal tilings obtained by direct projection from a five-dimensional hypercubic lattice. This set of tilings includes the Penrose tiling [14]. Chapter 3 is based on work published in [28] (with Paul Steinhardt and Salvatore Torquato)[3].

1.5.1 Degree of hyperuniformity

All quasicrystals—and hence all LI classes—have long-wavelength density fluctuations that, like crystals and special amorphous systems, are suppressed relative to typical structurally disordered systems (e.g., glasses and amorphous solids); this large-scale structural property is known as *hyperuniformity* [29, 30, 31]. Some measures of hyperuniformity have been observed to be correlated with physical properties, e.g., electromagnetic [32, 33], electronic [34], and mechanical [35]. Thus, it has been an open question of physical interest whether these measures of hyperuniformity vary with LI class.

In Chapter 3, we report that the degree of hyperuniformity, as measured by the leading coefficient of the number variance (defined in Section 3.2), does vary with LI class. Additionally, we report that among the continuum of LI classes studied, the Penrose LI class is the most hyperuniform. We further show that the degree of

[3]C.L. led the research and writing of [28].

hyperuniformity is dominantly determined by the local structure (e.g., by Voronoi areas) and has a subdominant contribution from the restorability of the LI class. The restorable LI classes, roughly speaking, contain a lower variance in their local neighborhoods than nearby LI classes. The results give us a better understanding of what determines the degree of hyperuniformity.

1.5.2 Photonic properties

In Chapter 4, we study the photonic properties of the continuum of LI classes associated with pentagonal quasicrystal tilings to determine if they differ from one another. Our results show that, with the sole exception of the Penrose LI class, all other LI classes result in degenerate, effectively localized states, with precisely predictable and tunable properties (frequencies, frequency splittings, and spatial configurations). We discuss a relationship between the degeneracy of these states and the number of certain vertex environments, as well as describe potential applications for these states.

Chapter 2

Natural quasicrystals

2.1 History of natural quasicrystals

2.1.1 Search beginnings

We begin by briefly reviewing the search for natural quasicrystals led by Paul Steinhardt and Luca Bindi, which is largely based on their own personal accounts of the events [9, 20, 36, 37, 38, 39, 40].

In 1999, Peter Lu, then a senior at Princeton University, began working with Paul Steinhardt, as well as Ken Deffeyes (Professor of Geosciences, Princeton University) and Nan Yao (Director of the Imaging and Analysis Center, Princeton University), on a systematic search for natural quasicrystals. They sifted through a database containing some 80,000 powder diffraction patterns, including over 9,000 patterns from natural samples [41]. To systematically search through the database for promising candidates, they constructed a novel metric that scored the powder patterns based on their similarity to patterns generated from ideal icosahedral quasicrystals. Known quasicrystals scored highly according to the metric. After the metric was computed for all of the patterns in the database, a few dozen promising candidates were identified. Samples from many of them were obtained and analyzed, but no new quasicrystals

were found. This was all reported in the 2001 paper by Lu et al. ([41]), which invited anyone interested in collaborating to contact Lu and Steinhardt.

The first response came six years later, in 2007, when Steinhardt was contacted by Luca Bindi, who was head of mineralogy at the Natural History Museum of the University of Florence in Italy. Bindi began going through rocks in the collection at the Florence museum, starting with candidates that had already been identified earlier in [41]. After a year, when nothing promising was found, the search was expanded beyond the catalogue to rocks that contained metals with compositions similar to those of known quasicrystals. The search soon focused on a sample labeled "khatyrkite". Khatyrkite itself is an Al-bearing alloy mineral ($CuAl_2$) that was first reported in 1985 and found in association with another Al-bearing alloy mineral, cupalite (CuAl). The holotype material (i.e., the specimen upon which the description and name of a new mineral is based) for both khatyrkite and cupalite is kept at the St. Petersburg Mining Institute. The sample labeled "khatyrkite" in the Florence museum (hereafter referred to as the "Florence sample") was not pure khatyrkite but, rather, a rock three millimeters in maximum dimension, which to the naked eye appeared to be a complex mineral assemblage containing silicates and metallic phases. The samples in Florence and St. Petersburg were the only two rocks known to contain khatyrkite and cupalite. The Florence sample had been acquired by the Florence museum in 1990 and had been catalogued as coming from "the Khatyrka region of the Koryak mountains in the Chukotka autonomous okrug on the north-eastern part of the Kamchatka peninsula" (i.e., the far north-eastern corner of Russia) [9, 36, 37, 38].

Thin sections of the Florence sample were prepared, and the chemical compositions of the constituent phases were analyzed with wavelength dispersive X-ray spectroscopy (WDS). The WDS studies confirmed that the sample contained grains of khatyrkite and cupalite. But there were also some unknown Al-Cu-Fe phases. The unknown phases were removed and analyzed by powder X-ray diffraction. One

scored highly according to the Lu-Steinhardt metric [41] and was prepared for study by transmission electron microscopy (TEM) to obtain a diffraction pattern. After much anticipation, finally, on New Year's Day 2009, Steinhardt and Yao analyzed a grain by TEM. The resulting diffraction pattern exhibited the same icosahedral symmetry as Tsai's Al-Cu-Fe alloy and Shechtman's Al-Mn alloy, but with virtually no phason strain. The result was a spectacular and unambiguous sign that the team had found a quasicrystal. The composition was measured and compared to a synthetic $Al_{63}Cu_{24}Fe_{13}$ standard and found to match, within 1 atomic % [20]. The unknown icosahedral phase appeared to be the natural analogue of the thermodynamically stable quasicrystal discovered two decades earlier by Tsai et al. [15].

2.1.2 The Florence sample

The main question was then: how did the quasicrystal form? Clues were found among the remaining material of the Florence sample [22]. The first clue was a five-nanometer quasicrystal inclusion found in a fifty-nanometer grain of stishovite, which is a high-pressure polymorph of SiO_2. This occurrence indicates that the quasicrystal either formed before or during the high-pressure event that led to the formation of stishovite. The pressure required to form stishovite ruled out the possibility that the quasicrystal originated as slag from an aluminum smelter. It pointed instead to formation at high pressures, which could be found either in the lower mantle or in an impact. The latter opened up the possibility of formation in outer space.

To gain insight into whether the formation was terrestrial or not, the oxygen isotopes of some of the oxides and silicates were analyzed using secondary ion mass spectrometry (SIMS). Minerals that form terrestrially have significantly different oxygen isotope ratios $^{18}O/^{16}O$, $^{17}O/^{16}O$ than those that formed in the early solar system and remained unaltered, with the reason being that minerals forming in the early solar system underwent isotopic exchange with the early solar nebula [42]. The SIMS

analyses conclusively showed that the oxides and silicates were meteoritic, with some that resembled minerals found in Ca-Al-rich inclusions (CAIs), which are among the oldest solids in the solar system [22, 43]. With the evidence showing that the Florence sample was of natural origin, the quasicrystal was accepted in 2011 as a mineral under the name "icosahedrite" [21].

Although it was becoming clear that the icosahedrite-bearing rock had a rich, outer-space history, the investigation was unfortunately reaching its limits. Not much remained of the Florence sample after the slicing, dicing, and pulverizing; and, among the material that was destroyed were most of the contacts between icosahedrite and other phases. These contacts—the neighboring phases and the textures between phases—provide the context with which one could begin to piece together how icosahedrite first formed. More material was needed to resolve the history of icosahedrite. Thus began a strange and incredible expedition to Chukotka [23, 39, 40].

2.1.3 The Khatyrka meteorite

The expedition involved extracting and panning $\gtrsim$1.5 tons of clay from a variety of depositional environments (i.e., lacustrine, alluvial, reworked) along the Listvenitovyi stream in the Khatyrka ultramafic (i.e., SiO_2-poor) zone within the Koryak Mountains, which runs alongside the Eurasian coast of the Bering Sea in far north-eastern Russia. Bags of clay recovered from the expedition were then laboriously picked through in the laboratory. Around ten meteoritic grains have been found to-date, mostly from $\gtrsim$7000 year-old undisturbed alluvium, with many having components that resemble what was originally found in the Florence sample. The chemical and petrological study of these grains has shown that they are fragments of the same parent meteorite body, which has been officially named the "Khatyrka" meteorite.

The Khatyrka meteorite [22, 23] resembles the widely studied Allende meteorite and, like Allende, is classified as an oxidized-subgroup CV3 carbonaceous chondrite. Khatyrka contains silicates and oxides that are typical of CV3 (ox) chondrites [44, 45, 46, 47, 48], including: (1) a highly porous matrix, dominated by platy olivines with ferroan compositions (50-56 mol % forsterite, denoted Fo_{50-56}) typical of CV3 chondrites [46]; (2) Type IA porphyritic olivine chondrules, with minor element variations typical of CV3 chondrule olivines [49]; and (3) CAIs that are identical to those in oxidized CV3 chondrites [43].

While the silicates and oxides (and, generally, the presence of chondrules and CAIs) may be quite typical, the quasicrystals and Al-bearing alloys are not. So far, the only known natural occurences of these phases are in the Khatyrka meteorite, and these phases are ubiquitous among the recovered grains [23, 25, 26, 50, 51, 52]. Many more examples of icosahedrite, khatyrkite, and cupalite have been found, in addition to several new metallic alloy minerals that include: (i) "steinhardtite" ($Al_{38-50}Ni_{32-40}Fe_{10-30}$), an allotrope of aluminum, with a body-centered cubic lattice [51]; (ii) "decagonite" ($Al_{70.2(3)}Ni_{24.5(4)}Fe_{5.3(2)}$), the second natural quasicrystal and first with decagonal symmetry [50]; and (iii) an as-yet-unnamed quasicrystal with icosahedral symmetry and composition $Al_{62}Cu_{31}Fe_7$, the first quasicrystal to be discovered in nature prior to discovery in the laboratory [26].

2.2 Puzzles

We now turn to the puzzles that have been largely resolved by the results presented in this Chapter.

2.2.1 Natural origin of Al-Cu alloys

There is indisputable evidence for the meteoritic origin of the silicates and oxides of the Khatyrka meteorite, e.g., the oxygen isotope measurements reported earlier. However, direct analytical evidence either for or against the natural meteoritic origin of the Al-Cu alloys has been lacking, and there have been no clear signs of chemical reaction between the reduced metal alloys and the oxidized meteoritic silicates. A further complication in interpreting the Al-Cu alloys to be of natural origin has been that such alloys were previously unexpected to occur in nature [22, 23].

Metallic Al requires extremely reducing conditions to form. For example, at 1200°C, to stabilize pure metallic Al requires a log-oxygen fugacity $\log_{10} f_{O_2} \lesssim -28$ [22]. However, even the highly-reducing innermost hot regions of the pre-solar nebula at 4.567 Ga had $\log_{10} f_{O_2} \approx -20 \pm 1$ at 1200°C, which is nowhere near as reducing as is needed [53]. For comparison, at 1200°C, the FeO/Fe redox buffer curve has $\log_{10} f_{O_2} \approx -11$ and SiO_2/Si has $\log_{10} f_{O_2} \approx -20$ [22].

Another puzzle is that Al and Cu have greatly differing cosmochemical behaviors: Al is a refractory lithophile element that condenses at very high temperatures out of a hot and cooling gas of Solar composition, whereas Cu is a moderately volatile siderophile/chalcophile element that condenses at a much lower temperature than Al.

2.2.2 Formation history of Al-Cu-Fe alloys

Earlier investigations of Khatyrka have produced abundant petrologic and chemical evidence showing that Khatyrka experienced at least one high-velocity impact event [54, 55]. This includes, in addition to the stishovite in the Florence sample, the observation of two high-pressure Fe-bearing phases: ahrensite (Fe_2SiO_4), which only forms at >5 GPa [56], and an unnamed oxide with composition $Fe_{2.6}Si_{0.4}O_4$ that has the structure of spinelloid V, which only forms at 3-8 GPa [57].

Measurements of noble gas cosmogenic nuclides in the olivine of 126 show that the most recent major impact event experienced by Khatyrka occurred in space a few 100 Ma [58, 59]. and produced shocks consistent with the range S3 to S5 (though probably closer to S4), corresponding to approximately 10-35 GPa [60]. An impact of this magnitude could account for the high-pressure phases, as well as the silicate melt and reactions that we report herein. Because there is currently no evidence to the contrary, we will assume this is the case for the purpose of our discussion here, referring only to a single 'impact event' occurring a few 100 Ma, while acknowledging that we could also be observing the results of a series of impact events occurring over eons of time.

Based on the evidence of impact, two competing hypotheses were proposed in [55] to explain the relationship between the 'impact event' that led to the formation of high-pressure FeO-bearing phases and the event that formed the Al-Cu-Fe metal, which we refer to as the 'metal-forming event'. Observations that rule out either hypothesis would have implications for how the Al-Cu-Fe alloys first formed, such as the age of the Al-Cu-Fe alloys and whether the alloys formed in outer space or on Earth.

In the first hypothesis, the 'impact event' and 'metal-forming event' are the same. In this hypothesis, the Al-Cu-Fe alloys did not exist prior to the impact; instead, the Al, Cu, and Fe were incorporated in other phases, possibly Al- and Cu-bearing Fe-Ni metals, which then melted upon impact. Post-shock liberation of Cu has been discussed in the literature [61, 62], and Cu-bearing metal phases are commonly observed in meteorites (see, e.g., [61]). The Al would be similarly exsolved; however, Al-bearing Fe-Ni metals have only been observed and extensively studied in Khatyrka [50, 51], although an unconfirmed example has also been noted in a study of the shocked Suizhou L6 chondrite [63]. A challenge for this hypothesis is to explain the amount

of Al and Cu that would have to be liberated to account for the observed volume of Al-Cu alloys in Khatyrka.

In the second hypothesis, the 'impact event' and 'metal-forming event' are not the same. The essential difference is that, according to this hypothesis, whatever event formed the Al-Cu-Fe metals is different from the impact event(s) that produced the observed high-pressure FeO-bearing mineral phases. As stated, this hypothesis does not make any claims as to the specific mechanism for how the first Al-Cu-Fe alloys formed.

2.2.3 Recent progress

In this Chapter, we resolve the puzzles described above by presenting evidence of cross-cutting relationships and chemical reaction between the reduced Al-Cu-Fe metal alloys and the oxidized meteoritic silicates. (Cross-cutting relationships provide a time ordering between two or more materials. A material which cuts across another material is the younger of the two.) The new evidence occurs in a recently identified fragment of Grain 126, found during our continued study of grains from the Khatyrka meteorite. To distinguish the fragment from others of Grain 126, we refer to it as "Grain 126A". It is deposited at the Smithsonian Institution's National Museum of Natural History, Washington DC, USA under the catalogue number USNM 7908. We also document the petrological context of four new Al-Cu-Fe minerals, discovered in Grain 126A and recently reported in [26], [52], and [25]. We note that the interpretation here of a reaction history is supported by preliminary studies on Grain 129, some results of which were reported in [54].

The evidence of cross-cutting relationships and redox reactions support the second hypothesis of Section 2.2.2—that the 'impact event' and 'metal-forming event' are distinct from one another—and provide clues about the sequence of events that occurred in 126A during the most recent impact a few 100 Ma. The results indicate

that some, but not most, of the Al-bearing grains observed in 126A (including some quasicrystals) were formed as a direct result of the impact in space. An important corollary is that most of the Al-bearing alloys (including quasicrystals) existed prior to the impact, and so had to have formed in space at some earlier time.

The outline of this Chapter is as follows: We begin in Section 2.3 by describing the mineralogy and petrographical characteristics of Grain 126A. Then, in Section 2.4, we present the evidence for the redox reaction between the Al-Cu-Fe metal phases and silicate melt. Section 2.5 explains how the observed cross-cutting relationships between Al-Cu-Fe metal and silicate glass indicate that the 'metal-forming event' is distinct from and occurred prior to the 'impact event'. In Section 2.6, we demonstrate that there are two generations of quasicrystals in 126A: some formed during the 'impact event', and some formed prior. Moreover, among the quasicrystals that formed during the 'impact event', there is a quasicrystalline phase that is notable for at least two reasons: (i) it is the third ever quasicrystal to be discovered in nature; and, (ii) it is the first to be found in nature *prior to* discovery of a synthetic analogue. We describe two possible formation pathways for this novel quasicrystal and report on a related shock recovery experiment [27]. In Section 2.7, new temperature constraints and new evidence for rapid cooling and heterogeneous temperature distribution are provided. Finally, in Section 2.8, we conclude by discussing how the new results resolve the puzzles presented in Sections 2.2.1 and 2.2.2.

2.3 Description of sample

Grain 126A (Fig. 2.1) is dominated by relatively large (100-300 μm), irregularly shaped assemblages of Al-Cu-Fe metals (lighter, Fig. 2.1a; blue/purple, Fig. 2.1b) and, in the center-right of the figure, irregularly shaped olivine grains (10-30 μm). There are also smaller Al-Cu-Fe metal grains (5-20 μm), Fe-Ni globules (3-25 μm,

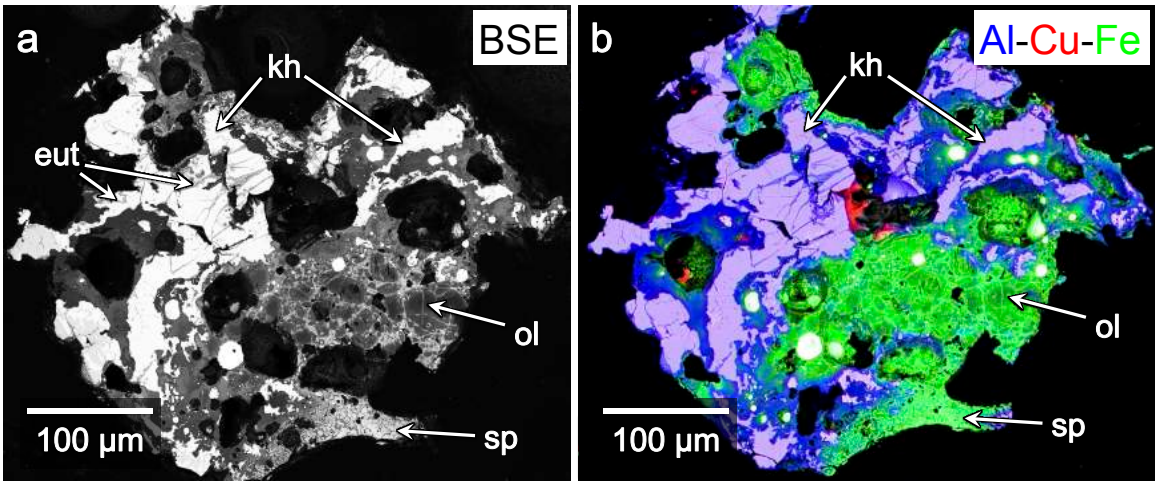

Figure 2.1: **Overview of Khatyrka Grain 126A.** (a) Backscattered electron (BSE) image of Grain 126A. Bright regions are mostly Al-Cu-Fe metal assemblages; they have an irregular, cuspate-lobate appearance and consist predominantly of khatyrkite ("kh"), stolperite, and eutectoid regions ("eut"; further detail in Fig. 2.3) that contain a vermicular mixture of metallic Al (up to 13.3 weight% Cu) and khatyrkite. The darker regions mostly comprise crystals of olivine ("ol"; further detail in Figs. 2.2c, 2.2d) and spinel-group minerals with varying composition, which we call "spinel" ("sp"; further detail in Fig. 2.6)—all surrounded by silicate glass. (b) Al-Cu-Fe combined X-ray area map, overlaid on a BSE image. Light purple regions are Al-Cu metal (khatyrkite, stolperite); blue/dark purple regions are predominantly glass and spinel; green regions are mainly the silicate glass and crystals that grew within the melt (olivine, spinel); the relatively large white grains are predominantly Fe-Ni (appearing white because of the underlying BSE image, despite containing Fe). The different compositions of spinel manifest here as different degrees of brightness (a) and different colors (b).

round and bright in Fig. 2.1), and a fine-grained, hypohyaline assemblage of olivine (2-10 µm) and spinel-group (<2 µm) crystals. (We refer to the spinel-group minerals, which occur in 126A with various compositions, as "spinel".) Each Al-Cu-Fe metal assemblage is surrounded by a rim of spinel crystals (<1 µm). Most assemblages have, adjacent to this spinel layer, Fe and Fe-Si metal beads, varying in size from <10 nm to ~5 µm. All of these phases are set in a glass. Small fragments of Al-Cu-Fe assemblages occur immediately above and below the region dominated by olivine, in the center-right of Fig. 2.1. The upper half and the left half of the figure are dominated by the relatively large Al-Cu-Fe assemblages. Averaged and representative

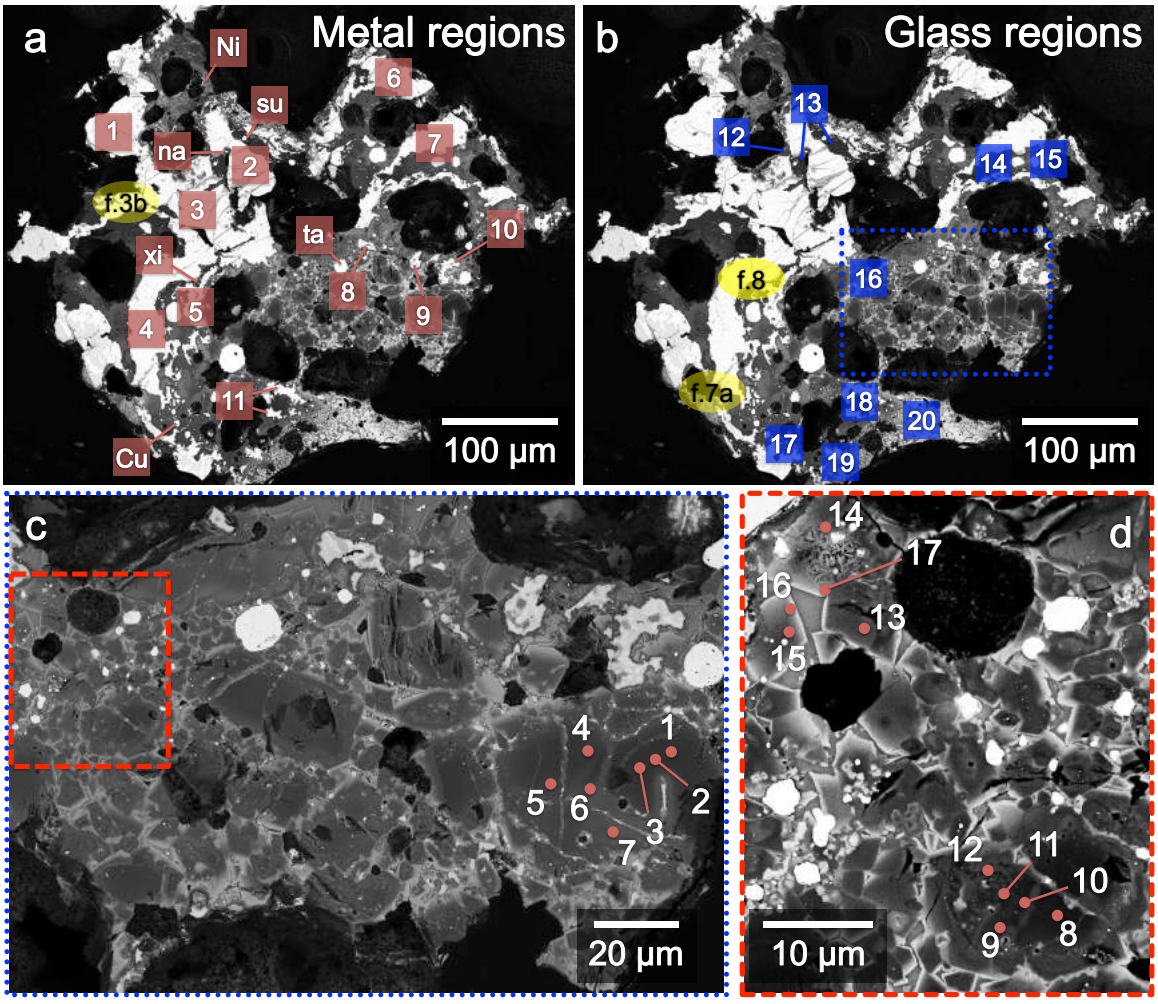

Figure 2.2: **BSE images, marked to show locations of EPMA-WDS and SEM-EDS analyses, with close up views of olivine in (c) and (d).** Red squares in (a) indicate metal regions referred to in Table 2.1. Blue squares in (b) indicate glass regions referred to in Table 2.2b and Fig. 2.5. Yellow ovals in (a) and (b) are referred to in Figs. 2.3b, 2.7a, and 2.10. (c) Close up of area boxed in blue in (b). This region contains several olivine crystals. The larger grains are cross-cut by Fe-rich veins that are continuously connected to glass. Analyses of numbered spots are provided in Table 2.2a. These appear to be relict olivine grains. (d) Close up of area boxed in red in (c) showing small euhedral to subhedral olivine grains that appear to be a non-relict, second generation of olivine that grew from the matrix melt. Analyses of numbered spots are provided in Table 2.2a.

analyses of the different phases are presented in Tables 2.1-2.2; regions that were analyzed are shown in Fig. 2.2. For the olivine and spinel compositions, we took care to center the electron beam on individual crystals to minimize excitation of elements in neighboring phases. Similarly, for the glass compositions, we took care to avoid crystalline material. Electron backscatter diffraction was used to identify the structure of various phases.

Table 2.1: Averaged elemental compositions of metal phases in 126A by EPMA-WDS. All in elemental weight %.

n: number of analyses included in average, n.a.: not analyzed, b.d.l.: below detection limits, 0.07 wt% Al, 0.2% Ni, 0.05% Si, 0.04% Mg, 0.03% Ca, 0.05% Cr; SEM-EDS detection limit 0.1 wt%. Uncertainty given in parentheses represents one standard deviation from the mean based on all analyses (e.g., $50.3\,(13) = 50.3 \pm 1.3$). [a] Location refers to Figure 2.2a. [b]Iron composition is averaged over multiple iron beads. [c]Xifengite analyzed by SEM-EDS (normalized total to 100%).

Phase	Location[a]	n	Al	Fe	Cu	Ni	Si	Mg	Ca	Cr	Total
khatyrkite	1	16	47.89 (17)	0.54 (14)	51.22 (51)	b.d.l.	b.d.l.	b.d.l.	b.d.l.	b.d.l.	99.65
	2	9	48.01 (27)	0.72 (20)	51.73 (48)	b.d.l.	b.d.l.	b.d.l.	b.d.l.	b.d.l.	100.46
	3	13	47.70 (28)	0.61 (14)	51.34 (54)	b.d.l.	b.d.l.	b.d.l.	b.d.l.	b.d.l.	99.65
	4	9	47.97 (43)	1.04 (6)	50.97 (51)	b.d.l.	0.06 (2)	b.d.l.	b.d.l.	b.d.l.	100.04
	5	5	48.88 (49)	1.40 (12)	50.07 (78)	b.d.l.	b.d.l.	b.d.l.	b.d.l.	b.d.l.	100.35
	6	8	48.16 (24)	0.85 (13)	50.94 (49)	b.d.l.	b.d.l.	b.d.l.	b.d.l.	b.d.l.	99.95
	7	11	48.06 (42)	1.34 (18)	50.78 (87)	b.d.l.	b.d.l.	b.d.l.	0.03 (2)	b.d.l.	100.21
	8	2	47.82 (19)	2.68 (1)	49.31 (3)	b.d.l.	0.16 (1)	b.d.l.	0.03 (2)	0.07 (3)	100.08
	9	2	48.74 (50)	2.10 (3)	49.94 (9)	b.d.l.	0.09 (5)	0.07 (10)	b.d.l.	b.d.l.	100.94
	10	2	48.42 (5)	2.16 (7)	49.37 (91)	b.d.l.	0.10 (2)	b.d.l.	0.05 (4)	b.d.l.	100.10
	11	2	47.24 (11)	1.55 (15)	50.20 (3)	b.d.l.	0.20 (11)	b.d.l.	b.d.l.	b.d.l.	99.19
stolperite	4	3	38.71 (20)	1.45 (12)	59.53 (59)	b.d.l.	b.d.l.	b.d.l.	0.03 (1)	b.d.l.	99.72
	5	3	38.33 (11)	2.70 (32)	57.77 (46)	b.d.l.	b.d.l.	b.d.l.	b.d.l.	0.05 (3)	98.85
	8	2	35.94 (37)	4.23 (4)	61.23 (42)	b.d.l.	b.d.l.	b.d.l.	b.d.l.	0.07 (2)	101.47
	9	3	33.921 (76)	3.09 (11)	62.71 (62)	b.d.l.	b.d.l.	b.d.l.	b.d.l.	0.05 (1)	99.78
	10	2	35.80 (5)	2.65 (26)	60.80 (11)	b.d.l.	b.d.l.	b.d.l.	0.04 (1)	b.d.l.	99.29
	11	2	36.13 (29)	2.73 (9)	60.83 (86)	b.d.l.	b.d.l.	b.d.l.	b.d.l.	b.d.l.	99.69
i-I	8	3	43.16 (13)	15.04 (50)	41.03 (41)	b.d.l.	0.14 (1)	b.d.l.	0.04 (1)	0.14 (1)	99.55
i-II	9	3	41.98 (67)	9.43 (94)	47.26 (92)	b.d.l.	0.08 (1)	0.04 (6)	b.d.l.	0.09 (3)	98.88
i-II	10	9	40.32 (47)	9.16 (35)	48.74 (64)	b.d.l.	0.06 (3)	0.06 (6)	0.04 (1)	0.11 (2)	98.49
kryachkoite	4	3	59.95 (65)	11.80 (14)	26.38 (30)	b.d.l.	0.16 (3)	b.d.l.	b.d.l.	0.32 (2)	98.61
hollisterite	8	4	55.04 (40)	30.42 (64)	14.15 (25)	b.d.l.	0.30 (1)	b.d.l.	0.03 (1)	0.16 (3)	100.11
iron[b]		5	b.d.l.	95.02 (52)	1.02 (13)	2.04 (9)	b.d.l.	n.a.	n.a.	n.a.	98.08
suessite	su	3	b.d.l.	80.89 (61)	1.85 (14)	0.55 (4)	14.23 (19)	n.a.	n.a.	n.a.	97.52
naquite	na	3	0.83 (38)	57.22 (64)	2.09 (39)	0.73 (4)	35.33 (19)	0.31 (12)	0.09 (3)	1.06 (1)	97.66
nickel	Ni	3	b.d.l.	3.86 (11)	3.53 (15)	90.45 (43)	b.d.l.	b.d.l.	b.d.l.	b.d.l.	97.84
copper	Cu	2	b.d.l.	3.82 (21)	94.19 (29)	b.d.l.	b.d.l.	n.a.	n.a.	n.a.	98.01
taenite	ta	4	b.d.l.	66.03 (40)	0.67 (9)	30.36 (30)	b.d.l.	n.a.	n.a.	n.a.	97.06
xifengite[c]	xi	1	b.d.l.	72.27 (42)	2.10 (43)	b.d.l.	24.46 (27)	b.d.l.	b.d.l.	1.17 (14)	100.00

Table 2.2: Point analyses of olivine (a) and averaged compositions of glass (b) and spinel (c) in 126A by EPMA-WDS. All in compound weight %.

n: number of analyses included in average, b.d.l.: below detection limits, 0.02 wt% Ca, 0.03% Na, 0.02% P, 0.08% Cu, 0.06% Cr, 0.06% Ni; SEM-EDS detection limit ∼0.1 wt%. Uncertainty given in parentheses represents one standard deviation from the mean based on: counting statistics (for olivine); all analyses (for spinel and glass), (e.g., $50.3(13) = 50.3(1.3) = 50.3 \pm 1.3$). [a]S# refers to a point analysis of olivine, where the # corresponds to a location specified in Figures 2.2c or 2.2d. [b]Forsterite content ("Fo") calculated as average of [Mg]/2 and 1 - [Fe]/2, where [Mg], [Fe] are atomic ratios of Mg and Fe, respectively, normalized to 3 cations. [c]Location refers to Figure 2.2b. [d]All Fe in glass compositions considered as FeO. [e]Fe_2O_3 content calculated by charge balancing on the basis of 4 Oxygen atoms. [f]Sp-Mg analyzed by SEM-EDS (unnormalized).

a. *Olivine*

Spot[a]	Fo[b]	SiO_2	Al_2O_3	FeO	Fe_2O_3	MgO	CaO	Na_2O	P_2O_5	CuO	Cr_2O_3	NiO	Total
S1	98	42.7 (2)	0.11 (2)	1.45 (8)		55.5 (2)	0.61 (2)	b.d.l.	b.d.l.	b.d.l.	0.18 (5)	b.d.l.	100.55
S2	98	42.7 (2)	0.14 (2)	1.23 (7)		55.4 (2)	0.65 (2)	b.d.l.	b.d.l.	b.d.l.	0.18 (5)	b.d.l.	100.30
S3	99	42.7 (2)	0.17 (2)	1.00 (7)		56.3 (2)	0.66 (2)	b.d.l.	b.d.l.	b.d.l.	0.13 (5)	b.d.l.	100.96
S4	95	41.7 (2)	0.11 (2)	5.0 (1)		53.3 (2)	0.57 (2)	b.d.l.	b.d.l.	0.09 (4)	0.21 (5)	b.d.l.	100.98
S5	92	41.1 (2)	0.09 (2)	8.0 (2)		50.4 (2)	0.49 (1)	b.d.l.	b.d.l.	0.11 (4)	0.15 (5)	b.d.l.	100.34
S6	84	39.9 (2)	0.07 (2)	14.9 (2)		43.9 (2)	0.56 (2)	0.03 (2)	b.d.l.	b.d.l.	0.13 (5)	b.d.l.	99.49
S7	77	38.8 (2)	0.05 (2)	21.2 (3)		39.6 (2)	0.39 (1)	b.d.l.	b.d.l.	b.d.l.	b.d.l.	0.08 (4)	100.12
S8	88	40.6 (2)	0.11 (2)	11.1 (2)		47.6 (2)	0.25 (1)	b.d.l.	b.d.l.	0.19 (4)	0.10 (5)	b.d.l.	99.95
S9	85	39.5 (2)	0.10 (2)	14.3 (2)		44.9 (2)	0.27 (1)	0.05 (2)	b.d.l.	0.16 (4)	b.d.l.	0.27 (4)	99.55
S10	79	39.0 (2)	0.06 (2)	18.1 (2)		40.6 (2)	0.23 (1)	b.d.l.	b.d.l.	0.25 (5)	0.21 (5)	1.83 (6)	100.28
S11	82	39.5 (2)	0.10 (2)	16.7 (2)		43.2 (2)	0.44 (1)	b.d.l.	b.d.l.	0.20 (5)	0.13 (5)	0.11 (4)	100.38
S12	78	37.9 (1)	1.12 (3)	19.6 (2)		40.4 (2)	0.25 (1)	b.d.l.	0.06 (3)	0.15 (5)	0.36 (6)	0.67 (4)	100.51
S13	73	37.6 (1)	0.80 (3)	22.9 (3)		36.1 (2)	0.17 (1)	b.d.l.	0.73 (5)	0.44 (5)	0.35 (6)	b.d.l.	99.09
S14	64	36.4 (1)	0.98 (3)	29.9 (3)		29.9 (1)	0.18 (1)	b.d.l.	0.82 (5)	0.80 (5)	0.14 (5)	b.d.l.	99.12
S15	61	35.4 (1)	0.97 (3)	32.0 (3)		28.7 (1)	0.17 (1)	b.d.l.	0.97 (5)	0.62 (5)	0.11 (5)	0.08 (4)	99.02
S16	45	33.6 (1)	0.87 (3)	43.6 (4)		20.1 (1)	0.31 (1)	b.d.l.	1.07 (6)	0.83 (6)	0.11 (4)	b.d.l.	100.49
S17	57	35.2 (1)	0.69 (3)	35.4 (3)		26.4 (1)	0.18 (1)	b.d.l.	0.86 (5)	0.67 (5)	b.d.l.	b.d.l.	99.40

b. *Glass*

Location[c]	*n*	SiO_2	Al_2O_3	FeO[d]	Fe_2O_3	MgO	CaO	Na_2O	P_2O_5	CuO	Cr_2O_3	NiO	Total
12	3	40.7 (42)	15.4 (29)	10.9 (10)		16.66 (32)	9.0 (11)	1.263 (73)	0.350 (60)	1.403 (27)	b.d.l.	0.21 (10)	95.90
13	6	46.57 (66)	28.4 (22)	0.60 (26)		14.9 (27)	7.47 (62)	1.07 (32)	b.d.l.	0.897 (85)	b.d.l.	b.d.l.	99.96
14	4	44.9 (21)	22.9 (59)	9.0 (66)		15.6 (27)	4.25 (65)	1.37 (78)	0.17 (17)	0.87 (10)	0.12 (10)	b.d.l.	99.12
15	4	42.9 (34)	16.49 (66)	23.8 (35)		8.1 (22)	4.10 (41)	0.41 (10)	0.54 (11)	0.83 (25)	b.d.l.	b.d.l.	97.20
16	2	35.2 (46)	18.4 (12)	35.11 (79)		3.1 (28)	5.6 (14)	0.450 (43)	1.63 (36)	0.80 (35)	b.d.l.	b.d.l.	100.30
17	19	34 (10)	30 (10)	15.7 (81)		13.9 (23)	1.94 (68)	0.38 (22)	0.54 (74)	0.68 (32)	0.63 (54)	b.d.l.	97.80
18	6	45.94 (49)	32.07 (78)	4.53 (88)		12.7 (12)	2.862 (76)	0.40 (12)	b.d.l.	0.626 (59)	0.302 (53)	b.d.l.	99.42
19	4	42.0 (51)	15.3 (31)	18.8 (14)		13.7 (15)	2.39 (23)	0.264 (27)	0.68 (13)	0.593 (53)	0.14 (23)	b.d.l.	93.84
20	3	36.3 (38)	4.7 (36)	33.8 (38)		13.5 (75)	2.0 (18)	0.47 (59)	1.19 (58)	0.38 (25)	b.d.l.	2.9 (38)	95.31

c. *Spinel*

Phase	*n*	SiO_2	Al_2O_3	FeO	Fe_2O_3[e]	MgO	CaO	Na_2O	P_2O_5	CuO	Cr_2O_3	NiO	Total
Crust	11	6.53 (5.86)	52.28 (13.89)	17.14 (4.73)	3.78 (9.37)	14.73 (2.56)	0.50 (0.42)	0.22 (0.14)	0.15 (0.09)	1.95 (2.17)	2.19 (1.60)	0.09 (0.01)	99.56
Sp-Al	15	3.60 (4.97)	39.87 (14.91)	21.08 (3.35)	18.85 (17.87)	12.30 (3.38)	0.25 (0.31)	0.06 (0.07)	0.16 (0.08)	0.14 (0.27)	2.53 (1.53)	2.74 (2.52)	101.57
Sp-Fe	17	3.53 (3.43)	12.81 (7.26)	25.01 (4.62)	48.41 (10.86)	6.56 (2.49)	0.24 (0.27)	0.10 (0.09)	0.11 (0.04)	0.09 (0.30)	0.64 (0.89)	4.10 (1.80)	101.61
Sp-Mg[f]	11	8.93 (4.16)	56.12 (6.25)	11.91 (4.55)	0.81 (2.03)	19.70 (2.45)	b.d.l.	b.d.l.	b.d.l.	b.d.l.	2.38 (5.23)	b.d.l.	99.85

2.3.1 Al-Cu-Fe metals

The Al-Cu-Fe metal grains have complex grain boundaries. Many of the grain boundaries display cuspate-lobate fold morphology, others are rounded to amoeboid, and some are straight and angular. In many cases, the cuspate-lobate boundaries show the cusps point to the metal grains. There is a halo of Al_2O_3-enrichment (appears as blue/purple, Fig. 2.1b), extending beyond the metal boundaries into the silicate regions. Averaged compositions of metal phases from regions marked in Fig. 2.2a are presented in Table 2.1.

Among the metal grains are four new Al-Cu-Fe minerals, which were recently reported in [26], [52], and [25]. They include stolperite (AlCu) [25, 52], kryachkoite ($(Al,Cu)_6(Fe,Cu)$) [25, 52], hollisterite (Al_3Fe) [25, 52], and an as-yet-unnamed quasicrystal [26] (denoted 'i-II'). The quasicrystal i-II has the same icosahedral symmetry as icosahedrite [20, 21] (denoted 'i-I') but a composition $Al_{62.0(8)}Cu_{31.2(8)}Fe_{6.8(4)}$, which is outside the measured equilibrium stability field at standard pressure of icosahedrite ($Al_xCu_yFe_z$, with x between 61 and 64, y between 24 and 26, z between 12 and 13%) [17, 64, 65].

The large (100-300 μm) Al-Cu-Fe metal fragments mostly comprise khatyrkite ($CuAl_2$, with up to 2.68 elemental weight % Fe) and variable amounts of stolperite. Within some of the Al-Cu-Fe metal grains and sometimes along their edges, there are mixtures of khatyrkite and Al, with a vermicular texture (Fig. 2.3). The Al in these mixtures contains up to 13.3 elemental weight % Cu. Given their texture and composition, we refer to these regions as "eutectoid". In Figure 2.3a, the grain boundaries between glass and the metal alloys are relatively straight. Straight grain boundaries typically indicate formation by fracture or along crystal faces [66]. Here, we infer that the glass may have filled a fracture. The glass appears to cross-cut what may have been connected eutectoid regions. In Figure 2.3b, the eutectoid regions

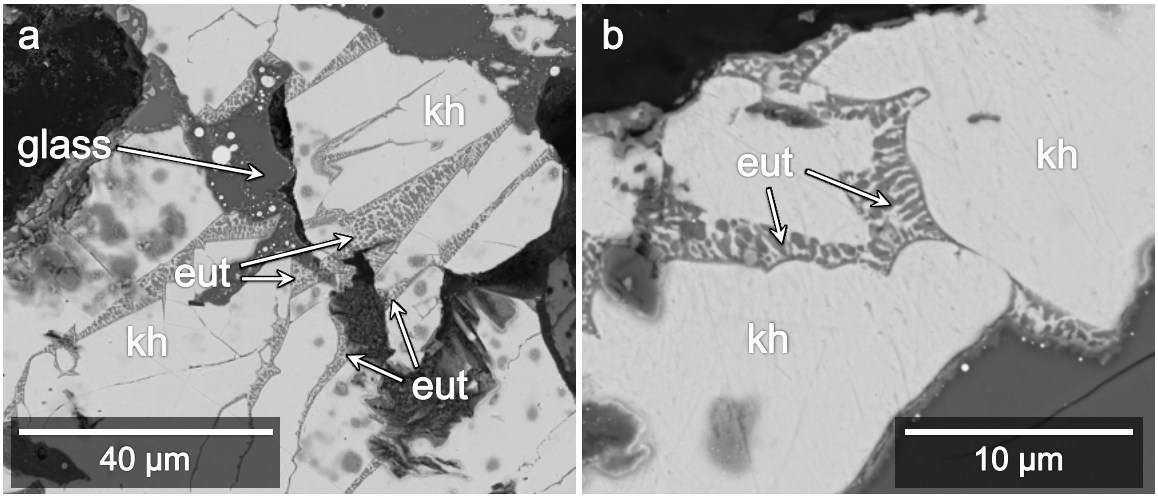

Figure 2.3: **BSE images of eutectoid regions.** (a) Close up of region overlapping with Locations 2 and 3 (Fig. 2.2a). The wedge-shaped silicate glass region appears to cross-cut khatyrkite metal ("kh") and what may have been previously connected eutectoid regions ("eut"). (b) Close up of Location f.3b (Fig. 2.2a). Cuspate-lobate boundaries of the eutectoid regions here suggest they were partially molten, whereas the khatyrkite was solid.

have cuspate-lobate boundaries where they are in contact with the adjacent metal grains. Along these edges, the cusps tend to point away from the eutectoid regions.

There is a single occurrence of hollisterite (Fig. 2.4a), which occurs immediately adjacent to grains of i-I (Fig. 2.4b). The upper and lower ends of the hollisterite grain are overlaid by a crust of spinel crystals (see discussion of the spinel crust below). The grains of i-II are surrounded, sequentially, by stolperite, khatyrkite, and Al (Fig. 2.4c). Kryachkoite appears as euhedral grains within some eutectoid mixtures.

2.3.2 Silicates and oxides

The material surrounding the Al-Cu-Fe metal grains is a fine-grained, hypohyaline assemblage of olivine and spinel quench crystals embedded in a glassy groundmass. Compositions taken from regions marked in Fig. 2.2b are presented in Table 2.2b. In Figure 2.5, all of the compositions are plotted in the ternary diagrams in terms of Al_2O_3-CaO-SiO_2 weight % and MgO-FeO-SiO_2 weight %. The compositions are

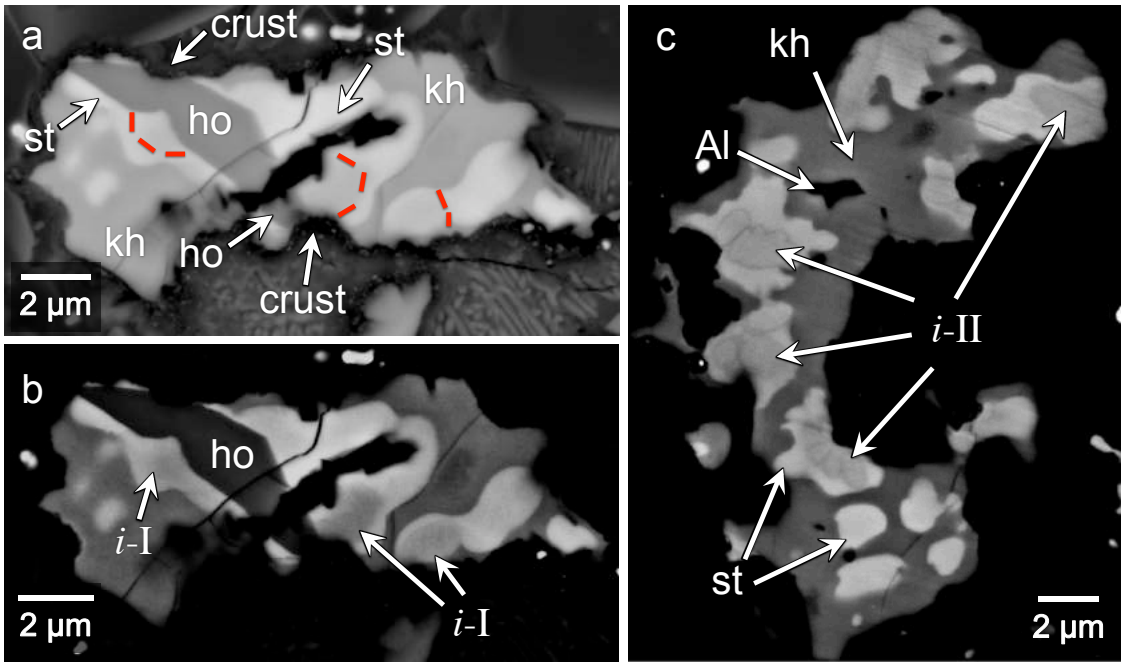

Figure 2.4: **BSE images of Al-Cu-Fe assemblages with two generations of quasicrystals.** Compositions for the metal phases shown here are listed in Table 2.1. Contrast in (b) and (c) has been stretched to emphasize compositional differences among the different metal phases. (a, b) Close up of Location 8 (Fig. 2.2a). This assemblage contains khatyrkite ("kh"), stolperite ("st"), hollisterite ("ho"), and icosahedrite ("i-I"). The red, dashed lines in (a) outline the icosahedrite grains to distinguish these grains from the neighboring phases; these sketches of the phase boundaries are based on higher contrast images of the same region, such as shown in (b). The upper and lower ends of the hollisterite grain terminate against the spinel crust ("crust"). We interpret this as a cross-cutting relationship that indicates the hollisterite and i-I are relict. The dark area in the center of the Al-Cu-Fe assemblage is a hole. (c) Close up of Location 10 (Fig. 2.2a). This assemblage contains quasicrystals ("i-II") that are distinct from i-I. Surrounding i-II is stolperite, which is surrounded by khatyrkite. The dark area in the interior of this assemblage is metallic Al ("Al"). The dark area external to this assemblage contains silicate phases, which are not discernable in this image because of the high contrast.

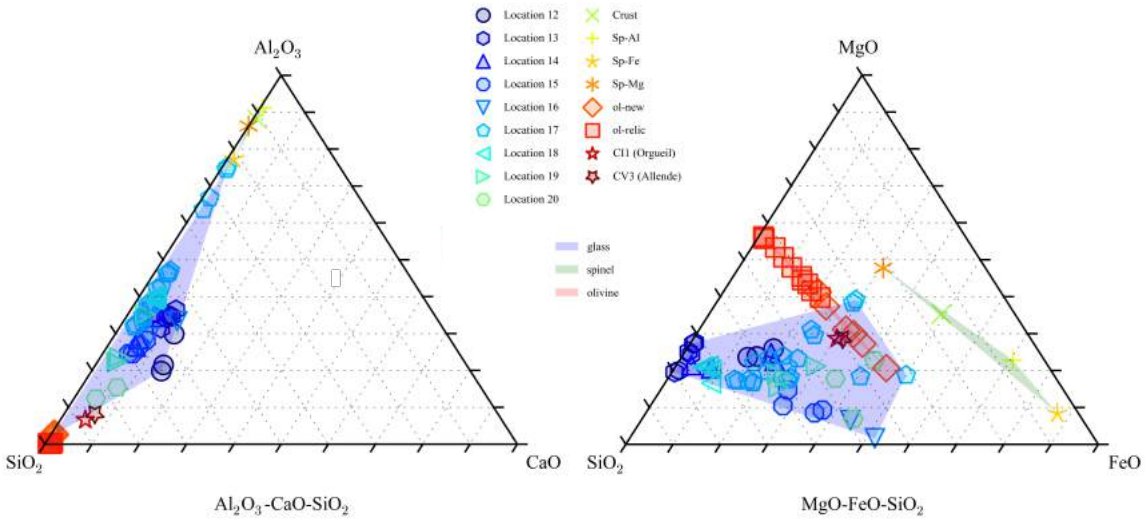

Figure 2.5: **Compositions of glass regions in 126A.** They are presented in terms of weight % Al_2O_3-CaO-SiO_2 (left) and MgO-FeO-SiO_2 (right) and normalized to 100%. The three shaded regions are the convex hulls of glass (blue), spinel (green), and olivine (red) compositions; each shaded region shows, roughly, the range of compositions for one of the three phases. Locations refer to those shown in Fig. 2.2b. Compositions vary widely both within the same region (see, e.g., Location 17) as well as across different regions. Also plotted for comparison are bulk compositions of the Orgueil (CI1) chondrite [67] (Fe_2O_3 from original analyses has been recalculated to FeO) and of the Allende (CV3) chondrite [68]. Orgueil's composition reflects bulk solar abundances, and Allende's is prototypical of CV3 chondrites. Compared to the bulk compositions of Orgueil and Allende, the glass in Grain 126A contains higher relative abundances of Al_2O_3 and lower relative abundances of FeO. This is consistent with modification of the matrix melt (which may originally have had composition similar to that of Orgueil and Allende) by assimilation of oxidized Al following redox reaction with Al-Cu-Fe metal. During the reaction, the FeO from the matrix melt reduced to metallic Fe, which then formed Fe beads.

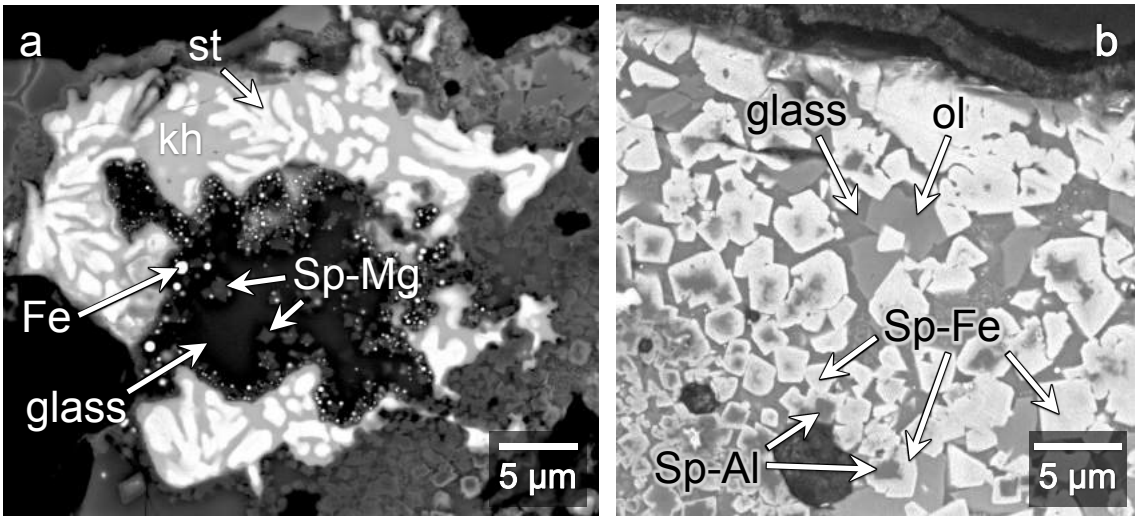

Figure 2.6: **BSE images of various spinel phases.** Compositions for spinel phases shown here are provided in Table 2.2c. (a) Close up of region overlapping with Locations 11 (Fig. 2.2a) and 18 (Fig. 2.2b). Khatyrkite ("kh") and stolperite ("st") have a texture indicating crystallization from a melt. Metallic Fe beads ("Fe") line the interior interface. Spinel crystals that grew here in the silicate melt (now glass) are denoted as "Sp-Mg". They have lower concentrations of FeO and Fe_2O_3 than the spinel crystals shown in (b). (b) Close up of Location 20 (Fig. 2.2b) showing Fe-rich spinel crystals ("Sp-Fe") and zoned spinel crystals with Fe-rich rims (also marked "Sp-Fe") and Al-rich cores ("Sp-Al"), all surrounded by glass. In contrast to (a), this region does not have Fe beads, but the spinel crystals here have higher concentrations of FeO and Fe_2O_3 than those in (a). Also noted in the image are olivine crystals ("ol", Fo_{50-56}).

widely distributed, varying not only across different regions of the sample, but also within the same region. Besides the glass, there are olivine crystals, contained primarily in the blue-boxed region in Fig. 2.2b that has been enlarged and shown separately in Fig. 2.2c. They exhibit a brecciated texture consisting of relatively larger (10-30 µm), fractured olivine grains, surrounded by fine-grained (2-10 µm) angular olivine fragments. Point analyses in this region are presented in Table 2.2a. All of the compositions are very close to stoichiometric olivine. The relatively larger grains have Mg-rich cores (Fo_{77-99}). Their appearance and composition resembles the chondrule olivines found in Grains 5 and 121 of Khatyrka [23]. The relatively smaller grains have subhedral to equant euhedral morphology, more ferroan cores (Fo_{61-73}) than the

larger grains, and rims that are Fe-rich (Fo_{45} in S16, Table 2.2a). Some of the smaller grains are shown in Fig. 2.2d, an enlarged version of the red-boxed region in Fig. 2.2c.

Averaged compositions of different spinel phases (Fig. 2.6) are presented in Table 2.2c. A layer of spinel crystals mantles each of the Al-Cu-Fe metal grains, separating the metal from the silicate regions (this is called "Crust" in Table 2.2c). This crust of spinel crystals forms part of the Al_2O_3-rich halo that envelops each of the metal grains (blue, Fig. 2.1b). Most metal grains also have a submicron-thin layer of Al-oxide located between the metal and the spinel crust. This Al-oxide layer is too thin to analyze for precise composition. In addition to the spinel crust, there are euhedral Mg-rich spinel crystals ($\lesssim$2 μm; "Sp-Mg", Fig. 2.6a, Table 2.2c). These spinel crystals tend to occur where the Al_2O_3 to FeO ratio in the adjacent glass is relatively high (more dark blue/purple, Fig. 2.1b), such as Locations 14, 17, and 18 (Fig. 2.2b, 2.6a), where the observed weight % ratio of Al_2O_3 to FeO ranges from 1.09 to 13.95. There are also subhedral to equant euhedral spinel crystals, some that have Al-rich cores ("Sp-Al"', Fig. 2.6b, Table 2.2c) and Fe-rich rims ("Sp-Fe", Fig. 2.6b, Table 2.2c), and others that are more homogeneous and near magnetite (Fe_3O_4) in composition (included in "Sp-Fe", Fig. 2.6b, Table 2.2c). The Sp-Al and Sp-Fe phases occur where the Al_2O_3 to FeO ratio in the adjacent glass is relatively low (more green, Fig. 2.1b), such as Location 20 (Figs. 2.2b, 2.6b), where the observed weight % ratio of Al_2O_3 to FeO ranges from 0.02 to 0.22.

Lastly, there are silicate phases surrounded by glass that are too fine-grained to resolve analytically. They include, for example, skeletal, acicular crystallites and others that exhibit granophyric textures (Fig. 2.7).

2.3.3 Metal beads and droplets (Fe, Fe-Si, Ni, Cu)

Near the interfaces between the Al-Cu-Fe metal grains and the silicates, there are spherical metallic Fe beads varying in size from less than 10 nm to $\lesssim$5 μm ("Iron",

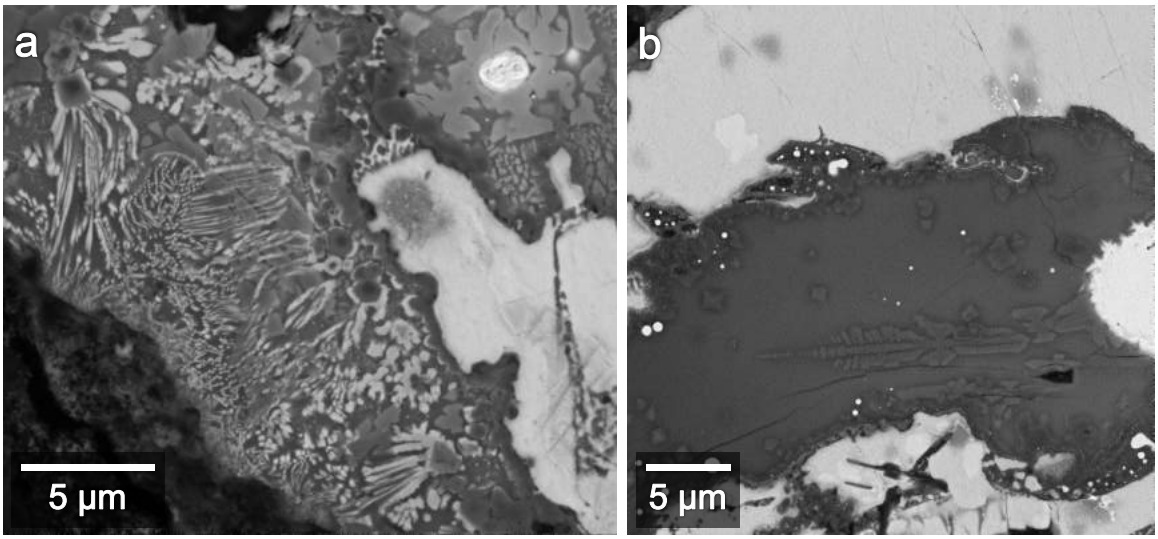

Figure 2.7: **BSE images of skeletal, quench textures in the silicate glass.** Individual phases are too small to analyze for precise compositions. (a) Close up of Location f.7a (Fig. 2.2b) showing granophyric textures. (b) Close up of Location 14 (Fig. 2.2b) showing feathery textures.

Table 2.1). Some of these beads are shown in Fig. 2.10a. The Fe beads contain variable amounts of Si, from below detection limit up to 35 weight %. Among the Fe-silicide beads are the minerals naquite (FeSi) [69], suessite (Fe_3Si) [70] and xifengite (Fe_5Si_3) [71] (Fig. 2.2a). Some of the larger Fe-beads contain S- and Cu-rich inclusions. The Fe- and Fe-Si beads are Ni-poor (as low as <0.1 weight %) and visibly distinct from the larger (3-25 µm) grains of taenite ("tae", Table 2.1), which dominate the olivine field in the center-right of the sample. A 1 µm Ni-rich droplet (90 weight % Ni) and 3-µm large Cu-rich droplet (94 weight % Cu) were also identified; their compositions can be found in Table 2.1.

2.4 Chemical reaction between Al-Cu-Fe metal and silicate matrix

Our study of Grain 126A shows that the melted silicate matrix and Al-Cu-Fe alloys reacted, probably exothermically, at temperatures above the bulk silicate solidus.

Oxidized Fe and Si in the silicate melt were reduced by metallic Al in the adjacent alloy. In reciprocal fashion, the metallic Al was oxidized and incorporated into the silicate melt. Subsequently, the reduced Fe and Si coalesced into beads. The oxidized Al diffused into the adjacent silicate melt and formed an Al_2O_3-rich zone (Fig. 2.1b). Some of the oxidized Al formed the Al-oxide layer and the aluminous spinel that crystallized on the metal grains. This mantle of spinel sealed off the metal from further reaction.

The reaction products (Fe, Fe-Si beads, Al_2O_3 halo, Al-oxide layer, and spinel) are mostly present along the metal-matrix interfaces where the reaction would have initiated (see, e.g., Fig. 2.10a). This is the clearest observation yet of a reaction zone in Khatyrka. The further observation that these reaction zones are narrow, extending only tens of microns at most away from the metal, argues for an extremely rapid process. The observations here are qualitatively similar to what was found in the impact experiments reported in [72]; there, a metallic Al projectile (with minor Cu) was shot into a quartz sand target, resulting in a redox reaction that produced a reaction zone of Al_2O_3 and beads of metallic Si.

Metallic Fe and Fe-silicide beads in 126A are similar to ones described in Grain 129 [54]. Such beads can be produced during impact [60, 69, 70, 71, 73, 74, 75, 76]. The observation of metallic Si alloying with Fe further indicates that, during the impact, the conditions were sufficiently reducing to favor formation of Fe-Si phases over Fe + SiO_2. However, there is no evidence that they were sufficiently reducing to produce Fe-Al phases in the silicate melt. We do, however, observe droplets of metallic Cu and Ni, consistent with these phases having f_{O_2} requirements less stringent than even metallic Fe. The presence of Cu droplets implies the simplified reaction ($\Delta_f H^o = 465$ kJ, using parameters from [77, 78, 79]):

$$CuAl_2 + MgFeSiO_4 \rightarrow Cu + Fe + Si + MgAl_2O_4 \ . \tag{2.1}$$

(We have assumed here for simplicity that the silicate melt originally had a bulk composition similar to the porous matrix of the unshocked regions of Khatyrka [23].) In addition to Cu appearing in metallic droplets surrounded by glass, we observe Cu as a minor constituent in the glass (up to 1.4 weight % CuO).

The two varieties of olivine differ in both appearance and chemistry. The relatively larger olivine crystals (S1-S7, Fig. 2.2c, Table 2.2a) have no detectable P_2O_5 and, on average, no CuO. The smaller olivine grains (S13-S17, Fig. 2.2d, Table 2.2a) have 0.73-1.07 weight % P_2O_5 and 0.44-0.83 % CuO. (There does not appear to be mixing of these analyses with neighboring glass, as there is no significant difference between concentrations of Al_2O_3, Na_2O, and CaO in the cores (S13, Fig. 2.2d) and in the rims (S16 and S17, Fig. 2.2d).) The larger grains also have considerably less Al_2O_3: up to 0.17 % Al_2O_3, compared with 0.69-1.12 Al_2O_3 in the smaller grains. For comparison, the neighboring glass has, on average, 1.63 % P_2O_5, 0.80 CuO, and 18.42 Al_2O_3 (Location 16, Table 2.2b). From the appearance and chemistry, we infer that the larger olivine grains are pre-impact relics, whereas the smaller grains are a newer generation that grew rapidly from the P_2O_5- and CuO-bearing silicate melt. This interpretation is supported by experimental studies of P-rich olivine [80] and nano-analytical studies of silicate inclusions in the Netschaëvo iron meteorite [81].

2.5 'Metal-forming event' occurred prior to the 'impact event'

As noted above, the cuspate-lobate boundaries between the Al-Cu-Fe metal grains and the glass have cusps that tend to point into the metal grains. The cuspate-lobate fold geometry forms as a buckling instability in compression, where the lobes point to the weaker material, and cusps point toward the stronger material [66]. Silicate melts have lower viscosities than solid metals, whereas in the solid-state metals are

less viscous than silicates. We thus infer that the silicates were molten or partially molten when the cuspate-lobate grain boundaries formed. The texture is consistent with the Al-Cu-Fe metal grains being solid and the glass being a melt when they reacted to form the spinel crust and thin Al-oxide layer.

In Figure 2.3a, the glass (formerly matrix melt) appears to cross-cut the eutectoid regions, which would indicate a time sequencing: the now-cut Al-Cu-Fe alloy existed before the fracturing and intrusion of the silicate melt.

The preceding observations suggest that the 'metal-formation event' occurred prior to and is distinct from the event that produced the silicate melt. This is further supported by the presence of cuspate-lobate eutectoid boundaries (Fig. 2.3b), which have a fundamentally different texture than the angular eutectoid regions (Fig. 2.3a). We infer from the difference in texture that two different processes generated them. The rounded boundaries are consistent with the khatyrkite adjacent to the eutectoid regions being incorporated into partially re-melted eutectic melt. Because these regions were partially re-melted, they must have first formed prior to the event that led to the partial re-melting.

2.6 Al-Cu-Fe quasicrystals

2.6.1 Two generations

The upper and lower ends of the hollisterite grain terminate against an overgrowth of spinel crystals (Fig. 2.4a). We interpret this geometry to indicate a cross-cutting relationship that shows the hollisterite grain existed prior to the formation of the spinel layer, and, hence, the hollisterite grain is a pre-impact relict. This is further supported by the fact that the crust embays the contact between the hollisterite and stolperite where the arrow points to the crust in Fig. 2.4a. The icosahedrite grains lying immediately adjacent to the hollisterite (see Fig. 2.4b) must also be relicts,

and, thus, the icosahedrite grains are older than those formed during the most recent impact a few 100 Ma.

The i-II-bearing assemblage (Fig. 2.4c) occurs ~50 μm to the right of the hollisterite-bearing assemblage. The metal grains are similar in size (~15 μm). However, the i-II-bearing assemblage does not contain either hollisterite or i-I. Moreover, the textures in the i-II-bearing assemblages strongly suggest that these assemblages are not relicts but, rather, had solidified from completely re-melted metal following the 'impact event'. The enclosed phases, including the i-II phase, formed during a new crystallization sequence: the i-II phase crystallized first from the Al-Cu-Fe liquid; subsequently, the stolperite grew around the i-II phase, shielding the residual Al-Cu-Fe liquid from the i-II phase; within this residual liquid, the khatyrkite crystallized from a peritectic reaction. Finally, at the eutectic point, khatyrkite and Al formed together. The age of the i-II phase would thus be a few 100 Ma (the time of the latest impact).

With the i-I grains having formed prior to the impact event and the i-II phase having formed after, we can make the following conclusions: first, there are at least two generations of quasicrystals in Khatyrka; second, Khatyrka experienced conditions suitable for producing quasicrystals both prior to and during the 'impact event'; and, third, the Al-Cu-Fe metal assemblages experienced different degrees of melting during the 'impact event', with some completely melting (like the i-II-bearing assemblage, Fig. 2.4c), some only partially melting (like the eutectoid region in Fig. 2.3b), and others not melting at all (like the relict eutectoid in Fig. 2.3a).

2.6.2 Novel pathways for quasicrystal formation

The i-II phase is only the third quasicrystal to be discovered in nature. Its two predecessors (icosahedrite [21] and decagonite [50]) were discovered in nature *after* synthetic analogues had already been discovered. The synthetic analogue of icosa-

hedrite was discovered in 1987 [15], and the analogue of decagonite was discovered in 1989 [82]. In contrast, the i-II phase is the *first* quasicrystal to be discovered in nature *prior to* synthesis in the laboratory, despite the fact that the Al-Cu-Fe system has been systematically studied in the laboratory near the region of the i-I phase [17, 83, 84, 85]. At this time, it has yet to be synthesized in the laboratory, which indicates that there are processes for forming quasicrystals that have not been replicated in laboratory synthesis. Understanding what these processes are would inform new methods for synthesis and novel methods for uncovering new quasicrystals.

Equilibrium formation

The i-II phase may be an equilibrium phase (i.e., thermodynamically stable), and the reason why it has not been synthesized yet is that the stability field of the quasicrystalline phase in the Al-Cu-Fe ternary system shifts or expands at higher temperature and pressure conditions (present after shock) that have not yet been studied in the laboratory. A textural interpretation of the i-I and i-II assemblages suggests an equilibrium process. These assemblages are similar in size and in close proximity to one another, and both assemblages have textures (described above) that are consistent with solidification along liquid lines of descent with similar cooling rates but starting from different bulk compositions. We note that the two quasicrystal-bearing assemblages share resemblance to those obtained in the experiments reported in Figures 13 and 15 of [84].

Non-equilibrium formation

Alternatively, the i-II phase may be a non-equilibrium phase (i.e., kinetically stable but thermodynamically unstable), which has been preserved due to quench. Evidence that Khatyrka experienced highly non-equilibrium conditions has been found elsewhere, e.g., evidence of rapid quench and heterogeneous distribution of temper-

ature and pressure. Furthermore, laboratory shock experiments could be used to simulate non-equilibrium conditions to see whether they lead to the production of new quasicrystals.

The Asimow experiment

Indeed, a laboratory shock experiment has already been performed that successfully produced a novel quasicrystal [27]. We refer to this experiment—led by Paul Asimow—as the "Asimow experiment". The setup and the results (some unpublished) are discussed here.

The Asimow experiment was designed to simulate the impact shock conditions between possible starting materials in Khatyrka. The starting materials in the experiment consisted of a stainless steel recovery chamber made of 304SS ($Fe_{71}Cr_{18}Ni_8Mn_2Si_1$) enclosing a stack of discs of (in order from top to bottom, according to Fig. 2.8a) synthetic forsteritic olivine $(Mg_{0.75}Fe_{0.25})_2SiO_4$, synthetic $CuAl_5$ alloy composed of a eutectoid mixture of metallic Al and $CuAl_2$, natural FeNi from the Canyon Diablo meteorite, and a synthetic Al-bronze alloy ($Al_{14}Cu_4Fe_1Ni_1$). Some of these materials underwent a redox reaction, which produced metallic Fe beads and spinelloid group minerals (Fig. 2.9). The striking similarities between the products of the shock experiment and the phases observed in 126A (described in Sections 2.3 and 2.4) support our earlier conclusion that the impact event led to a reaction whereby FeO from the silicate melt was reduced by metallic Al from the Al-Cu-Fe metal.

The Asimow experiment also resulted unintentionally in the synthesis of a novel quasicrystal. Among the run products is a new quasicrystalline phase, shown in Fig. 2.8c, with icosahedral symmetry and with compositional range $Al_{68-73}Fe_{11-16}Cu_{10-12}Cr_{1-4}Ni_{1-2}$. Like the i-II phase, this new phase has an Fe/Cu ratio outside the range previously reported for Al-Cu-Fe-based quasicrystals. Its

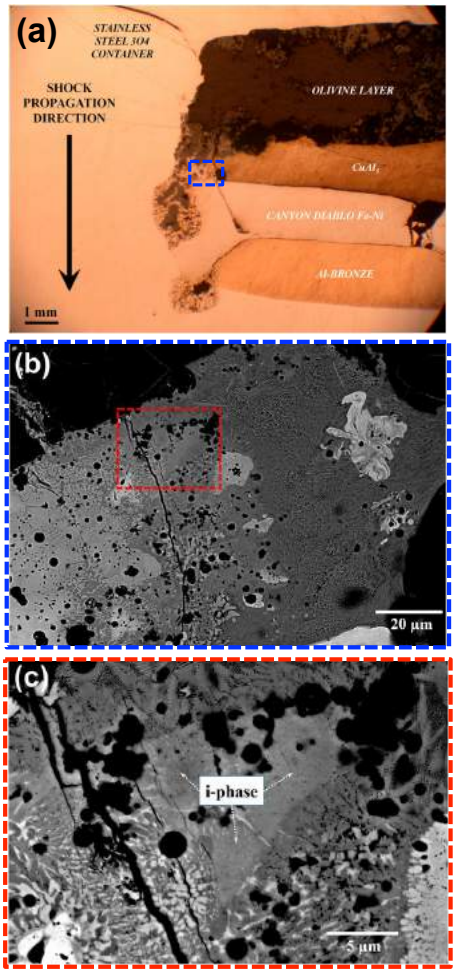

Figure 2.8: **Shock-synthesized icosahedral quasicrystal from the Asimow experiment.** (a) Reflected light photomicrograph showing layout of discs used in the Asimow experiment. Shown are the materials following the experiment, but the layout of the starting materials is clearly visible. The starting materials (from top to bottom) were: synthetic forsteritic olivine $(Mg_{0.75}Fe_{0.25})_2SiO_4$, synthetic $CuAl_5$ alloy composed of a eutectoid mixture of metallic Al and $CuAl_2$ (i.e., synthetic analogue of khatyrkite-Al eutectic mixture), natural FeNi from the Canyon Diablo meteorite, and synthetic Al-bronze alloy ($Cu_{14}Al_4Fe_1Ni_1$). The materials are contained in a stainless steel 304 chamber with composition $Fe_{71}Cr_{18}Ni_8Mn_2Si_1$. Arrow indicates shock propagation direction. (b) BSE image of magnified portion of blue-outlined region in (a). (c) BSE image of magnified portion of red-outlined region in (b), indicating the location of the new quasicrystal ("i-phase") with icosahedral symmetry and compositional range $Al_{68-73}Fe_{11-16}Cu_{10-12}Cr_{1-4}Ni_{1-2}$. Contrast in (b) and (c) have been stretched to emphasize differences of the metal phases. The dark spaces are not voids; they are grains of olivine and spinel.

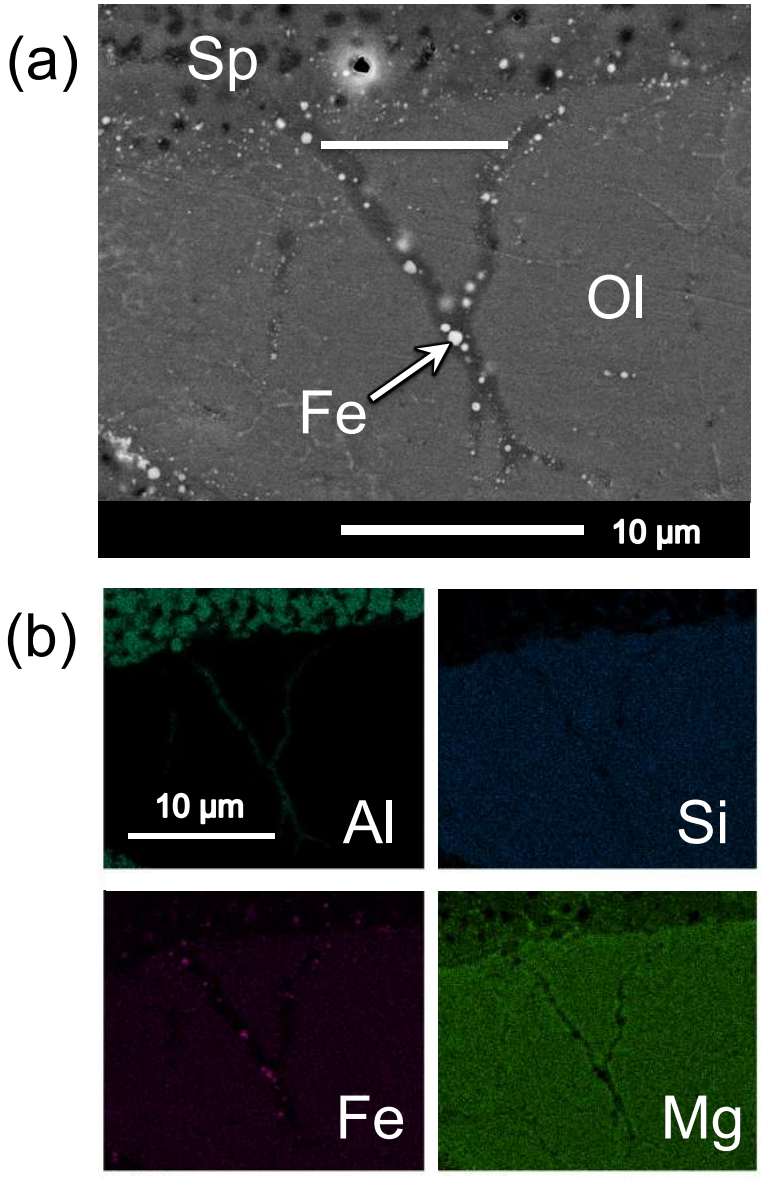

Figure 2.9: **Evidence of redox reaction from the Asimow experiment.** BSE image (a) and X-ray area maps (b) of a magnified region slightly above the blue-square-outlined area in Fig. 2.8a. A spinel-bearing glass ("Sp") appears to be a quenched melt, based on the observation of an apophysis cutting the olivine grain. Metallic Fe-beads ("Fe") occur within the apophysis and along the olivine ("Ol")-glass boundaries. The spinel and Fe-beads appear to be the products of redox reaction between the olivine and the $CuAl_5$ layers.

Al/(Cu+Fe) ratio is also outside the previously reported range [17, 64, 65]. The similarities observed between the Asimow experiment and 126A suggest they may have shared a common route for forming these new quasicrystals.

The experiment does not conclude whether the synthesis can be attributable to equilibrium formation (i.e., expanded thermodynamic stability at high pressure and temperature), non-equilibrium formation (i.e., kinetic pathways that exist with shock conditions), or a mixture of the two. Shock itself may be a sufficient condition for the formation of natural quasicrystals, but it may not be necessary. However, the experiment does demonstrate that shock recovery experiments provide a feasible way for forming and discovering new quasicrystals in the future. This presents an alternative to metallurgical methods that involve cooling (either quench or annealing) of bulk melts. A systematic study of the Al-Fe-Cu-Cr-Ni quinary system would have been impractical by existing metallurgical methods and computation, given the enormous number of bulk combinations possible among five elements.

2.7 Rapid cooling, heterogeneous temperature distribution, and new temperature constraints

The highly heterogeneous composition of the glass (as seen in the ternary diagrams in Fig. 2.5) and the presence of skeletal crystals (Fig. 2.7) indicate that the silicate melt cooled rapidly enough so that there was not enough time for compositional variations to be smoothed out by diffusion. Hence, 126A experienced at least two stages of extreme thermal changes caused by the latest impact event: first, a period of rapid heating, initiated by the impact and assisted by the aluminothermic reaction; and, subsequently, a rapid quench.

The effects of impact are heterogeneous at the grain scale. We can obtain local constraints—not on the entire body but for particular spots—on the temperature

attained during the 'impact event' by identifying phases that did not fully melt. For these temperature constraints, we assume ambient pressures—even though high-pressure phases were found in other fragments of 126 and in other grains of Khatyrka.

The presence of relict chondritic olivine implies that the meteorite was not 100% melted during the 'impact event'. Specifically, the presence of relict Fo_{77} implies that the peak temperature in these relict cores during the 'impact event' was no higher than ~1,700°C, the melting temperature of Fo_{77} at atmospheric pressure [86]. As discussed previously, the appearance and composition of these relict olivine grains is similar to the chondrule olivines observed elsewhere in Khatyrka [23].

Where the olivine was partially melted, we can infer that those regions were hot enough to melt olivine and pyroxene; hence, they were heated to at least 1,200°C, which is set by the solidus in the Fa-Fo-SiO_2 ternary [86]. This latter estimate is corroborated by the presence of Fe-silicide beads. The crystallization of these beads from the silicate melt implies that they experienced temperatures as high as 1,200°C, about the temperature of the solidi in the Fe-Si binary system [87]. This temperature estimate is also consistent with that obtained in [55] from an interpretation of ladder-like veins of ahrensite + SiO_2.

The Al-Cu-Fe metal yields a much lower peak temperature estimate, based on the relict eutectoid regions containing Al and khatyrkite. The cross-cut eutectoid regions (Fig. 2.3a) were heated to at most ~540°C, the Al-khatyrkite eutectic temperature [88]. If the peak temperature were higher, these regions would have completely re-melted and the cross-cutting relationship would not be preserved.

The very different peak temperature estimates from the relict metal eutectoid regions and the partially melted olivine regions, 540°C and 1,200°C respectively, reinforce the earlier conclusion that cold, solid metal was in contact with hot, molten matrix material during the 'impact event'. This also presents stark evidence for a heterogeneous distribution of temperatures in 126A following the 'impact event'.

We can also constrain the maximum peak temperatures for the hollisterite grain and the adjacent icosahedrite. As discussed previously, the cross-cutting relationship with the spinel crust indicates that these phases are relict. If these phases were heated above their melting temperatures after the onset of the aluminothermic reaction, they would have melted and the cross-cutting relationship would not be preserved. We conclude that the hollisterite and icosahedrite grains were heated to at most around 1,160°C and 1,100°C, their respective melting temperatures [17, 64, 89].

In those regions containing stolperite (e.g., the quasicrystal-bearing assemblages and the region shown in Fig. 2.6a) we can constrain the temperature at the time of quench, which may be different from the peak temperature. We interpret the texture as crystallization from a melt, with the stolperite grains appearing to be partially resorbed. The presence of stolperite implies that the temperature of the metal when it was quenched was not higher than the melting temperature of stolperite, which is around 640°C [84].

2.8 Discussion and Outlook

We assume for the purposes of simplicity that a single shock event is associated with the production of the high-pressure phases in 126 and in other grains, as well as with the silicate melt and redox reaction observed in 126A. Features in 126A and other samples indicate that this shock event produced a highly heterogeneous range of temperatures and pressures, followed by rapid cooling. Our interpretations are corroborated by the studies in [58] and [59] of noble gas measurements on forsteritic olivine fragments of Grain 126 (not from 126A) that show a high-velocity impact event occurred a few 100 Ma. This impact event resulted in shock stages ranging from S3 to S5 but most likely around S4 [60].

The textural relationships and evidence of redox reaction found in 126A clearly demonstrate that some of the Al-Cu-Fe alloy phases (including quasicrystals) formed prior to the impact event and some during, firmly establishing that the Al-Cu-Fe alloys (including icosahedrite) are extraterrestrial in origin and have a shared history with the chondritic material in outer space. The noble gas studies indicate that the first Al-Cu-Fe alloys formed over a few 100 Ma. However, the formation of the first Al-Cu-Fe alloys was probably no earlier than 4.564 Ga based on the absence of any evidence of excess ^{26}Mg (radiogenic from the decay of the short-lived nuclide ^{26}Al) in any of the measured Al-bearing metal grains from Khatyrka [22, 23]. (However, it is possible that any excess ^{26}Mg was reset during the most recent impact event.)

Our study also shows that the single event hypothesis' of [55] can be ruled out. In this hypothesis, the 'metal-forming event' and 'impact event' are the same. Although this hypothesis was favored for its simplicity, the results in this Chapter show that a more complex multiple-stage process is necessary to explain the observations: at the very least, a 'metal-forming event' was followed by one or more later 'impact-events,' with the most recent major impact occurring a few 100 Ma. Furthermore, the original 'metal-forming event' must have entailed highly reduced conditions, at least below the $(CuO+Al_2O_3)/CuAl_2$ buffer, in order to form khatyrkite. This makes it especially challenging to formulate a reasonable theory for how the Al-Cu-Fe metals first came to be, and is thus a subject of ongoing research. Speculations include: (i) condensation from the presolar nebula; and (ii) a carbon-mediated extraction process (i.e., smelting), which could take place, for example, upon extreme heating of neighboring Cu- and Al-rich phases within ureilite-like carbon-rich material (see [90] and [91] for further discussion on such a reduction mechanism).

One of the striking features of 126A reported here is the presence of unmelted Al-Cu alloy, with melting temperature ~540°C [88], in contact with silicate glass, with melting temperature ~1,200°C [86]. We note that [92] observed similar textures to

what we observe (Fig. 2.1) with respect to Fe-Ni metals in contact with silicates, in a study of three CB carbonaceous chondrites (Queen Alexandra Range (QUE) 94411, Hammadah al Hamra 237, and Bencubbin). One example, within QUE 94411, is a relict grain of Fe-Ni embedded in a shock melt (see Figure 7 of [92]). They argue that the precursor to the shock melt was fine-grained porous matrix material, and that, during a shock event, differences in shock impedance between denser, non-porous Fe-Ni metal and less dense, porous silicate matrix led to localized melting in the matrix material, which formed the now-observed shock melt. (See [60] and [93] for further discussion of disequilibrium shock effects.) The features observed in Grain 126A, including the contact between cold metal and silicate melt, can also be interpreted as the effects of highly localized, heterogeneous, shock-induced melting as a result of fine-scaled shock impedance variation. The main difference from the study of [92] and ours is that instead of relict Fe-Ni metal with melting temperature ~300°C [94], Grain 126A contains the relatively higher melting-point Al-Cu(-Fe) alloys.

We suggest that, after the silicate melt formed, the melt interacted with the Al-Cu-Fe metal grains as follows (see Fig. 2.10b for a schematic illustration): The Start panel in Fig. 2.10b represents the initial contact between silicate melt and cold metal. (Step 1) The Al-Cu-Fe metal, beginning at the grain boundaries, was partially assimilated into the melt. The metal-matrix interface retreated into the metal (indicated by arrows, Fig. 2.10b), leaving behind a modified matrix melt ("assimilated metal", Fig. 2.10b) with elevated concentrations of Al, Cu, and Fe. (Step 2) While the metal-matrix interfaces continued to retreat, the kinetic and chemical conditions were eventually suitable for ignition of an aluminothermic reaction near the interfaces, whereby Al was oxidized and Fe and Si were reduced ("reaction zone", Fig. 2.10b). (Step 3) The redox reaction and the retreat of the metal-matrix interface stopped. A layer of oxidized aluminum and a crust of aluminous spinel crystals grew on the metal grains into the modified matrix melt. Fe and Fe-silicide beads formed within the

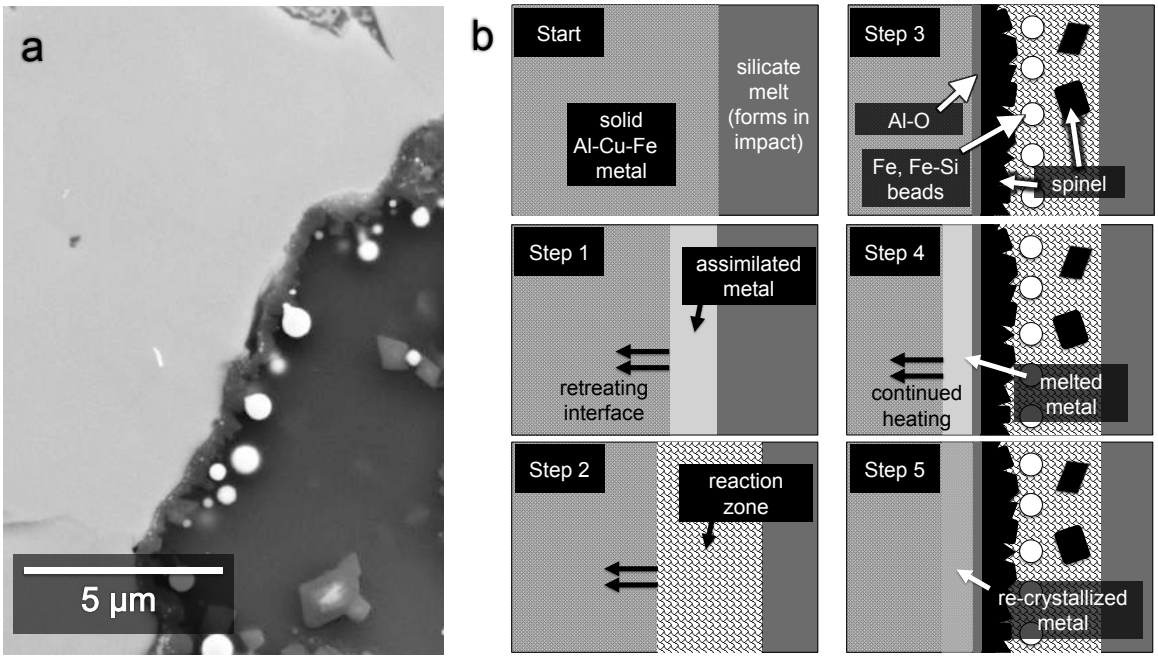

Figure 2.10: **Redox reaction at metal-matrix interface.** (a) BSE image showing close-up of Location f.8 (Fig. 2.2b). Metallic Fe beads occur mostly along interface between Al-Cu-Fe metal and glass. Spinel crust surrounds the Al-Cu-Fe metal grains. The Fe beads and spinel crust are the products of a redox reaction between Al-Cu-Fe metal and silicate melt. (b) Schematic illustration showing a proposed sequence of how the interaction unfolded between Al-Cu-Fe metal and silicate melt. The **Start** panel represents the initial contact between metal and silicate melt. In **Step 1**, the metal is being partially assimilated into the melt, which leads to an enrichment of Al, Cu, and Fe in the melt. The metal-matrix interface retreats into the metal. In **Step 2**, the interface continues to retreat, while the redox reaction occurs in the reaction zone, producing oxidized Al and metallic Fe and Si. In **Step 3**, the interface stops retreating and the redox reaction stops, as various phases begin to crystallize, including a layer of Al-oxide ("Al-O"), spinel crystals, and Fe and Fe-Si beads. In **Step 4**, the metal grains are still being heated. Some, like the one represented here, begin to melt, beginning at the metal-matrix interface. In **Step 5**, the system cools, and the newly melted metal regions re-crystallize. This final panel reflects what is observed in (a).

modified matrix melt, mostly along the metal-matrix interface, and alongside spinel crystals. These phases are indicated in Fig. 2.10b. At this stage, the Al-Cu-Fe metal grains—including those enclosed by a crust of spinel crystals—were still solid but continued to be heated. (Step 4) The metal grains heated to varying degrees. Some did not melt, others partially melted, and others completely melted. Represented in Fig. 2.10b is a melting grain, with the melt front advancing into the metal. (Step 5) Where there was newly melted metal encapsulated by the spinel crust, a new crystallization sequence occurred ("re-crystallized metal", Fig. 2.10b).

The new observations presented in this Chapter firmly establish that the quasicrystals and other metallic Al-bearing alloys in Khatyrka indeed formed in outer space. This should largely resolve the remaining uncertainty surrounding their natural origin. Looking forward, the discovery of the i-II phase in Khatyrka and the synthesis of a quinary quasicrystalline alloy in the Asimow experiment give us promise that further examples of exotic metallic alloy minerals and clues to their formation processes will eventually be discovered—perhaps as new and different types of meteorites are found and studied. The question of how the metallic Al was first reduced and then alloyed with Cu remains unanswered. Resolving this puzzling question would mark a new chapter in our understanding of stellar and geologic processes and of the early solar system.

2.9 Appendix: Methods

2.9.1 Sample characterization techniques

The sample studied here (Grain 126A) was first embedded in epoxy resin, prepared as a polished thick section, and coated with a 30-nm-thick carbon film. The results included here are from SEM-EDS (scanning electron microscopy, energy dispersive

spectroscopy) and EPMA-WDS (electron microprobe microanalysis, wavelength dispersive spectroscopy).

2.9.2 Scanning electron microscopy

X-ray compositional maps were obtained at the Centre for Electron Microscopy and Microanalysis (MEMA) of the University of Florence, Italy, using a Zeiss EVO MA15 SEM coupled with an Oxford INCA250 energy-dispersive spectrometer, operating at 25 kV accelerating potential, 500 pA probe current, and acquisition times of 10 ms per pixel. Further SEM-EDS studies were performed at Princeton University's Imaging and Analysis Center and at the Smithsonian Institution. Most of the SEM-EDS compositions presented in this Chapter were obtained at the GPS analytical facility at Caltech, using a GPS ZEISS 1550VP field emission SEM equipped with an angle-sensitive back-scattered electron (BSE) detector, an Oxford X-Max SDD EDS, and an HKL EBSD (electron backscatter diffraction) system. BSE imaging, EDS and EBSD analyses were conducted using SmartSEM, AZtec and Channel 5 software. EBSD analyses at a sub-micrometer scale were performed at 20 kV and 6 nA in focused beam mode with a 70° tilted stage and in a variable pressure mode (25 Pa), using methods described in [95] and [96]. The sample was vibro-polished to remove the carbon coat prior to EBSD analysis.

2.9.3 Electron microprobe

Quantitative elemental microanalysis was carried out at the GPS analytical facility at Caltech, using a JEOL 8200 electron microprobe (WDS mode, 12 kV and 5 nA for metals, 15 kV and 10 nA for silicates and oxides, focused beam). Counting times were 20 s on-peak and 10 s each on upper and lower background positions. Data reduction used the CITZAF routine built into the Probe for EPMA software. Standards used for metals were: pure metal standards (Al, Si, Cr, Fe, Ni, Cu), forsterite (Mg) and

anorthite (Ca). Standards used for silicate, oxide, and glass phases were: forsterite (Si, Mg), fayalite (Fe), albite (Na), microcline (K), anorthite (Ca, Al), Cr_2O_3 (Cr), NiO (Ni), apatite (P) and metal-Cu (Cu). For the spinel regions, it was difficult to obtain clean analyses of the small individual crystals. This resulted in weight percent totals for the spinel phases that deviated by several percentage points from the ideal 100% and spinel analyses that regularly contained >1 weight % SiO_2, which is apparently from glass and/or olivine from the surroundings or from underneath. In the spinel compositions presented in Table 2.2c, we have included in the average only individual analyses whose weight % totals were between 90 and 110%. The total shown in the rightmost column is the averaged total.

Chapter 3

Hyperuniformity variation with local isomorphism classes

The choice of orientatational symmetry, quasiperiodicity, and set of fundamental repeating units (e.g., tiles, atoms, molecules) does not uniquely specify a quasicrystal. In fact, there are infinitely many possible space-filling arrangements of the same repeating units, with the same symmetry and same support for their diffraction patterns [8, 10, 11, 12]. They can be grouped into *local isomorphism* (LI) *classes*; two quasicrystals are in the same LI class if, and only if, any local configuration of the repeating units found in one can be found with the same frequency in the other. In this Chapter and the next, we report on two studies of local isomorphism classes of quasicrystals.

3.1 Introduction

All quasicrystals have long-wavelength density fluctuations that, like crystals and special amorphous systems, are suppressed relative to typical structurally disordered systems; this large-scale structural property is known as *hyperuniformity* [29, 30, 31]. Whether the degree of hyperuniformity, as measured by the leading coefficient of the

number variance (defined in Section 3.2), varies with LI class is an open question. If it does vary, then it would be of interest to understand the following: (1) What specific structural properties of an LI class determine the degree of hyperuniformity; and, (2) How do these structural properties affect the physical properties, e.g., electromagnetic, electronic, mechanical properties?

On one hand, one might think the degree of hyperuniformity would not vary with LI class, given what they have in common: the same symmetry, fundamental repeating units, support for their diffraction patterns. They are also quite similar in their construction. With the direct projection method, different LI classes can be generated from using the same acceptance window (same shape and orientation) to select a subset of points from the same hypercubic lattice that project onto the same projection space. Their construction differs only in the position of the acceptance window in the direction orthogonal to the projection space.

On the other hand, one might think the degree of hyperuniformity *would* vary with LI class, with the following reasoning: We know that changing the decoration of the fundamental unit cell of crystals affects the degree of hyperuniformity. (This can be seen, e.g., with the triangular, kagome and honeycomb crystals [29, 30].) Although different LI classes have identical fundamental repeating units (e.g., tiles in the case of quasicrystal tesselations) and identical Bragg peak positions, their diffraction patterns have different scattering intensities (similar to what occurs by changing the decoration of the unit cell in a crystal pattern). Also, with the direct projection method, while the acceptance window is the same for the different LI classes, when the hypercubic lattice points are projected into the space that includes the acceptance window, they are confined to planes that cut the acceptance window in different ways for different LI classes. Therefore, one could consider the different LI classes as having different accpetance windows, if one took the set of projected planes as the "acceptance window".

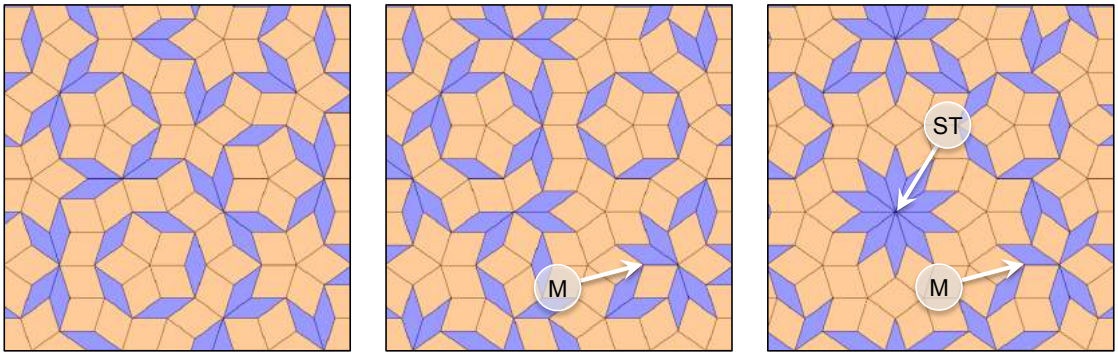

Figure 3.1: **Tilings from three different LI classes.** The Penrose tiling is shown at the left. From left to right, they correspond to $\gamma = 0$, $\gamma = 0.2$, and $\gamma = 0.5$. Though all are constructed from the same fat (orange) and skinny (violet) tiles, they differ in their distribution of vertex environments. The ST vertex is absent in the $\gamma = 0$ and $\gamma = 0.2$ LI classes. The M vertex is absent in the $\gamma = 0$ class. (See Figure 3.4 for notation and enumeration of the sixteen distinct vertex environments.)

In this Chapter, we examine how the degree of hyperuniformity varies with LI class and why. The results we present clearly show that the latter intuition—that the degree of hyperuniformity varies with LI class—is correct. We study a continuous set of LI classes of two-dimensional, pentagonal quasicrystal tilings, which can be obtained as duals to a multigrid composed of five overlapping sets of periodically spaced lines or as direct projections from a five-dimensional hypercubic lattice [11, 97, 98]. The set of tilings includes a continuum of configurations with five-fold symmetry and discrete instances with ten-fold symmetry, which includes the Penrose tiling [14]. Examples from different LI classes are shown in Figure 3.1. In determining their degree of hyperuniformity, we treat the quasicrystal tilings as point patterns, with points at the vertices of the tiles.

We begin in Section 3.2 by providing a brief review of the notion of hyperuniformity and defining our choice of how to measure the degree of hyperuniformity, which will be denoted by $\overline{\Lambda}(\infty)$. Then, in 3.3, we describe how to mathematically construct the quasicrystals studied in this Chapter and establish some terminology. Section 3.4 details our numerical methods for determining $\overline{\Lambda}(\infty)$. Finally, in Section 3.5, we

present and discuss our main results, which show that $\overline{\Lambda}(\infty)$ varies continuously with the LI class, has a global minimum at the Penrose LI class, and has local minima at a special denumerable subset of LI classes known as *restorable* [99]. A restorable LI class is one that, roughly speaking, has a lower variance in its local neighborhoods than do nearby LI classes. We also present empirical evidence indicating that the overall trend in $\overline{\Lambda}(\infty)$ can be attributable to the distribution of vertex environments.

3.2 Hyperuniformity

3.2.1 Defining the degree of hyperuniformity

The notion of hyperuniformity can be formulated as follows: Given a point pattern in d-dimensional Euclidean space $\mathbb{R}^d$, we let $N(R;\mathbf{x}_0)$ be the number of points within a hyperspherical window of radius R with center at position $\mathbf{x}_0$, which is a random variable. For a fixed R, we let $\sigma^2(R) \equiv \langle N^2(R)\rangle - \langle N(R)\rangle^2$ be the number variance associated with this random variable. For typical disordered systems, $\sigma^2(R)$ asymptotically follows a volume law $\sigma^2(R) \sim R^d$. A system is said to be *hyperuniform* if $\sigma^2(R)$ grows more slowly than the volume of the window, i.e.,

$$\sigma^2(R) \sim R^{\alpha} \ , \tag{3.1}$$

where $\alpha < d$. All ideal crystals and many quasicrystals are hyperuniform with $\alpha = d–1$ [29, 30, 100], as are special disordered systems (a recent review of hyperuniform disordered systems can be found in [31]).

Our numerical results suggest that the particular quasicrystal tilings studied here are also hyperuniform with $\alpha = d-1$, implying their local number variance has the

asymptotic behavior [29, 30]

$$\sigma^2(R) \sim \Lambda(R)R + o(R) \ , \tag{3.2}$$

where $\Lambda(R)$ is a bounded function that fluctuates around some average value, and $o(R)$ denotes terms of lower order than R. We therefore conjecture that the same holds for the entire continuous set of LI classes explored in this Chapter. It is useful to average out the small-scale variations in $\Lambda(R)$ and consider the running (cumulative moving) average $\overline{\Lambda}(R)$ [101] and the global average $\overline{\Lambda}(\infty)$ [29, 30], which are defined as follows:

$$\overline{\Lambda}(R) \equiv \frac{1}{R}\int_0^R \Lambda(R')dR' \ , \tag{3.3}$$

and

$$\overline{\Lambda}(\infty) \equiv \lim_{R\to\infty} \overline{\Lambda}(R) \ . \tag{3.4}$$

In Figure 3.2, we show $\Lambda(R)$ (purple), $\overline{\Lambda}(R)$ (red), and $\overline{\Lambda}(\infty)$ (black, dashed) for the three tilings in Figure 3.1. Following [29] and [30], we shall use $\overline{\Lambda}(\infty)$ to characterize the *degree of hyperuniformity* of a given system.

3.2.2 Alternative formulations of hyperuniformity

Other formulations of hyperuniformity, described below, may be more suitable for measuring the degree of hyperuniformity in other systems. These alternative formulations may not be as efficient for estimating $\sigma^2(R)$ when closed-form expressions of the pair correlation function $g(\mathbf{r})$ or the structure factor $S(\mathbf{k})$ are not known, as is the case for the quasicrystalline point patterns studied here.

We begin with a formulation of hyperuniformity in terms of $S(\mathbf{k})$ [29]. Assuming the system is statistically homogeneous (i.e., correlation functions depend only on the relative positions of points and not on their absolute positions), $S(\mathbf{k})$ can be written

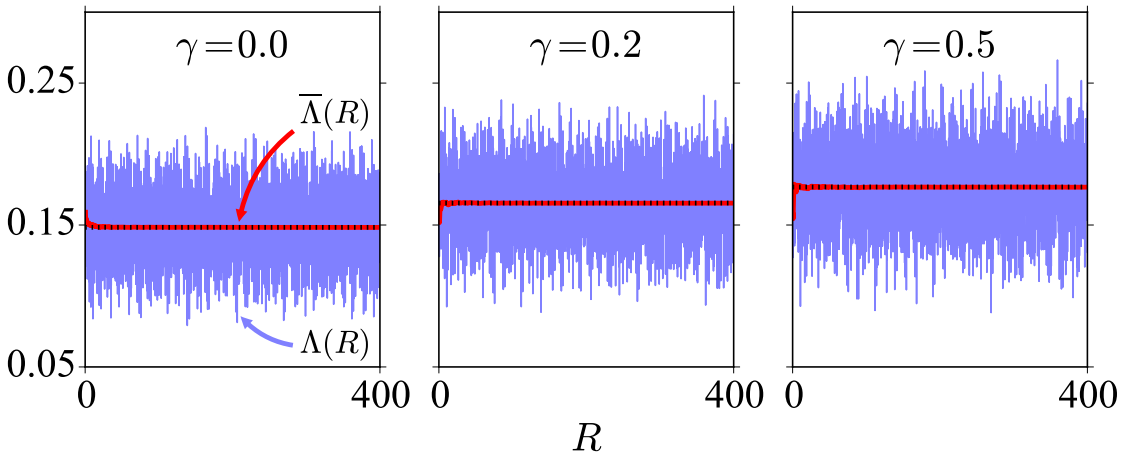

Figure 3.2: **Leading coefficient of the local number variance.** The small-scale function $\Lambda(R)$ (purple), running average $\overline{\Lambda}(R)$ (red), and global average $\overline{\Lambda}(\infty)$ (dashed black line), as defined in the text are shown, calculated for the three tilings in Figure 3.1. The running average $\overline{\Lambda}(R)$ and the global average $\overline{\Lambda}(\infty)$ are indistinguishable for all but the smallest values of R. The small-scale function $\Lambda(R)$ appears to have bounded variations.

as

$$S(\mathbf{k}) = 1 + \rho\tilde{h}(\mathbf{k}) \ , \tag{3.5}$$

where ρ is the number density (i.e., the average number of points per unit area), $\tilde{h}(\mathbf{k})$ is the Fourier transform of the total correlation function $h(\mathbf{r}) = g(\mathbf{r}) - 1$, and a delta-function peak at $\mathbf{k} = 0$ has been subtracted out. A hyperuniform system is one in which

$$\lim_{k\to 0} S(\mathbf{k}) \to 0 \ , \tag{3.6}$$

where $k = |\mathbf{k}|$ is the modulus of $\mathbf{k}$.

The local number variance is related to the structure factor by

$$\sigma^2(R) = \rho v_1(R) \left[\frac{1}{(2\pi)^d} \int_{\mathbb{R}^d} S(\mathbf{k}) \tilde{\alpha}_2(\mathbf{k}; R) d\mathbf{k} \right] \ , \tag{3.7}$$

where $\tilde{\alpha}_2(\mathbf{k}; R)$ is the Fourier transform of the scaled intersection volume $\alpha_2(\mathbf{r}; R)$, which is the volume of overlap between two hyperspheres of radius R with centers

separated by $\mathbf{r}$, normalized by the volume of a single hypersphere $v_1(R)$. For systems that are both statistically homogeneous and statistically isotropic (i.e., correlation functions depend only on the distances between points), the structure factor depends only on the modulus of $\mathbf{k}$, i.e., $S(\mathbf{k}) = S(k)$. For such hyperuniform systems, when $S(k) \sim k^\beta$ ($\beta > 0$) for small k,

$$\sigma^2(R) = \begin{cases} R^{d-\beta} \ , & \beta < 1 \\ R^{d-1} \ln R \ , & \beta = 1 \\ R^{d-1} \ , & \beta > 1 \end{cases} \tag{3.8}$$

for large R. The $\beta \leq 1$ cases follow from Eq. (3.7) using $v_1(R) \propto R^d$ and expanding $\tilde{\alpha}_2(\mathbf{k}; R) \propto k^{-d} \left(J_{d/2}(kR)\right)^2$ in k, where $J_\nu(x)$ is the Bessel function of the first kind of order ν. The $\beta > 1$ case follows from the fact that $\sigma^2(R)$ cannot grow more slowly than R^{d-1} [29].

For quasicrystals, $S(\mathbf{k})$ is composed of dense Bragg peaks whose intensities do not decrease monotonically as $k \to 0$. Therefore, one cannot obtain the exponent α in Eq. (3.1) directly from the small-k behavior of $S(\mathbf{k})$. To determine the scaling exponent α for quasicrystals has motivated yet a third formulation for hyperuniformity in terms of an integral over $S(\mathbf{k})$ [100]. After integration by parts, Eq. (3.7) can be written as

$$\sigma^2(R) = -\rho v_1(R) \left[\frac{1}{(2\pi)^d} \int_0^\infty Z(k) \frac{\partial \tilde{\alpha}_2(k; R)}{\partial k} dk \right] \ , \tag{3.9}$$

where $Z(k) = \int_{|\mathbf{q}|<k} S(\mathbf{q}) d\mathbf{q}$ is called the *integrated spectral density intensity*. For one-dimensional quasicrystals, it has been shown (rigorously for some cases, numerically for others) that $Z(k)$ is bounded above and below by curves $c_+ k^{1+\alpha}$, $c_- k^{1+\alpha}$, where c_-, c_+ are constants, and α is the scaling exponent in Eq. (3.1) [100].

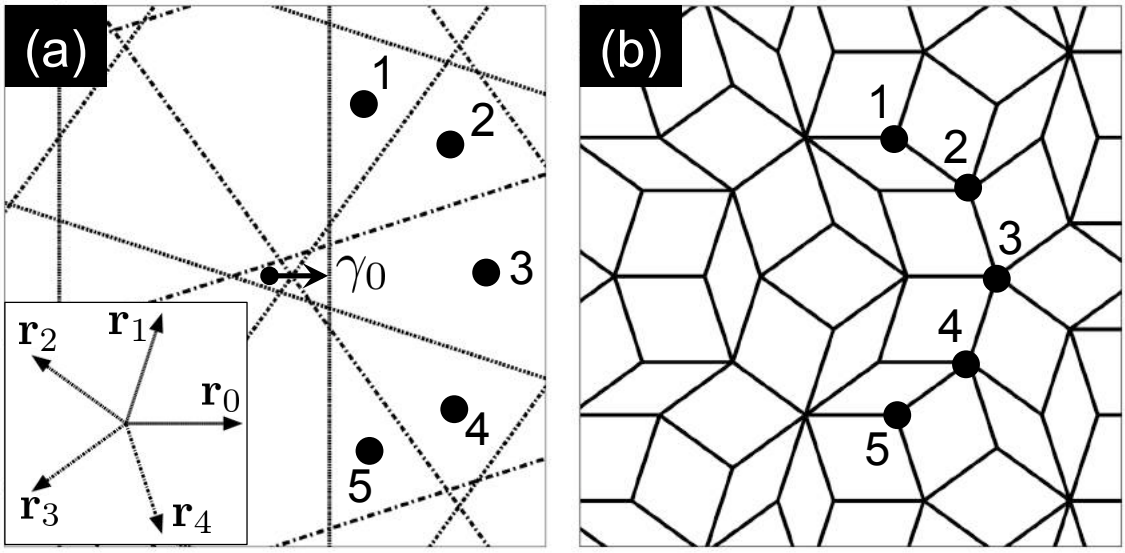

Figure 3.3: **Schematic illustration of the dual method.** (a) Periodic pentagrid, consisting of five grids (overlapping sets of periodically spaced lines), each normal to one of the five vectors $\mathbf{r}_i$ (inset). Each grid has been displaced from the origin by a finite phase γ_i. The extent of the 0th phase γ_0 is marked. Five open regions have been numbered. (b) Tiling obtained by applying the dual transformation to the pentagrid in (a). Vertices corresponding to the five numbered open regions in (a) are shown.

3.3 Quasicrystals

We now turn to the construction of the two-dimensional pentagonal quasicrystals studied in this Chapter. Two equivalent methods are presented. We establish that the LI classes can be continuously parameterized by a number γ and define the condition for when two LI classes are locally isomorphic. The notion of restorability is introduced, which is useful to understand how $\overline{\Lambda}(\infty)$ varies with γ.

3.3.1 Dual method

A *grid* is an infinite set of parallel, straight lines, labeled by $n \in \mathbb{Z}$ corresponding to their ordinal position in the grid. A *multigrid* is the union of multiple grids in which no two grids are parallel, and in which the ith grid is oriented normal to the vector $\mathbf{r}_i$. A *periodic multigrid* is one in which the spacing between adjacent gridlines is equal.

The set of vectors $\mathbf{r}_i$ are called *star vectors*. They determine the orientational order of the resulting tiling: every tile edge is oriented parallel to one of the star vectors. The displacement γ_i of the ith grid from the origin is called the *phase*.

The multigrid partitions space into open regions, each of which can be uniquely labeled by a set of N integers $\mathbf{K} \equiv (k_1, k_2, \ldots, k_N)$ such that, if $\mathbf{x}$ is any point within the region, it lies between lines k_i and $k_i + 1$ of the ith grid. The dual method maps these open regions $\mathbf{K}$ to the vertices $\mathbf{t}$ of a tiling, according to the transformation $\mathbf{t} = \sum_{i=1}^{N} k_i \mathbf{r}_i$. Open regions that share an edge are mapped to vertices connected by an edge.

The tilings studied in this Chapter are dual to *periodic pentagrids*, which are periodic multigrids with star vectors $\mathbf{r}_i = (\cos 2\pi i/5, \sin 2\pi i/5)$ $(i = 1, 2, \ldots, 5)$. The vectors $\mathbf{r}_i$ point to the corners of a pentagon; therefore, the resulting tilings will have five-fold orientational order. The tilings so constructed comprise two rhombuses of equal sides but with angles of $2\pi/5$ ("fat") and $2\pi/10$ ("skinny"). The ratio of the numbers of fat and skinny tiles equals $\tau = (1 + \sqrt{5})/2 \approx 1.618$, the golden ratio. The sum of the phases $\gamma = \sum_{i=i}^{5} \gamma_i$ labels the LI class.

3.3.2 Direct projection method

The dual method is the most general method for generating quasicrystals. It can be used to generate quasicrystals that cannot be generated by other methods (e.g., direct projection, inflation/substitution). However, the quasicrystals studied in this Chapter are the same as those that can be generated by the direct projection method. Hence, the tilings are referred to as "direct projection tilings" (DPTs). Here, we review the direct projection method for constructing pentagonal tilings.

With the direct projection method, the tiles are obtained by projecting a subset of points from a five-dimensional hypercubic lattice $\mathbb{Z}^5$. One divides real space $\mathbb{R}^5$ into two subspaces: a two-dimensional *physical space* $\mathbb{R}^2_{\parallel}$ spanned by the unit vectors

$$\begin{aligned}
\mathbf{a}_{\parallel}^{1} &= \sqrt{\tfrac{2}{5}}\Big(1, \cos\tfrac{2\pi}{5}, \cos\tfrac{4\pi}{5}, \cos\tfrac{6\pi}{5}, \cos\tfrac{8\pi}{5}\Big)\ , \\
\mathbf{a}_{\parallel}^{2} &= \sqrt{\tfrac{2}{5}}\Big(1, \sin\tfrac{2\pi}{5}, \sin\tfrac{4\pi}{5}, \sin\tfrac{6\pi}{5}, \sin\tfrac{8\pi}{5}\Big)\ ,
\end{aligned} \tag{3.10}$$

and a three-dimensional *perpendicular space* $\mathbb{R}_{\perp}^{3}$ spanned by the unit vectors

$$\begin{aligned}
\mathbf{a}_{\perp}^{1} &= \sqrt{\tfrac{2}{5}}\Big(1, \cos\tfrac{4\pi}{5}, \cos\tfrac{8\pi}{5}, \cos\tfrac{2\pi}{5}, \cos\tfrac{6\pi}{5}\Big)\ , \\
\mathbf{a}_{\perp}^{2} &= \sqrt{\tfrac{2}{5}}\Big(1, \sin\tfrac{4\pi}{5}, \sin\tfrac{8\pi}{5}, \sin\tfrac{2\pi}{5}, \sin\tfrac{6\pi}{5}\Big)\ , \\
\mathbf{a}_{\perp}^{3} &= \sqrt{\tfrac{1}{5}}\Big(1, 1, 1, 1, 1\Big)\ .
\end{aligned} \tag{3.11}$$

Points of the tiling are obtained from the projection onto $\mathbb{R}_{\parallel}^{2}$ of a subset $\mathcal{C} \subset \mathbb{Z}^5$ composed of points which, when projected onto $\mathbb{R}_{\perp}^{3}$, fall within the projection of a unit hypercube $\mathcal{W}$. The body diagonal of $\mathcal{W}$ is oriented parallel to $\mathbf{a}_{\perp}^{3}$, and the projection of $\mathcal{W}$ onto $\mathbb{R}_{\perp}^{3}$, a rhombic icosahedron in the case of pentagonal symmetry, is called the *acceptance volume*. Neighboring points in $\mathbb{Z}^5$ that are accepted in $\mathcal{W}$ are projected onto vertices connected by an edge. Translations of $\mathcal{W}$ along $\mathbf{a}_{\perp}^{1}, \mathbf{a}_{\perp}^{2}$ correspond to phason displacements; tilings related by phason displacements are locally isomorphic. Translations of $\mathcal{W}$ along $\mathbf{a}_{\perp}^{3}$ result in changes in LI class. The LI class label γ is the sum of the components of the offset $(\gamma_0, \gamma_1, \ldots, \gamma_4)$ of $\mathcal{W}$ from the origin in $\mathbb{R}^5$: $\gamma = \sum_{i=0}^{4} \gamma_i$.

3.3.3 Local isomorphism and restorability

Two tilings are said to be *locally isomorphic* if any configuration of tiles in any finite region from one will occur with the same frequency in the other. It can be shown [11] that two tilings are locally isomorphic (up to inversion) if, and only if, the sum

of the phases $\gamma \equiv \sum_{i=0}^{4} \gamma_i$, $\gamma' \equiv \sum_{i=0}^{4} \gamma_i'$ are related by

$$\left|-\tfrac{1}{2} + \{\gamma\}\right| = \left|-\tfrac{1}{2} + \{\gamma'\}\right| \tag{3.12}$$

where $\{\gamma\}$ denotes the fractional part of γ. An arbitrary γ can be mapped to a locally isomorphic γ' that lies within the range $[0, 0.5]$ via

$$\gamma' = \tfrac{1}{2} - \left|-\tfrac{1}{2} + \{\gamma\}\right| \ . \tag{3.13}$$

If $\gamma, \gamma' \in [0, 0.5]$ and $\gamma \neq \gamma'$, then γ, γ' are not locally isomorphic.

To understand how $\overline{\Lambda}(\infty)$ varies with γ, it is useful to characterize the tile configurations of the different LI classes. For this, we employ the concepts of r-maps and r-atlases: Given a tiling, select a vertex and construct a circle of radius r centered at that vertex. The collection of all tiles that are entirely contained within the circle is called an *r-map*. Repeat this for every vertex in the tiling. The resulting collection of r-maps is called the *r-atlas* for that tiling (taking out duplicates and configurations equivalent under reflections and rotations).

An LI class is said to be *restorable* if there is some finite R_r, called the *restorability radius*, such that the R_r-atlas is unique to that LI class, among all DPTs. A restorable LI class γ with restorability radius R_r has the property that its R_r-atlas contains the fewest number of R_r-maps, compared to LI classes with $\gamma' = \gamma \pm \delta\gamma$, in the limit $\delta\gamma \to 0$. For DPTs, it has been shown that the only restorable LI classes are those with $\gamma = n\tau$, where $n \in \mathbb{Z}$ and $\tau = (1 + \sqrt{5})/2 \approx 1.618$ is the golden ratio [99]. For the $\gamma = n\tau$ class, R_r is proportional to n. That is, as n increases, one must consider all tile configurations out to larger and larger sizes to distinguish the $\gamma = n\tau$ class from all other LI classes.

Also useful in our discussion of how $\overline{\Lambda}(\infty)$ varies with γ is the notion of vertex environments. A *vertex environment* is defined to be a collection of tiles sharing a

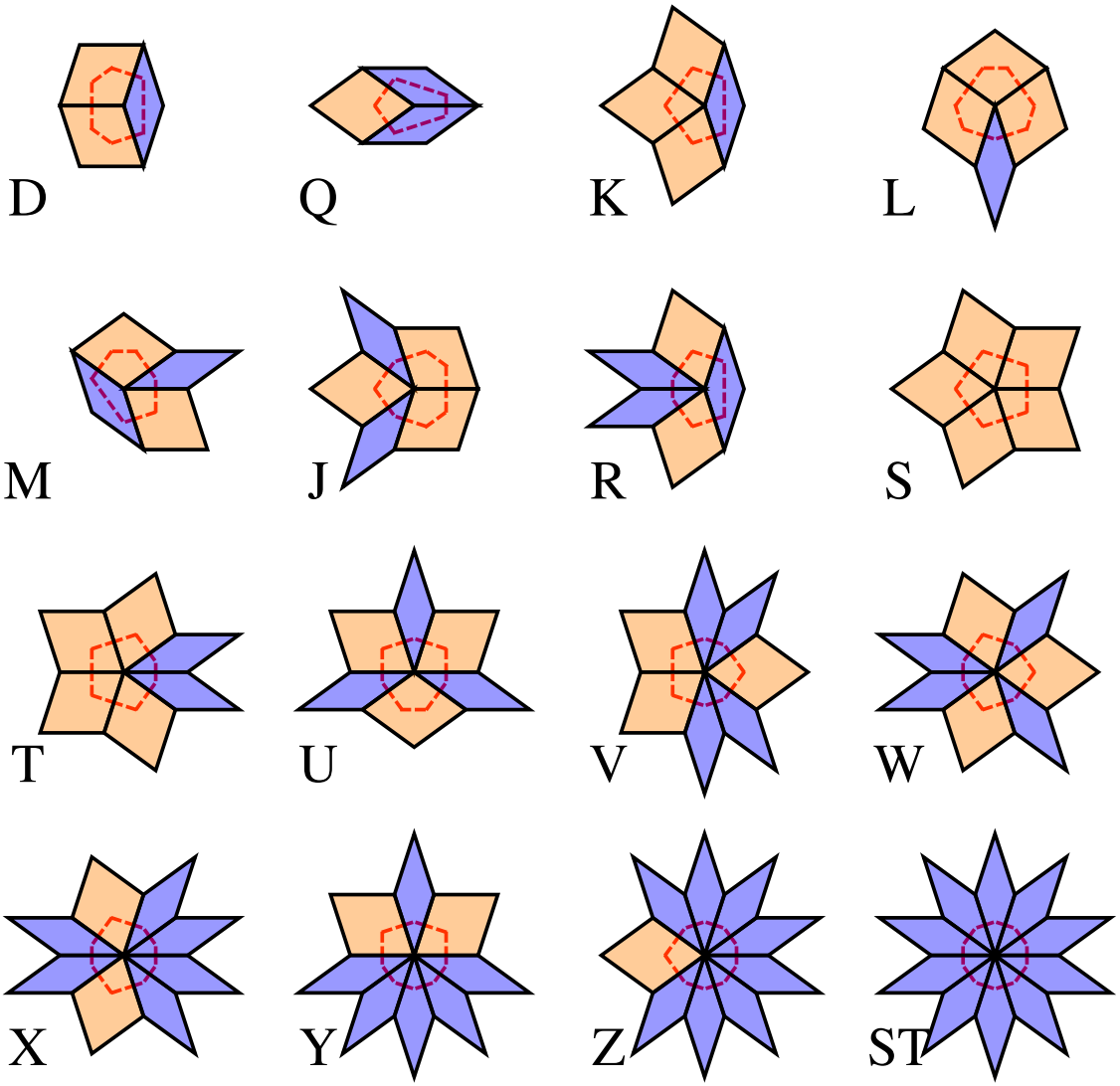

Figure 3.4: **The sixteen distinct vertex environments.** The vertex environments are constructed from fat (orange) and skinny (violet) tiles. The Voronoi areas are outlined in dashed, red lines. Notation follows that of [97], [98] and [102].

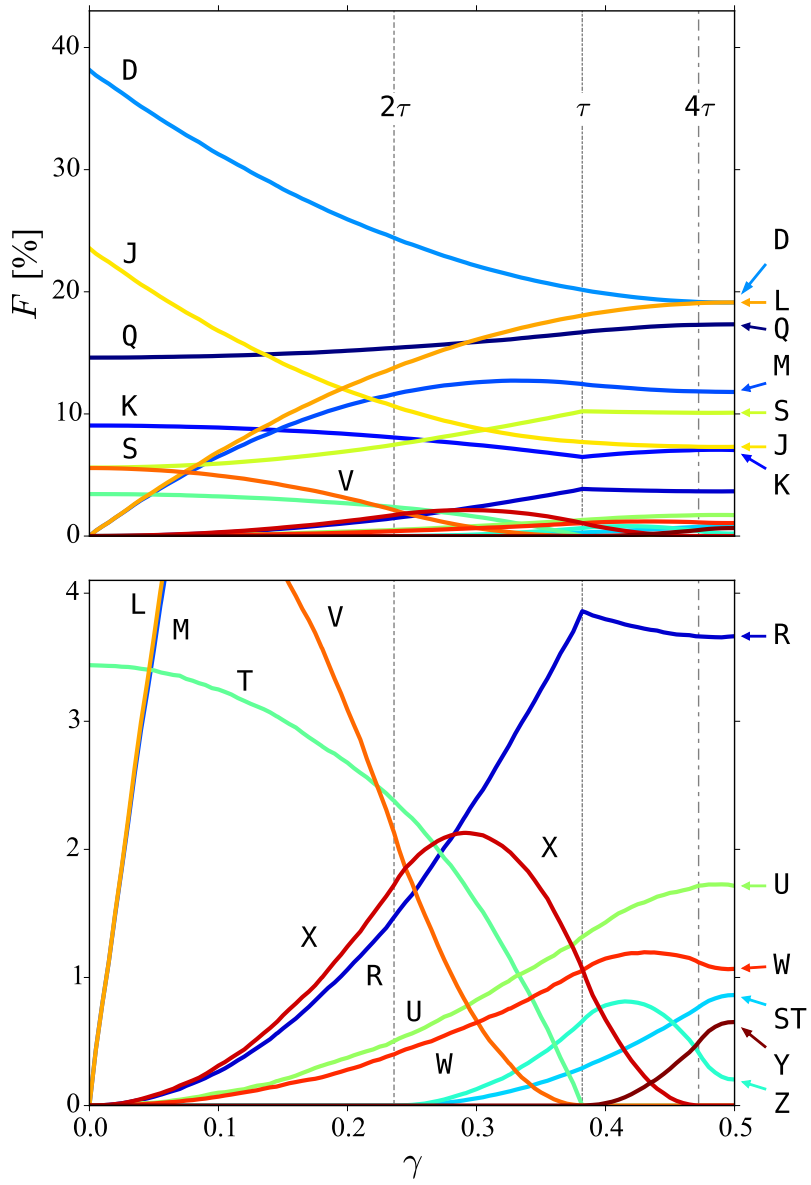

Figure 3.5: **Frequencies F of the sixteen vertex environments *versus* LI class γ.** The vertex environments are shown in Figure 3.4. The lower portion of the top panel is magnified in the bottom panel. Dashed vertical lines mark $\gamma \approx 0.236, 0.382, 0.472$, which correspond to $\gamma = 2\tau, \tau, 4\tau$; at these values of γ (and at $\gamma = 0$), certain vertex environments appear or disappear. Frequencies were calculated in [103] but have been independently re-calculated here.

common vertex. Up to rotations and reflections, there are sixteen distinct vertex environments (shown in Figure 3.4) that can be constructed from the skinny and fat rhombuses. Each LI class has a characteristic distribution of vertex environments [102, 103, 104]. The distribution of vertex environments for the different LI classes is shown in Figure 3.5.

Among all restorable LI classes, the Penrose LI class ($\gamma = 0$) has the smallest restorability radius. It is also distinguished for having the fewest distinct vertex environments.

3.4 Determining $\overline{\Lambda}(\infty)$

In this section, we describe how we numerically estimate the degree of hyperuniformity $\overline{\Lambda}(\infty)$, defined by Eq. (3.4), for the different LI classes.

We first generate a DPT from LI class γ using the dual method. This is necessarily a finite portion of the perfect, infinite tiling and is not a periodic approximant. Treating the tilings as point patterns, with points at the vertices of the tiles, we estimate the local number variance $\sigma^2(R)$ by, first, counting the number of points $N(R;\mathbf{x}_i)$ lying within M circular sampling windows of radius R with centers at positions $\mathbf{x}_i$ $(i = 1, \ldots, M)$, then calculating the variance in these counts as follows:

$$\sigma^2(R) = \frac{1}{M}\sum_{i=1}^{M} N(R;\mathbf{x}_i)^2 - \frac{1}{M^2}\left(\sum_{i=1}^{M} N(R;\mathbf{x}_i)\right)^2 . \tag{3.14}$$

This is repeated for a set of radii R_i, uniformly distributed between $R_{\min}$ and $R_{\max}$.

The window centers $\mathbf{x}_i$ are uniformly distributed within a circular region of radius $R_{\max}$ about the center of mass of the quasicrystal point pattern. The fiducial area, which contains all points that can be sampled, is a circular region about the center of mass of radius $2R_{\max}$. The DPT must be sufficiently large to contain within its

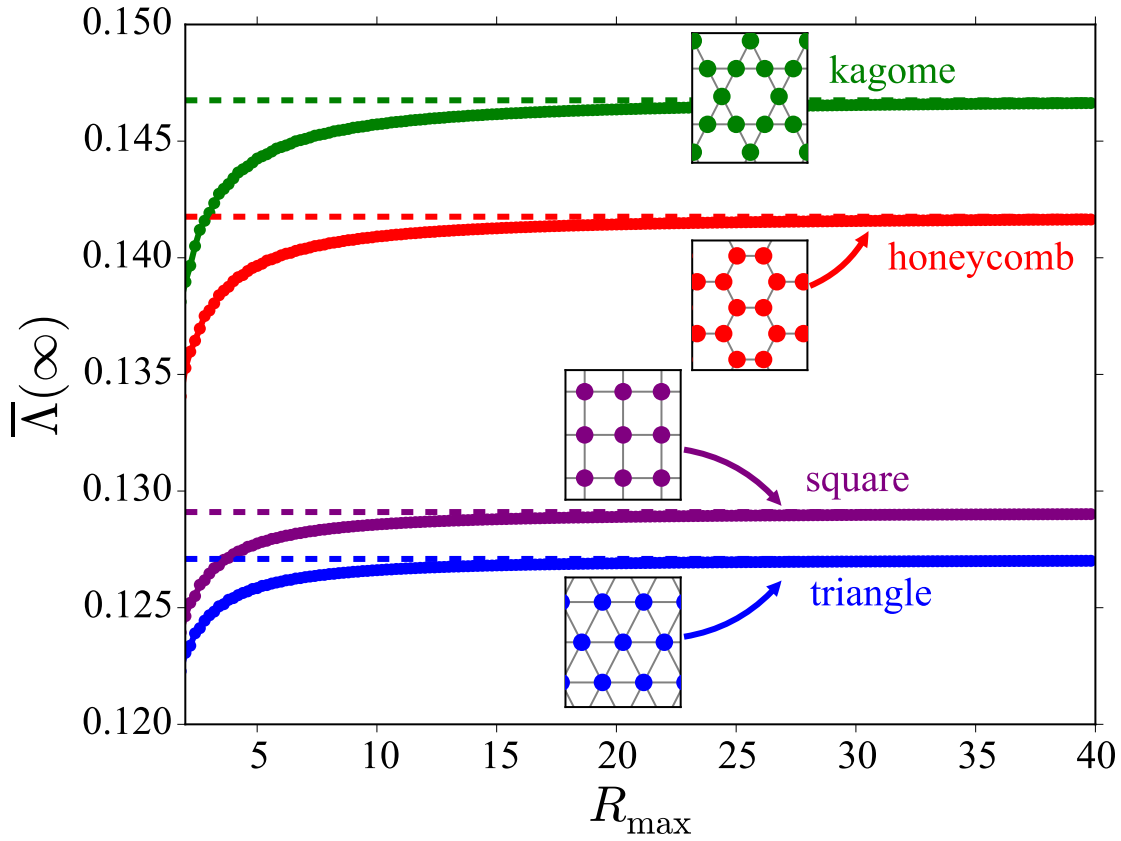

Figure 3.6: **Convergence test of $\overline{\Lambda}(\infty)$ for crystalline point patterns.** Estimates of the degree of hyperuniformity $\overline{\Lambda}(\infty)$, as the upper integration limit $R_{\max}$ is varied, for kagome, honeycomb, square, and triangle crystal point patterns. The ideal values are overlaid in dashed lines (from [29] and [30]).

boundaries this fiducial area. (We have found that a sufficiently large DPT can be generated from a pentagrid containing $2R_{\max}/a$ grid lines per grid.)

We calculate the running average $\overline{\Lambda}(R)$ by using a trapezoidal rule to numerically integrate Eq. (3.3) up to $R_{\max}$:

$$\overline{\Lambda}(R_i) \equiv \frac{1}{R_i - R_{\min}} \sum_{j=2}^{i} \frac{\lambda_{j-1} + \lambda_j}{2} \Delta R_j \ , \tag{3.15}$$

where

$$\lambda_j \equiv \frac{1}{2\sqrt{\pi\rho}} \left(\frac{\sigma^2(R_j)}{R_j} \right) \tag{3.16}$$

and $\Delta R_j \equiv R_j - R_{j-1}$. The coefficient $1/\left(2\sqrt{\pi\rho}\right)$ is included in Eq. (3.16) so that the results are independent of the number density ρ (the number of points per unit area). Our estimate of the global average $\overline{\Lambda}(\infty)$ is obtained by fitting $\overline{\Lambda}(R_i)$ to the two-parameter curve

$$\overline{\Lambda}(R) = \overline{\Lambda}(\infty) + C/R \tag{3.17}$$

where C is a second free parameter. Using an F-test and a comparison of residual sum of squares, we determined that the C/R subleading term is a better fit than (i) no subleading term ($C = 0$), (ii) a subleading term $C\log(R)/R$, and (iii) a subleading term C/R^2. Our definition of $\overline{\Lambda}(\infty)$ corresponds to $\overline{\Lambda}/(4\phi^{1/2})$ and $\phi^{1/2}B$ in [29] and to $\overline{\Lambda}/(4\phi^{1/2})$ and $\phi^{1/2}B_N$ in [30].

As a test of our procedure, we evaluate $\overline{\Lambda}(\infty)$, varying the upper integration limit $R_{\max}$, for different crystal point patterns: kagome, honeycomb, square, and triangle lattices. The lattice spacings have been chosen so that the number of points per unit area is one. For each crystal point pattern, the window centers are chosen to be uniformly distributed within the unit cell. These estimates are shown in Figure 3.6, with the ideal values computed in [29] and [30] overlaid in dashed lines. Our procedure approaches an accuracy that is within 0.1% of the ideal values for $R_{\max} \gtrsim 27$ for the triangle and square lattices and $R_{\max} \gtrsim 35$ for the honeycomb and kagome crystals.

We perform a similar test with the quasicrystal point patterns. In Figure 3.7, we show, for three representative LI classes, our estimates of $\overline{\Lambda}(\infty)$ as the upper integration limit $R_{\max}$ is varied. Comparing with $\overline{\Lambda}(\infty)$ evaluated at $R_{\max} = 400$ (dashed lines), the percentage difference is less than 0.1% for $R_{\max} \gtrsim 100$ for the $\gamma = 0$ class and $R_{\max} \gtrsim 150$ for $\gamma = 0.2$ and $\gamma = 0.5$. We also tested how $\overline{\Lambda}(\infty)$ varies with the number of windows M and found that, comparing with $M = 10000$, the percentage difference is less than 0.1% for $M \gtrsim 3500$.

For the estimates of $\overline{\Lambda}(\infty)$ presented in this Chapter, we used the conservative choices of $R_{\max} = 400$ and $M = 10000$. Moreover, the sampling of LI classes γ must

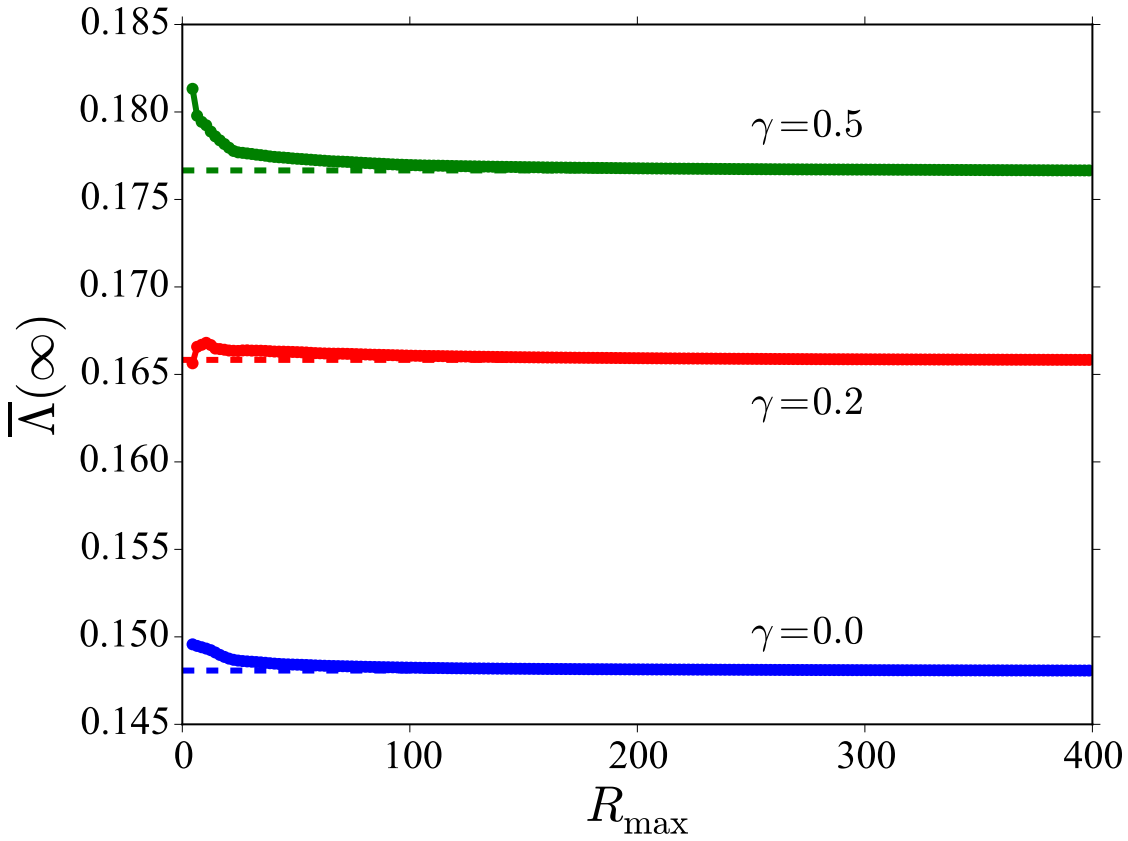

Figure 3.7: **Convergence test of $\overline{\Lambda}(\infty)$ for quasicrystal point patterns.** Estimates of the degree of hyperuniformity $\overline{\Lambda}(\infty)$, as the upper integration limit $R_{\max}$ is varied, for three quasicrystal point patterns. Portions of the corresponding tilings are shown in Figure 3.1. Estimates of $\overline{\Lambda}(\infty)$ evaluated at $R_{\max} = 400$ are overlaid in dashed lines.

be treated with care, because random sampling would miss features that occur at the discrete set of points $\gamma = n\tau$. We do a uniform sampling from 0 to 0.5 in intervals of 0.005, in addition to sampling $n\tau$ for n from 1 to 15. The values of γ are mapped to equivalent values lying within the interval [0,0.5] using Eq. (3.13).

3.5 Results and Discussion

Our calculation of $\overline{\Lambda}(\infty)$ *versus* γ for pentagonal DPTs is shown in Figure 3.8. There are noteworthy features in $\overline{\Lambda}(\infty)$, as a function of γ, that may not have been expected. The function appears to be continuous and increases on average. It also appears to

have a global minimum at the Penrose LI class ($\gamma = 0$), a global maximum at $\gamma = 0.5$, and local minima at the restorable LI classes ($\gamma = n\tau$). The local minima are cusplike, not smooth. Moreover, the depths of these local minima appear to decrease with respect to n. In Figure 3.8, we have included a magnified portion of the curve around $\gamma = \tau$, where a finer resolution sampling of γ was performed.

As shown in the upper panel of Figure 3.9, the increasing trend of $\overline{\Lambda}(\infty)$ with γ is already exhibited by $R_{\max} = 2$. This indicates that the trend must be attributable to local geometrical features on length scales of order ≤ 2, given that this estimate of $\overline{\Lambda}(\infty)$ was obtained from information contained in sampling windows with radius ≤ 2. As shown in the lower panel, by $R_{\max} = 16$, the cusp at $n = 1$ begins to appear, with more cusps appearing as $R_{\max}$ increases.

To explore the dependence of $\overline{\Lambda}(\infty)$ on the local geometry of the DPTs, we construct their Voronoi tesselations, considering the vertices as a point pattern. The *Voronoi cell* of a vertex is the region of space within which all points in space are closer to that vertex than to any other. Each of the sixteen vertex environments in Figure 3.4 has a corresponding Voronoi cell (shown in Figure 3.4 as dashed, red lines), with an area that we denote by A_i ($i = 1, \ldots, 16$). The tesselation of space by the Voronoi cells is the *Voronoi tesselation*. The distribution of Voronoi cell areas in the Voronoi tesselation quantifies the local geometric structure of the point pattern.

We compute the standard deviation σ_V of the Voronoi cell areas as follows:

$$\sigma_V \equiv \sqrt{\sum_{i=1}^{16} F_i \left(A_i - \mu_V\right)^2} \,, \tag{3.18}$$

where we have used the frequencies F_i of the vertex environments from Figure 3.5, and $\mu_V \equiv \sum_{i=1}^{16} F_i A_i$ is the average Voronoi cell area. The normalized standard deviation σ_V/μ_V of the areas is shown in Figure 3.10 as a function of γ. We observe that the

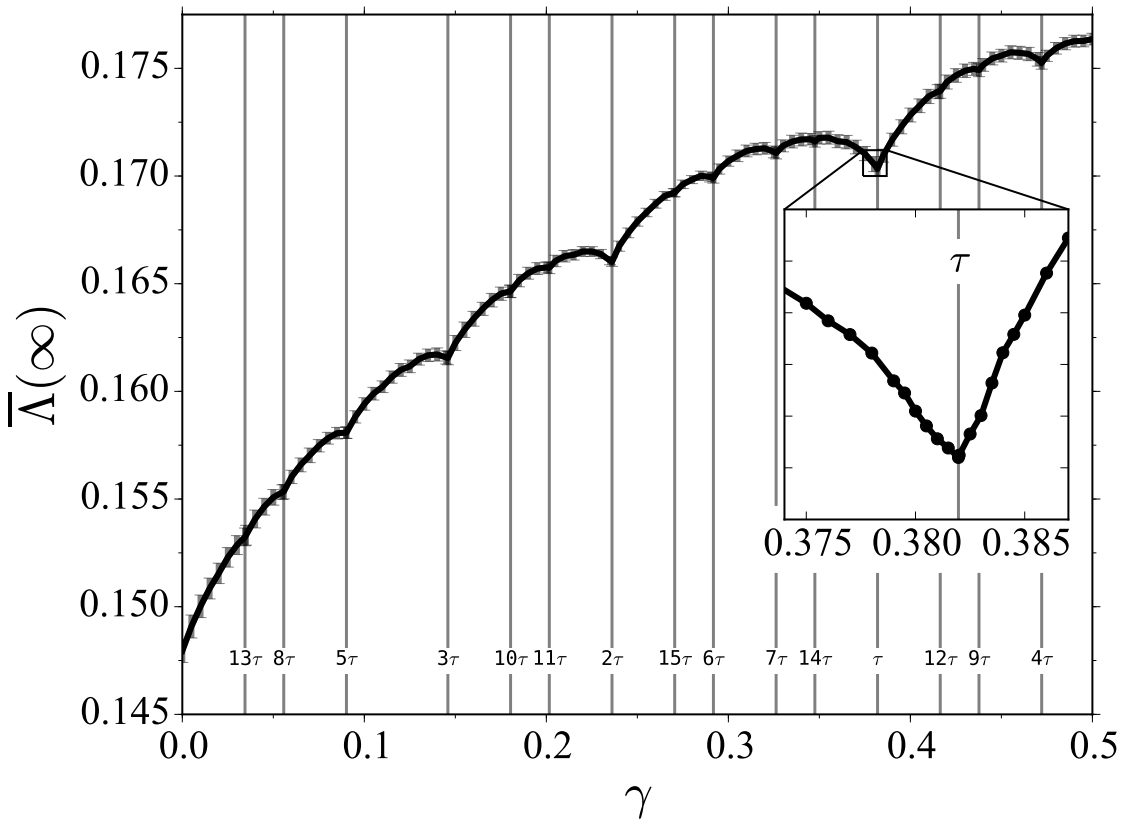

Figure 3.8: **Degree of hyperuniformity** $\overline{\Lambda}(\infty)$ *versus* **LI class** γ**.** The vertical lines mark the restorable LI classes $\gamma = \tau, 2\tau, \ldots, 15\tau$, mapped to equivalent values lying within the interval [0,0.5] using Eq. (3.13). Magnified portion around $\gamma = \tau$ shows the typical structure of the local minima. Each point represents an average over ten tilings from the same LI class γ. The error bars represent the standard deviation of the estimates of $\overline{\Lambda}(\infty)$. Pentagrids contain 800 grid lines per grid; each tiling contains approximately 3.5×10^6 vertices; upper integration limit $R_{\max} = 400$ and number of windows $M = 10000$.

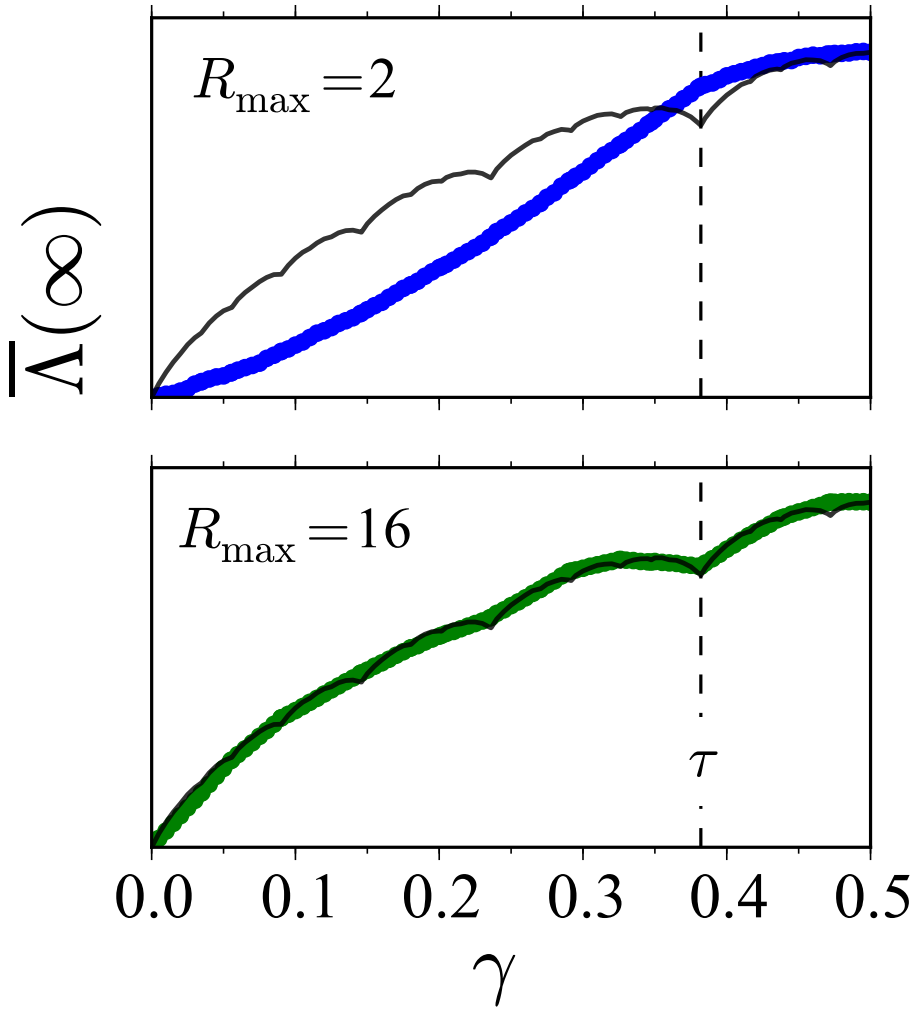

Figure 3.9: **Degree of hyperuniformity $\overline{\Lambda}(\infty)$ evaluated at $R_{\max} = 2$ and 16.** Values at $R_{\max} = 2$ (blue, upper panel) and 16 (green, lower panel) are overlaid on the curve from Figure 3.8, which was evaluated at $R_{\max} = 400$. The curves have been rescaled so that $\overline{\Lambda}(\infty)$ at $\gamma = 0$ and at $\gamma = 0.5$ are set to 0 and 1, respectively. The dashed vertical line at $\gamma \approx 0.382$ marks the $\gamma = \tau$ class.

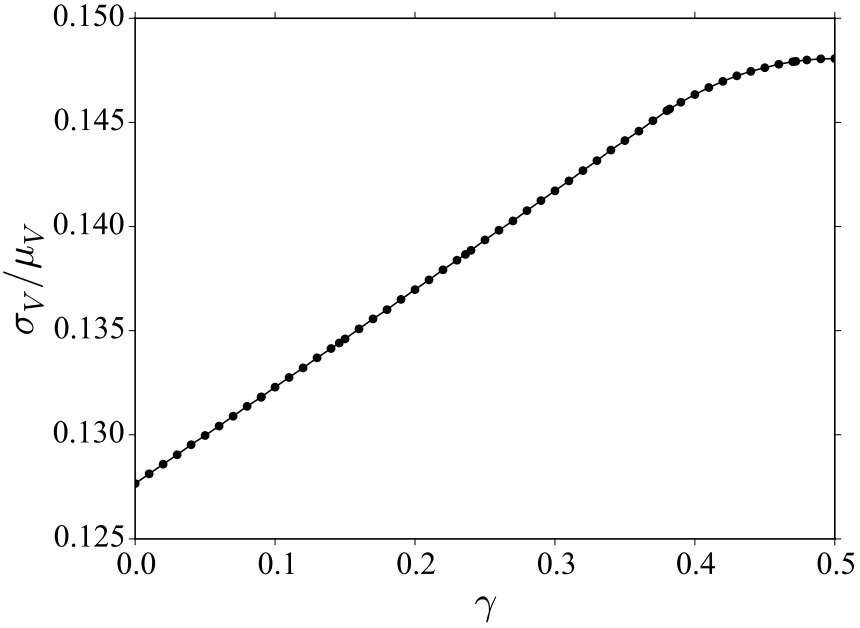

Figure 3.10: **Normalized standard deviation σ_V/μ_V of the Voronoi cell areas *versus* LI class γ.**

distribution of vertex environments, as characterized by σ_V/μ_V, is monotonic with γ and increases with γ in a manner similar to $\overline{\Lambda}(\infty)$ in Figure 3.8, excluding the cusps.

We therefore see two competing effects: the local ordering (e.g., as measured by σ_V/μ_V) and the restorability (e.g., as measured by the restorability radius R_r). The restorability radius is a characteristic length scale of the restorable LI classes. It is smallest for the Penrose LI class, which has the highest degree of hyperuniformity, so one might have expected $\overline{\Lambda}(\infty)$ to grow monotonically with R_r. Instead, we claim that the leading effect is the local ordering, which is monotonic with γ. The deviations from monotonicity with γ (i.e., the depths of the cusps) are a subdominant effect that is monotonic with the restorability radius. The evidence that the local ordering is the dominant factor in determining the degree of hyperuniformity is that the value of $\overline{\Lambda}(\infty)$ is not monotonic in R_r, but, instead, is more correlated with γ.

As noted in the Introduction, it had been an open question whether the degree of hyperuniformity varies with LI class. The results above clearly show the answer is yes.

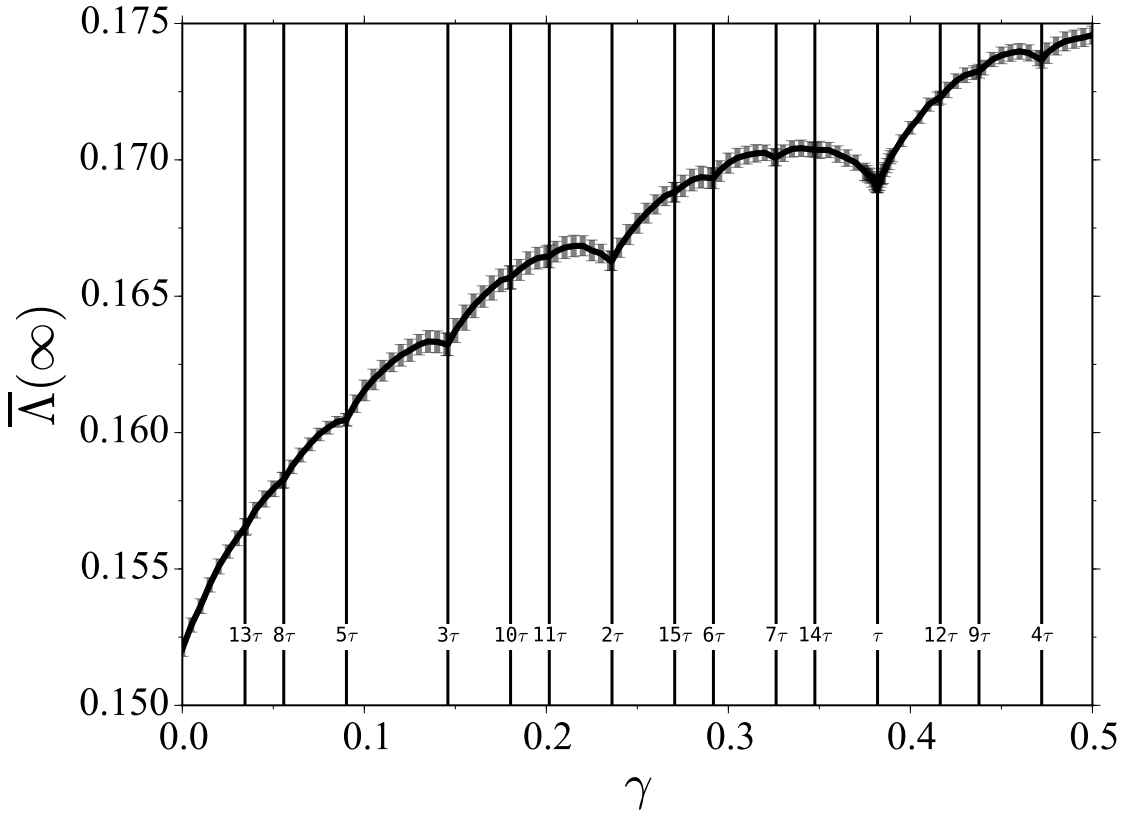

Figure 3.11: **Degree of hyperuniformity $\overline{\Lambda}(\infty)$ *versus* LI class γ of quasicrystalline point patterns obtained by placing points at tile centers.** The curve is virtually identically to the one obtained by placing points at vertices (Fig. 3.8). (Same parameters were used here as those used for the curve in Fig. 3.8.)

Evidently, the repeating units and the symmetry do not, by themselves, determine the degree of hyperuniformity—the continuum of DPTs studied here are constructed from the same tiles and have the same five-fold symmetry (with the exceptions of $\gamma = 0$ and $\gamma = 0.5$, which have ten-fold symmetry, although the tilings corresponding to these two special choices of γ also have different values of $\overline{\Lambda}(\infty)$). The results also show, for the DPTs studied here, that the differences in hyperuniformity are largely attributable to local differences in point (or tile) configurations and that restorability plays a factor. We have also studied point patterns obtained by placing points at the centers of the tiles instead of at the vertices, shown in Fig. 3.11. Comparing with Fig. 3.8, the results are virtually identical.

A primary question of interest is whether the differing degree of hyperuniformity among LI classes has any physical consequence, such as on electronic and photonic transport properties. In the next Chapter, we will report on the photonic properties of the set of LI classes studied here.

3.6 Appendix: Implementation of the dual method

We solve for the points of intersection between gridlines and present a solution in vector form, which lends itself to faster computational evaluation than solutions in component form. We use the fact that a straight line in $\mathbb{R}^2$ can be written in terms of a vector $\mathbf{v} = (v_x, v_y)$ parallel to the line and a point (x_0, y_0) lying on the line as follows:

$$y - y_0 = \tfrac{v_y}{v_x}(x - x_0) \ . \tag{3.19}$$

We start with a periodic pentagrid. Each of the five grids contains $2N+1$ equally spaced gridlines (we take the spacing to be one), oriented normal to one of the unit star vectors

$$\mathbf{r}_i = (\cos 2\pi i/5, \sin 2\pi i/5) \ , \ i = 1, 2, \ldots, 5 \ . \tag{3.20}$$

Every gridline has an index $\mu \in \{-N, -N+1, \ldots, N-1, N\}$ corresponding to its ordinal position in the grid. The gridline with index 0 is displaced from the origin by a phase $\gamma_i \in [0, 1]$. The gridline with index μ from grid i is denoted by g_i^μ.

We now write an equation for a gridline g_i^μ in the form of Eq. (3.19). Because g_i^μ is normal to the star vector $\mathbf{r}_i = (r_{ix}, r_{iy})$, a vector that is parallel to g_i^μ is

$$\mathbf{v} = \mathbf{r}_i^\perp = (-r_{iy}, r_{ix}) \ . \tag{3.21}$$

A point on g_i^μ is

$$(x_0, y_0) = \mathbf{r}_i \, (\mu - \gamma_i) = \alpha_i^\mu (r_{ix}, r_{iy}) \ , \tag{3.22}$$

where $\alpha_i^\mu \equiv \mu - \gamma_i$. Therefore, following Eq. (3.19), we can write the equation for g_i^μ as

$$y - \alpha_i^\mu r_{iy} = -\tfrac{r_{ix}}{r_{iy}}(x - \alpha_i^\mu r_{ix}) \ , \tag{3.23}$$

which can be simplified as follows, because the star vectors are of unit length:

$$y = \frac{\alpha_i^\mu - x r_{ix}}{r_{iy}} \ . \tag{3.24}$$

We can straightforwardly solve for the point of intersection $\mathbf{X}$ between two grid-lines g_i^μ, g_j^ν, where $i \neq j$:

$$\mathbf{X} = \frac{1}{\mathbf{r}_i \cdot \mathbf{r}_j^\perp}\Big(\alpha_j^\nu r_{iy} - \alpha_i^\mu r_{jy}, \alpha_i^\mu r_{jx} - \alpha_j^\nu r_{ix}\Big) \ , \tag{3.25}$$

which can be written in vector form (the key result of this Appendix):

$$\mathbf{X} = \frac{\alpha_i^\mu \mathbf{r}_j^\perp - \alpha_j^\nu \mathbf{r}_i^\perp}{\mathbf{r}_i \cdot \mathbf{r}_j^\perp} \ . \tag{3.26}$$

The kth grid index K_k is obtained as

$$K_k = \lceil \mathbf{X} \cdot \mathbf{r}_k + \gamma_k \rceil \ , \tag{3.27}$$

where $\lceil \cdot \rceil$ is the greatest integer function. The tile (i.e. set of four vertices) corresponding to $\mathbf{X}$ can then be obtained

$$\{\mathbf{t}, \mathbf{t} + \mathbf{r}_i, \mathbf{t} + \mathbf{r}_i + \mathbf{r}_j, \mathbf{t} + \mathbf{r}_j\} \tag{3.28}$$

where $\mathbf{t} = \sum_{i=1}^{5} K_i \mathbf{r}_i$.

Chapter 4

Light localization in local isomorphism classes of quasicrystals

In this Chapter, we report on the photonic properties of the same continuum of pentagonal quasicrystal tilings studied in Chapter 3.

4.1 Introduction

The results described herein represent the first systematic investigation of how a continuous set of LI classes differ in their photonic properties. We examine dielectric heterostructures generated from the pentagonal quasicrystal tilings. We demonstrate that a generic feature of their photonic bandstructure is that it contains effectively localized states, lying inside the fundamental bandgap, with frequencies, frequency splittings, and degeneracies that are predictable and tunable. The predictability and tunability of these effectively localized states significantly improves one's ability to control the design of photonic quasicrystal heterostructures; existing methods for generating such states have relied on the introduction of defects into the structure.

The one LI class for which these states are absent is the Penrose tiling. Consequently, it has the largest bandgap.

We begin in Section 4.2 by describing how we generate periodic approximants of the ideal, infinite tilings so that Maxwell's equations can be exactly solved. In Section 4.3, the details are provided for how the dielectric heterostructures are derived from the tilings and how the bandstructure calculation is performed. Our main results are presented in Section 4.4. Concluding remarks are provided in Section 4.5.

4.2 Periodic approximants

The approximants are generated using the dual method described in Section 3.3.1 with one modification: instead of $\mathbf{r}_i = (\cos 2\pi i/5, \sin 2\pi i/5)$, the star vectors are chosen as follows:

$$\begin{aligned}
&\hat{\mathbf{r}}_0 = (1,0)\ ,\ \hat{\mathbf{r}}_1 = (\cos 2\pi/5, \sin 2\pi/5)\ ,\\
&\hat{\mathbf{r}}_2(n) = (-1, \tau_n^{-1}) \cdot (\hat{\mathbf{r}}_0, \hat{\mathbf{r}}_1)\ ,\\
&\hat{\mathbf{r}}_3(n) = -(\tau_n^{-1}, \tau_n^{-1}) \cdot (\hat{\mathbf{r}}_0, \hat{\mathbf{r}}_1)\ ,\\
&\hat{\mathbf{r}}_4(n) = (\tau_n^{-1}, -1) \cdot (\hat{\mathbf{r}}_0, \hat{\mathbf{r}}_1)\ ,
\end{aligned}$$

where $\tau_n = F_{n+1}/F_n$ $(= 1/1, 2/1, 3/2, 5/3, \dots)$ and F_n is the nth Fibonacci number $(F_0 = F_1 = 1)$. Examples from different LI classes are shown in Fig. 4.1. For the Penrose LI class, this procedure minimizes the density of defects—necessary to make the tilings periodic—to two mismatched edges per unit cell [105]. As $n \to \infty$: the approximants approach the ideal tiling; the number of vertices in the unit cell increases; $\tau_n \to \tau = (1+\sqrt{5})/2 \approx 1.618$, the golden ratio; and $\hat{\mathbf{r}}_i(n) \to \mathbf{r}_i$, the star vectors of the ideal tiling.

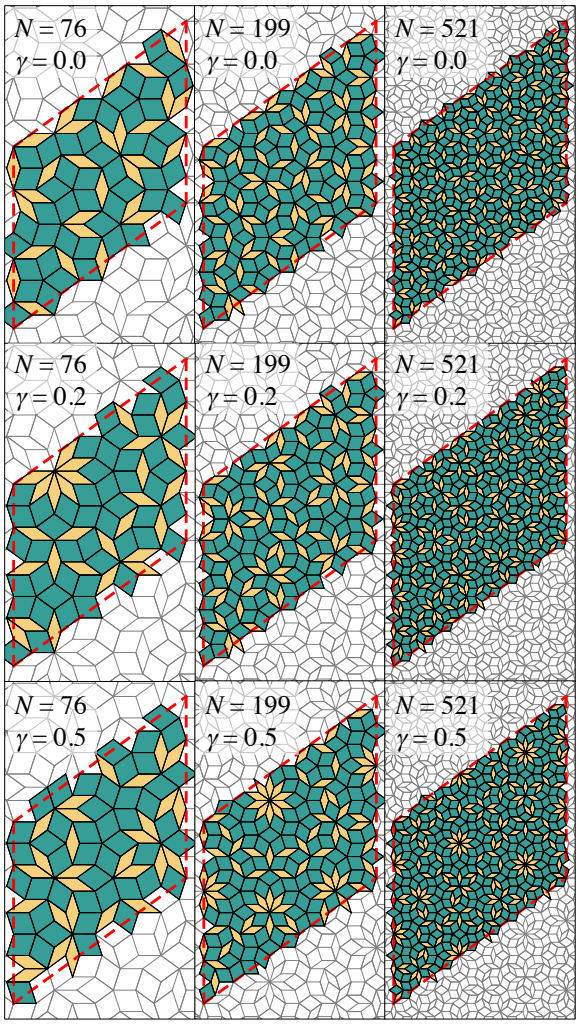

Figure 4.1: **Examples of periodic approximants from three LI classes (top to bottom) and from different degrees of approximant (left to right).** The LI classes are: $\gamma = 0$ (top row), $\gamma = 0.2$ (middle row), and $\gamma = 0.5$ (bottom row). The number of points in the unit cell for each approximant is: $N = 76$ (left column), $N = 199$ (middle column), and $N = 521$ (right column). The unit cell for each approximant is outlined in dashed red lines. The tiles that form the unit cell are filled in, with fat tiles filled in with green and skinny tiles filled in with yellow. (Some of the unit-cell tiles extend beyond the dashed red lines, because we have chosen here to completely fill in tiles (without repeats) that occur at the boundary of the unit cell, instead of truncating them.)

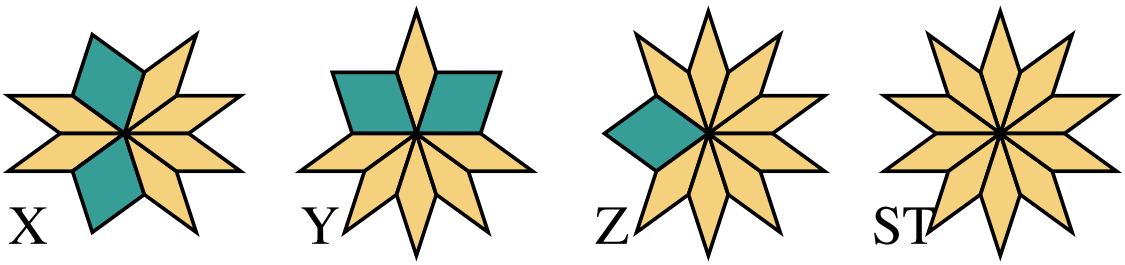

Figure 4.2: **The four special vertex environments.**

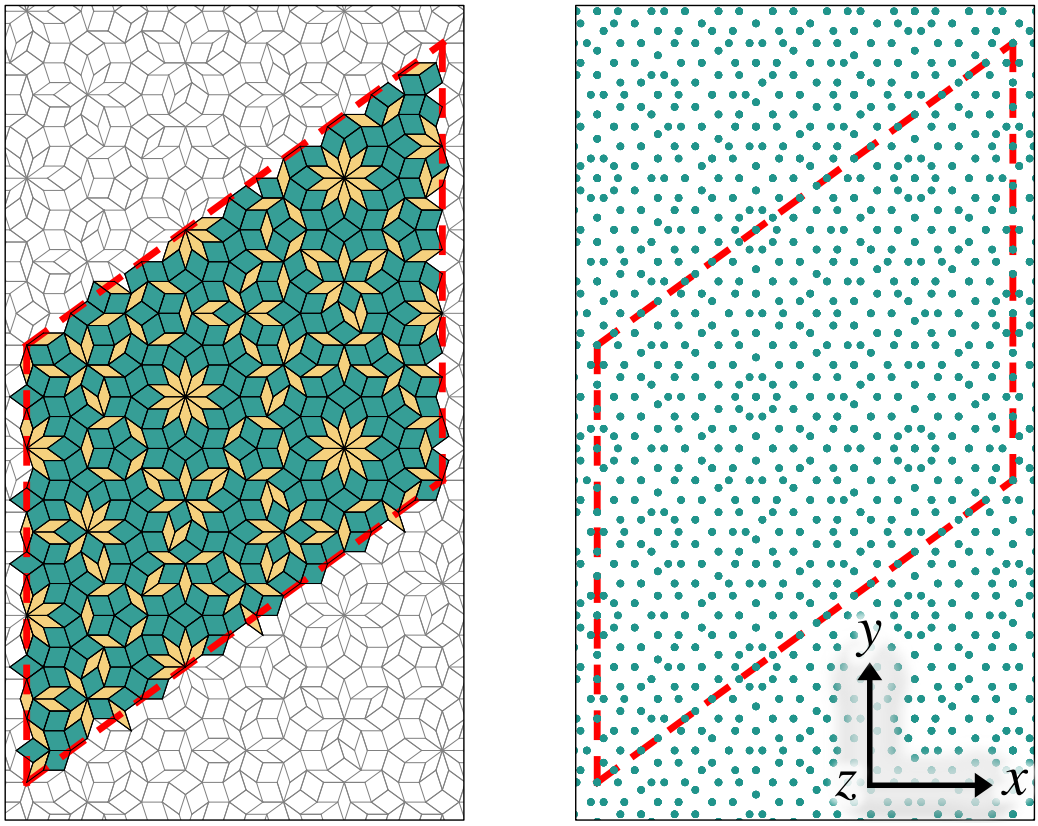

Figure 4.3: **Example of a dielectric structure (right panel) derived from the tiling shown in the left panel.** The unit cell is outlined in dashed red lines. Dielectric cylinders (filled in with green) have axes oriented along the z-axis, which points out of the page.

4.3 Photonic bandstructure calculation

We compute the photonic bandstructure of dielectric heterostructures constructed by placing, on the tile vertices and oriented normal to the tiling plane, an array of parallel, infinitely long cylindrical rods with dielectric constant 11.56 (silicon) and radius $0.18a$ (filling fraction ~12.5%) in a background of air. The same radius (equivalently, same filling fraction) is chosen for all structures to allow for fair comparison. An example of such a dielectric structure is shown in Fig. 4.3.

Maxwell's equations are solved for states with transverse magnetic (TM) polarization, i.e., with the electric field oriented parallel to the cylindrical axis (the z-axis in Fig. 4.3). Details can be found in Appendix 4.6. The TM bandstructure is calculated using a supercell approximation and the plane-wave expansion method [106, 107]. Spatial resolution of the unit cell is chosen to be 512×512 pixels. For $N = 521$ approximants, the frequencies computed at this resolution differ by less than 0.3% of those computed at 1024×1024 resolution. We compute the lowest $1.1 \times N$ bands, which reliably contains the first sizeable bandgap.

For quasicrystals, the photonic bandgaps and the neighboring bands are known to be highly isotropic [32, 108]. Therefore, we simplify our analysis by restricting our computation of spectra to the $\mathbf{\Gamma} = (0, 0)$ and $\mathbf{M} = (\mathbf{b}, 0)$ symmetry points, where $\mathbf{b}$ is one of the basis vectors of the reciprocal lattice. These are defined for the hexagonal first Brillouin zone, corresponding to the rhombic unit cell of the approximant. (Because the basis vectors of the rhombic unit cell are not equal in magnitude, the hexagonal first Brillouin zone is flattened/stretched along one of the symmetry directions.)

4.4 Results

4.4.1 Effectively localized states

Whenever a SVE appears in a tiling, the TM bandstructure contains states in which the electric field is highly concentrated on the SVE, either on one isolated site or on many sites. Figure 4.4 shows representative examples of these states on isolated sites.

Take one of these states and let r be the radial distance from the central vertex. We observe that the energy density (the square of the field) peaks around $r \approx a$—where the first nearest neighbors are located—then decays to $\lesssim 1\%$ of the peak values by $r/a \approx 2$ and $\lesssim .01\%$ of the peak values by $r/a \approx 3$. There appears to be a log-linear decay, which is consistent with being localized on the SVE. However, because some states are observed to have support on multiple sites, they are not localized in the strict sense but, instead, may be multifractal, critical states [109, 110]. Determining whether this is the case is worthy of further investigation. Some initial studies are reported in Appendix 4.7. Here, we describe the states as *effectively localized*.

We note that similar states have been observed [111, 112] in a particular (unspecified) LI class, as well as in dodecagonal [113, 114] and octagonal [115] quasicrystal heterostructures. The states have been described as local resonances between closely neighboring scatterers that are arranged in highly symmetric configurations [111, 112, 115]. A review of these earlier studies can be found in [116].

4.4.2 Degeneracy of effectively localized states

The number of effectively localized states is directly related to the number of SVEs. We empirically observe that there is one state for every X vertex (Fig. 4.4a), one for every Y (Fig. 4.4b); two for every Z (Fig. 4.4c,d); and three for every ST (Fig. 4.4e,f; there are two orthogonal states that look like Fig. 4.4e). Thus, the total number of

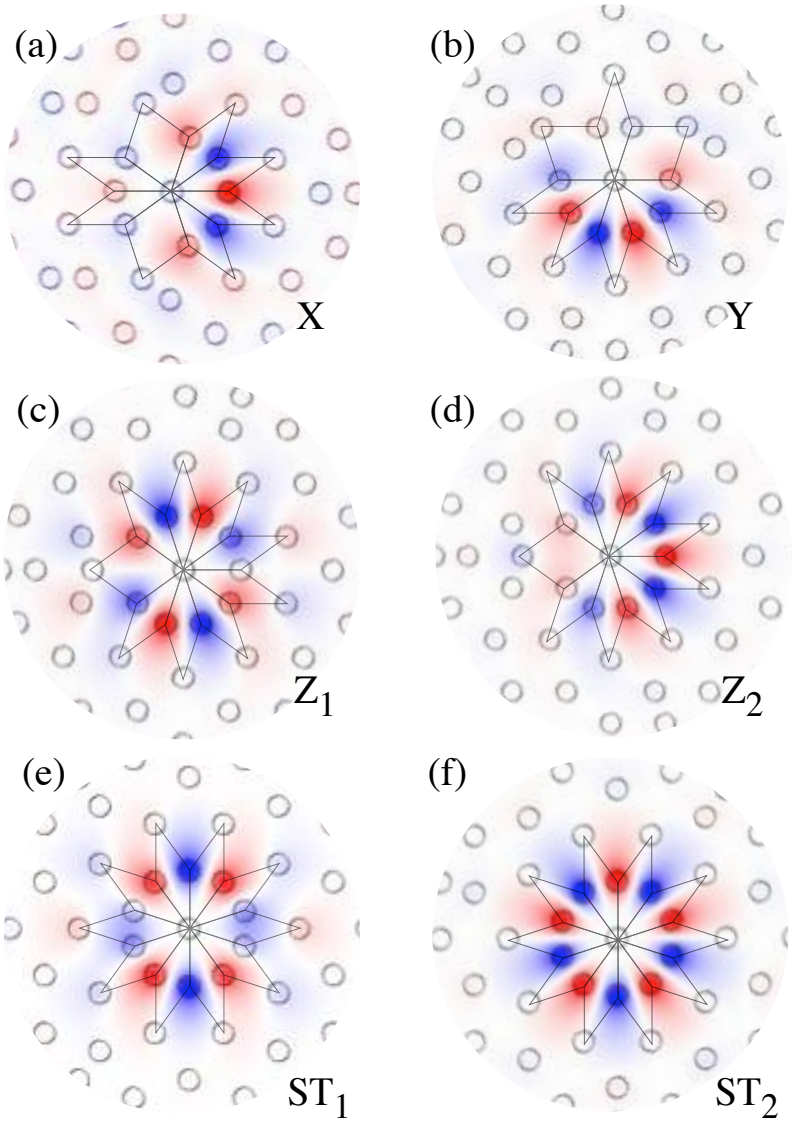

Figure 4.4: **Representative electric field distribution for the six observed types of effectively localized states.** Blue/red/white correspond to negative/positive/zero power for a given state. Contours of dielectric cylinders are shown, and the vertex environments are overlaid (see Fig. 4.2). (a) X, (b) Y, (c) Z_1, (d) Z_2, (e) ST_1, and (f) ST_2.

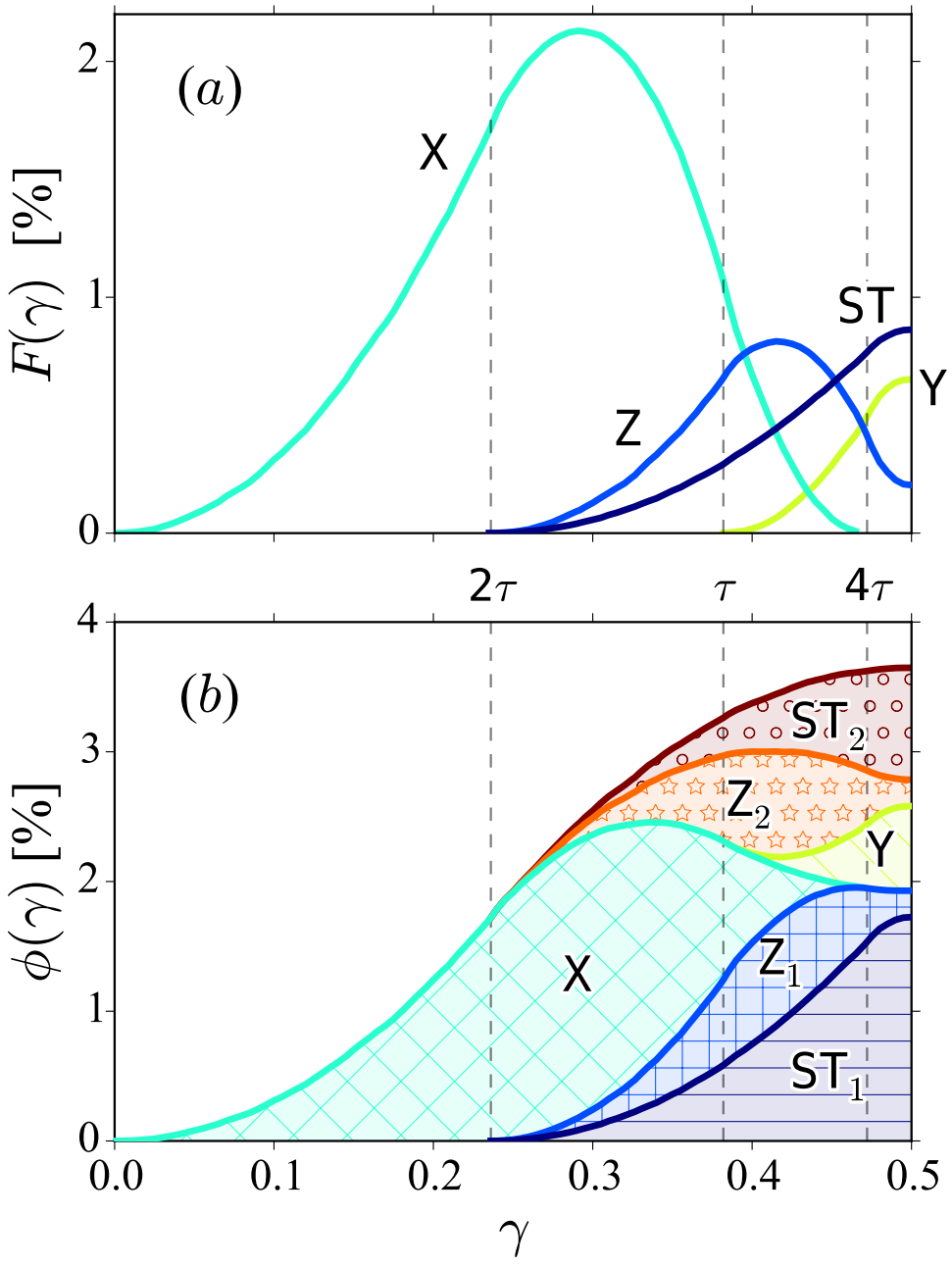

Figure 4.5: **Special vertex environments.** (a) Density F of the four special vertex environments (shown in Figure 4.2), *versus* LI class γ. (b) Expected fraction ϕ of special states (shown in Fig. 4.4) *versus* LI class γ.

effectively localized states $n_{\rm loc}$ is given by

$$n_{\rm loc} \equiv N_{\rm X} + N_{\rm Y} + 2N_{\rm Z} + 3N_{\rm ST} \ , \tag{4.1}$$

where $N_{\mathbf{V}}$ is the number of SVEs of type $\mathbf{V}$. For different renditions (i.e., choices of γ_i) from the same LI class, the number will differ.

In the infinite-system limit, the fraction of effectively localized states for LI class γ is given by

$$\phi(\gamma) = F_{\rm X}(\gamma) + F_{\rm Y}(\gamma) + 2F_{\rm Z}(\gamma) + 3F_{\rm ST}(\gamma) \ , \tag{4.2}$$

where $F_{\mathbf{V}}$ is the density of SVEs of type $\mathbf{V}$, shown in Fig. 4.5a. We plot $\phi(\gamma)$ in Fig. 4.5b. All of our numerical results thus far, which are summarized below, support the counting of effectively localized states according to Eqs. (4.1) and (4.2). The SVEs that are composed of a greater number of skinny tiles and which are more symmetric (i.e., Z and ST) have a larger number of states per SVE.

4.4.3 TM spectrum and characteristic frequencies of effectively localized states

Let ω_i^L, ω_i^H be the lower and upper frequencies of the ith band. It is useful to define, for a given tiling, the *upper band edge frequency* ω_+ and the *lower band edge frequency* ω_- as follows:

$$\omega_+ \equiv \omega_N^L \ , \quad \omega_- \equiv \omega_{N-n_{\rm loc}}^H \tag{4.3}$$

where N is the number of vertices in the unit cell. Figure 4.6 shows ω_+, ω_-, and their average, plotted for several samples from different LI classes γ, for different degrees of approximants. Several observations can be made:

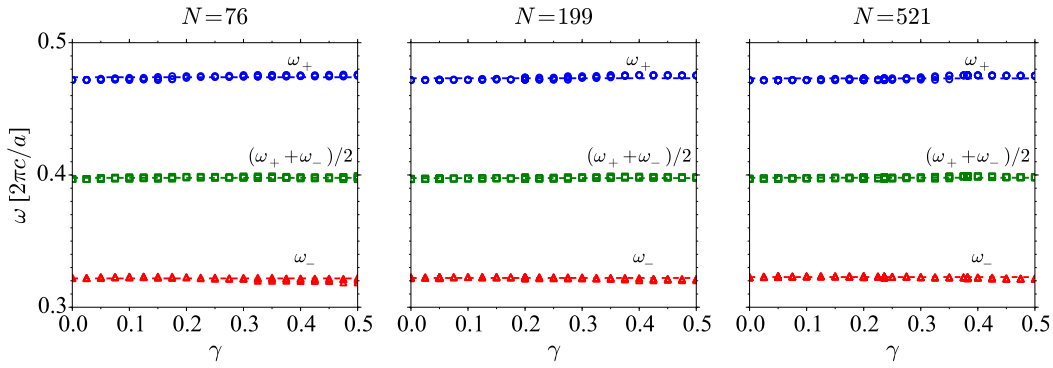

Figure 4.6: **Upper and lower band edge frequencies.** Upper band edge frequency $\omega_+ \equiv \omega_N^L$ (blue circles, top), lower band edge frequency $\omega_- \equiv \omega_{N-n_{\rm loc}}^H$ (red triangles, bottom), and the central frequency (green squares, middle), *versus* γ. As discussed in the text, ω_+ and ω_- correspond to the upper and lower edges, respectively, of the fundamental bandgap. Dashed lines represent the average value for a given curve. Each panel is a different degree of approximant, with increasing degree from left to right. Number of points in the unit cell is shown above each panel ($N = 76, 199, 521$).

First, none of these quantities changes significantly *versus* the degree of the approximant, characterized by N. This indicates that these quantities quickly converge to the values of the ideal, infinite system.

Second, the upper and lower band edges remain approximately constant versus γ. For the Penrose LI class, the region between ω_- and ω_+ is called the *fundamental bandgap*. Extending this definition to all LI classes, we find that the effectively localized states counted by Eq. (4.1) are high-frequency states lying within the fundamental bandgap.

Third, none of these quantities changes significantly *versus* LI class γ, even though the number of effectively localized states typically varies for different samples and for different values of γ. This indicates that we are correctly counting the number of states lying within the fundamental bandgap, which supports the counting conjecture in Eq. (4.1). This is also consistent with the states being localized.

Finally, the fraction of these states appears to stay constant, as the degree of the approximant increases. This is contrary to what we would expect if these effectively

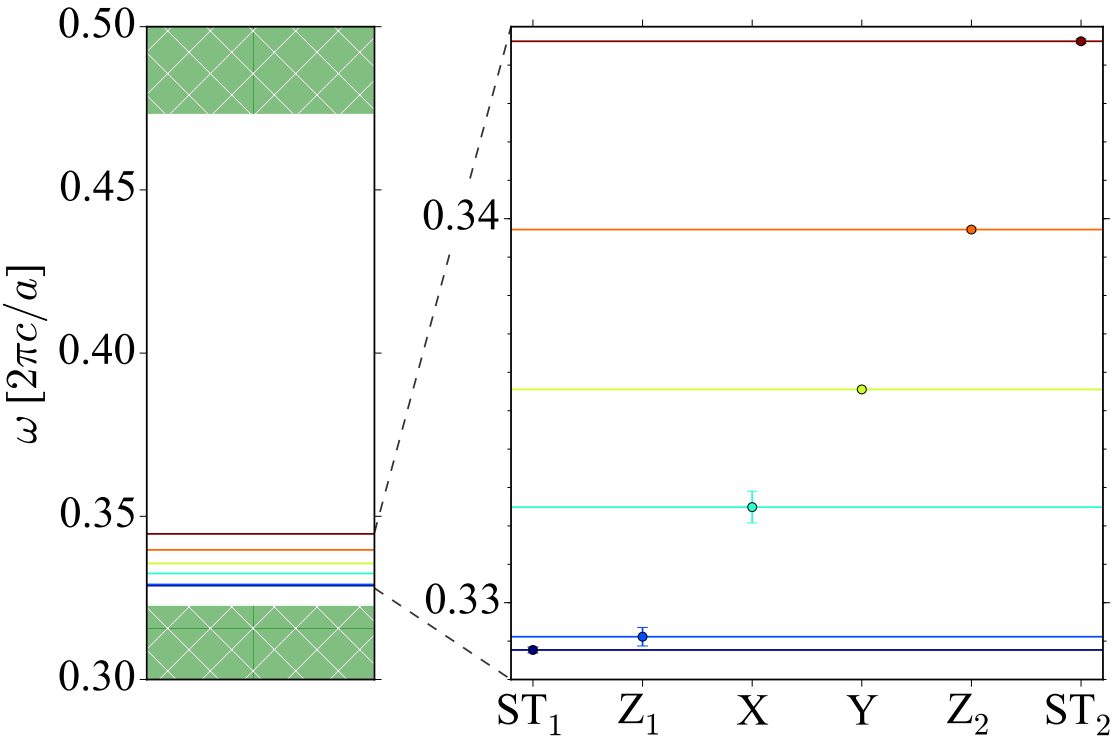

Figure 4.7: **The average frequencies of effectively localized states.** The states are shown in Fig. 4.4. In the left panel, the green, solid regions at the upper and lower ends represent the continuum of states adajcent to the fundamental bandgap. The right panel, which is a blown up portion of the left panel around the effectively localized states, identifies which effectively localized states correspond to the different frequencies.

localized states arose from defects. We thus conclude that these effectively localized states are not defects, but are, rather, robust states that arise due to the SVEs.

Figure 4.7 shows the averaged midband frequency for each type of state. Within uncertainties, all states of a given type have the same frequency, i.e., are degenerate. Moreover, frequencies for different types do not overlap. This indicates that each type of state has a characteristic frequency.

We also observe that the characteristic frequencies do not vary significantly *versus* γ, which suggests that these states are primarily attributable to the presence of SVEs and not to the global structure of the tiling. This supports a hypothesis, based on the study of one unspecified LI class [111, 112, 115], that these states can be described

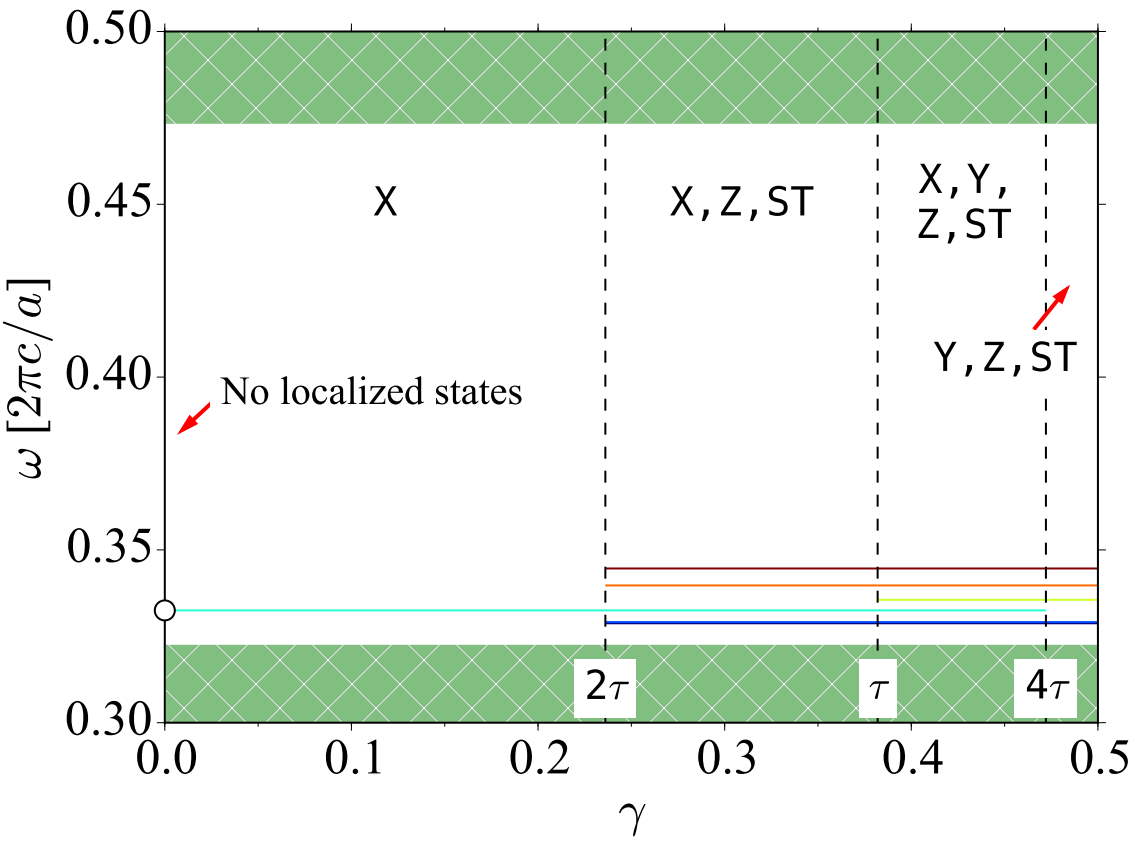

Figure 4.8: **Expected TM spectrum around the fundamental bandgap *versus* LI class γ.** Average frequencies of effectively localized states shown within each range of γ that their corresponding SVEs appear. Also labeled are the SVE types occurring within each range of γ. Green, solid regions at upper and lower ends represent the continuum of states adajcent to the bandgap. Note: $\gamma = 0$ (Penrose LI class) has no SVEs and no corresponding effectively localized states.

as local resonances between closely neighboring scatterers that are arranged in highly symmetric configurations. Further evidence is that the four SVEs have the largest numbers of adjacent skinny tiles (at least four); all other vertex environments contain fewer than four adjacent skinny tiles.

From these observations, we expect that the TM spectrum around the fundamental bandgap will vary with γ according to Fig. 4.8. We also expect the *outer bandgap*—which is the width of the gap between bands N and $N+1$, normalized by the midgap frequency—to vary with γ according to Fig. 4.9.

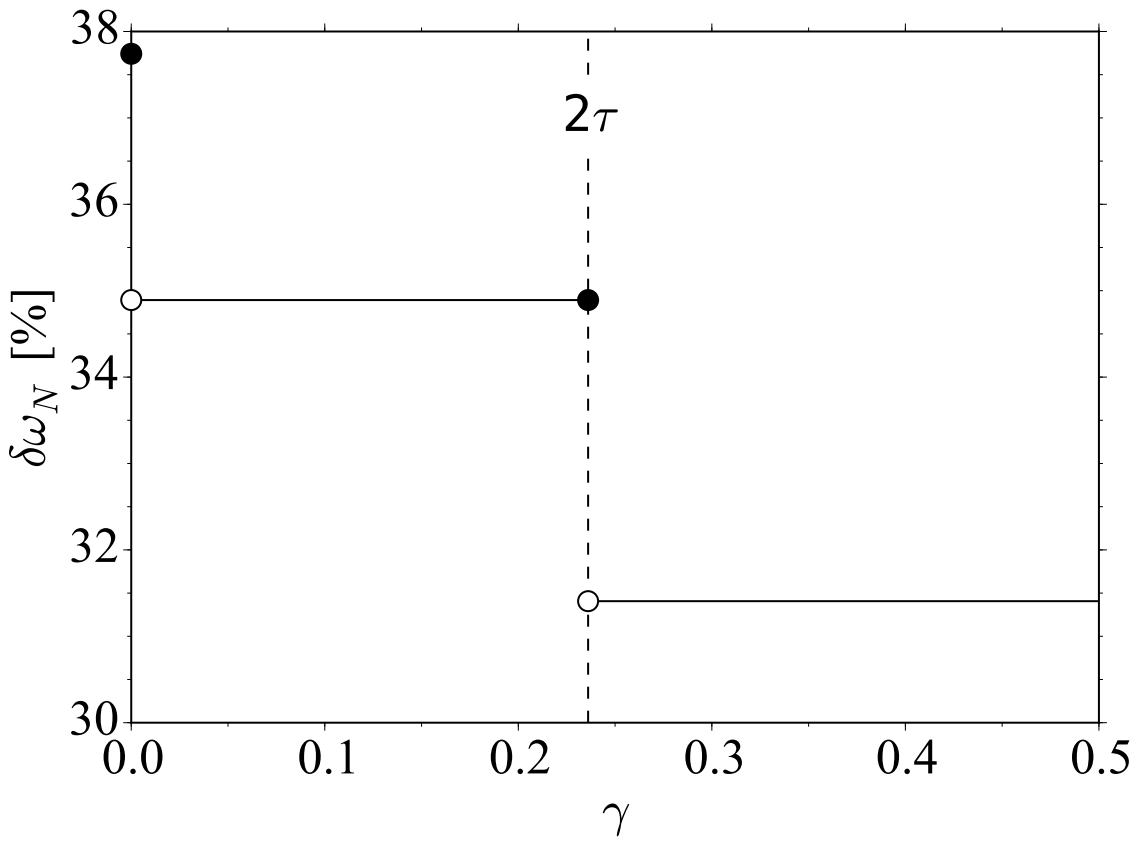

Figure 4.9: **Expected outer bandgap *versus* LI class γ.**

We thus discover that the Penrose LI class is exceptional for being the only class with no effectively localized TM states; as a consequence, it has the largest outer bandgap. All other LI classes have, generically, effectively localized TM states within the fundamental bandgap with predictable and tunable degeneracies (Fig. 4.5) and frequencies (Fig. 4.7) and are related to the presence of SVEs. In our initial studies using other choices of dielectric decoration, we have found qualitatively the same results, although we note that some choices of decoration also produce effectively localized states within the *air* component of the heterostructure (this is further described in Appendix 4.8).

4.5 Discussion

4.5.1 Order and disorder

We have presented the first systematic study of how the photonic bandstructure varies with the LI class for a continuum of photonic quasicrystals. Our results introduce a new form of control over the properties of localized states in photonic quasicrystal heterostructures (PQCs), which may find utility in the design of optical cavities for use as radiation sources [117] or sensors [118]. Existing methods for generating localized states have relied on *disorder* to produce localized states by intentionally introducing defects into the heterostructure, e.g., removing, adding, or changing the geometry of one or several scatterers. A disorder-based design procedure presents challenges, such as minimizing interference between defects and obtaining a desired set of frequencies. As shown in this Chapter, these design challenges are not present in the PQCs, where the effectively localized states are *not* defects. We have shown that the effectively localized states in PQCs are a consequence of the ordered structure of the underlying quasicrystal. We have further shown that the frequencies, frequency splittings, spatial configuration, and concentration of the effectively localized states can all be predicted and tuned *in advance*, by varying the LI class and/or other parameters, such as the dielectric contrast or the cylinder radius. It would be of interest to see whether similarly localized states are present in LI classes of icosahedral quasicrystals.

It would also be of interest to understand how robust the effectively localized states are to the introduction of disorder, which is of practical relevance during fabrication. It is possible that uncorrelated disorder causes the effectively localized states to couple to one another to form extended states, leading to enhanced transport. Disorder-enhanced transport in quasicrystals was discussed in [119]. A tight-binding nearest-neighbor model on a Penrose tiling was used to calculate how the conductance changes as phason disorder increases [119]. The disorder was introduced by allowing

random perturbations of the spacing between adjacent gridlines, which manifests in the tiling as local rearrangements of tiles. It was reported that at some values of the Fermi energy, the conductance decreases with the strength of the disorder (indicating localization of states), while at other values of the Fermi energy, the conductance increases (i.e., enhanced transport).

Disorder-enhanced transport was experimentally observed for light in a photonic quasicrystalline lattice [120], generated using optical induction following the methods described in [121]. The resulting lattice contains centers of local ten-fold symmetry, resembling the ST SVE. It was found that localized states lie near the pseudo-gap (where there is a sharp reduction in the density of states) that are centered on the ST-like sites. When disorder is introduced, these localized states couple to one another, which results in extended states. As the disorder strength increases, eventually diffusive transport is observed; upon further increasing, the behavior becomes localized once again.

4.5.2 Hyperuniformity and photonics

It was proposed in [32, 33] that the "width of the photonic bandgap" is correlated with the "degree of hyperuniformity". As discussed in Chapter 3, hyperuniformity is the suppression of long-wavelength density fluctuations relative to typical structurally disordered systems (e.g., glasses, amorphous solids) [29]. Thus, a measure of the "degree of hyperuniformity" would also be a measure of long-range order. The proposed relationship between the photonic bandgap and hyperuniformity is based on the intuition that more long-range order leads to more interference, which leads to larger bandgaps (the origin of photonic bandgaps can be traced to interference due to Mie scattering and Bragg scattering [122, 123, 124]). Here, we briefly review how two measures of hyperuniformity are currently understood to be related to the photonic bandgap, informed by our results in this and the previous Chapter.

We begin by clarifying the term "photonic bandgap", which can take on many definitions—not all equivalent—depending on context. Any finite range of frequencies over which the density of states vanishes can be called a *photonic bandgap*. A photonic bandstructure can contain many photonic bandgaps, all of varying widths, where the *width* is defined as the difference between the upper band edge frequency and the lower band edge frequency, normalized by the midgap frequency. Therefore, further qualification is needed to know which photonic bandgap (of the possibly many that exist in a given bandstructure) is being referred to. Usually, the bandgap of interest is the one separating the air states (i.e., states in which the field is concentrated in the air component) from the dielectric states (i.e., states in which the field is concentrated in the dielectric component). When many such bandgaps exist, the one of interest is typically the bandgap with the lowest midgap frequency.

In this Chapter, we have introduced the notions of the *fundamental bandgap* and the *outer bandgap*. The *fundamental bandgap* refers to the bandgap that lies between bands $N-n_{\text{loc}}$ and $N+1$, where N is the number of scatterers in the unit cell and n_{loc} is the number of effectively localized states as defined in Eq. (4.1). When $n_{\text{loc}} \neq 0$, there are effectively localized states lying within the fundamental bandgap. Hence, the fundamental bandgap is not a photonic bandgap per se, but, instead, represents what the photonic bandgap would be in the absence of effectively localized states. The *outer bandgap* refers to the bandgap that lies between bands N and $N+1$. When $n_{\text{loc}} = 0$ and when there are no air states (described in Appendix 4.8), the fundamental bandgap and outer bandgap coincide.

When a dielectric structure is effectively two-dimensional (i.e., homogeneous along one direction, say, z), the eigenstates can be divided into two polarizations. This Chapter has studied only TM (transverse magnetic) states, in which the electric field is parallel to the z axis. There are also TE (transverse electric) states, in which the magnetic field is parallel to the z axis. Photonic bandgaps that exist in a spectrum

restricted to only TM (TE) polarized states are called TM (TE) bandgaps. A *complete* bandgap is a bandgap for both polarizations.

We now turn to one measure of the "degree of hyperuniformity", which is called the *degree of stealthiness* and applies only to *stealthy* hyperuniform point patterns [33, 125, 126]. Our discussion focuses on *stealthy disordered* point patterns, a subclass of disordered hyperuniform point patterns (i.e., neither crystalline nor quasicrystalline). Stealthy disordered point patterns have an isotropic, continuous structure factor $S(k)$. For stealthy disordered point patterns, the *degree of stealthiness* can be defined to be the largest wavenumber $k_C \geq 0$ such that $S(k) = 0$ for all $|k| < k_C$. Alternatively, the degree of stealthiness is the fraction χ of the first Brillouin zone over which $S(k) = 0$. Among two-dimensional stealthy disordered point patterns, all numerical evidence to date indicates that the degree of stealthiness (both k_C and χ) of a point pattern is correlated with the TM, TE, and complete bandgap of a dielectric decoration of the pattern [33].

A second measure of the "degree of hyperuniformity" is the leading coefficient in the local number variance (denoted here by $\overline{\Lambda}(\infty)$), which was described and computed in Chapter 3 for the pentagonal quasicrystal tilings (see Fig. 3.8). The measure $\overline{\Lambda}(\infty)$ can be defined for the subclass of two-dimensional hyperuniform point patterns in which the local number variance scales with the perimeter in the large-R limit, i.e., $\sigma^2(R) \sim R$ as $R \to \infty$ (see Eq. (3.1)). In two dimensions, all crystalline point patterns and all stealthy disordered patterns fall in this subclass [29, 30, 126], and numerical evidence strongly indicates that many quasicrystalline point patterns do as well, including those derived from the pentagonal quasicrystal tilings (see Chapter 3). For entropically favored stealthy disordered patterns in the canonical ensemble, $\overline{\Lambda}(\infty)$ is equivalent to the degree of stealthiness, in the sense that the two measures can be mapped one-to-one, and when χ (or k_C) increases, $\overline{\Lambda}(\infty)$ decreases [126, 127].

The results of this Chapter show that the *fundamental* TM bandgap for the pentagonal quasicrystal tilings appears to stay constant versus LI class γ (Fig. 4.8), whereas the *outer* TM bandgap decreases in discrete steps (Fig. 4.9), which is attributable to the appearance of special vertex environments at particular values of γ. Thus, comparing to how $\overline{\Lambda}(\infty)$ varies with LI class (as shown in Fig. 3.8), we find that neither the fundamental TM bandgap nor the outer TM bandgap displays a clear correlation with $\overline{\Lambda}(\infty)$. The results suggest that, among quasicrystals, $\overline{\Lambda}(\infty)$ is not correlated with the TM bandgap or complete bandgap.

4.6 Appendix: Computing the photonic bandstructure

We review the approximations used when solving Maxwell's equations to determine the photonic bandstructure of a dielectric medium. The numerical calculations employ a freely available software package [107] that implements a block-iterative plane-wave solver. A more complete review can be found in [106].

In the absence of any free charges or currents, Maxwell's equations are given by

$$\begin{aligned} \nabla \cdot \mathbf{E} = 0 \quad &, \quad \nabla \cdot \mathbf{D} = 0 \\ \nabla \times \mathbf{E} + \frac{\partial \mathbf{B}}{\partial t} = 0 \quad &, \quad \nabla \times \mathbf{H} - \frac{\partial \mathbf{D}}{\partial t} = 0 \ , \end{aligned} \tag{4.4}$$

where $\mathbf{E}$ is the electric field, $\mathbf{B}$ the magnetic field, and $\mathbf{D}, \mathbf{H}$ are auxiliary fields whose components are related to $\mathbf{E}$ and $\mathbf{B}$ (respectively) by a power series. For example, the components of $\mathbf{D}$ can be written in terms of the components of the electric field as

$$D_i = \sum_j a_{ij} E_j + \sum_{jk} b_{ijk} E_j E_k + \sum_{jkl} c_{ijkl} E_j E_k E_l + \ldots \tag{4.5}$$

where $a_{ij}, b_{ijk}, c_{ijkl}, \ldots$ are material parameters that depend on the dielectric medium. The fields are functions of position $\mathbf{r}$ and time t.

A few realistic approximations can be made that simplify the analysis: First, we take the strengths of the fields to be sufficiently small so that the auxiliary fields are linearly related to $\mathbf{E}$ and $\mathbf{B}$, i.e., Eq. (4.5) is truncated at first order. In this case, the components of the fields are related as follows:

$$D_i = \epsilon_0 \sum_{j=1}^{3} \epsilon_{ij} E_j \quad , \quad B_i = \mu_0 \sum_{j=1}^{3} \mu_{ij} H_j \ , \tag{4.6}$$

where ϵ_0 is the vacuum permittivity, μ_0 is the vacuum permeability, and ϵ_{ij}, μ_{ij} are a set of coefficients relating the auxiliary fields to the electric and magnetic fields.

Second, we approximate the dielectric materials as isotropic, which simplifies Eq. (4.6):

$$\mathbf{D}(\mathbf{r}) = \epsilon_0 \epsilon(\mathbf{r}) \mathbf{E}(\mathbf{r}) \quad , \quad \mathbf{B} = \mu_0 \mu(\mathbf{r}) \mathbf{H}(\mathbf{r}) \ , \tag{4.7}$$

where $\epsilon(\mathbf{r})$ and $\mu(\mathbf{r})$ are the relative permittivity and permeability, respectively.

Finally, we restrict our analysis to materials that are not dispersive (ϵ, μ do not depend on frequency), do not absorb the field (real ϵ, μ), are transparent to the field (positive ϵ, μ), and for which $\mu(\mathbf{r}) \approx 1$.

Considering the fixed-frequency Fourier components of the fields

$$\mathbf{E}(\mathbf{r}, t) = \mathbf{E}(\mathbf{r}) e^{-i\omega t} \quad , \quad \mathbf{B}(\mathbf{r}, t) = \mathbf{B}(\mathbf{r}) e^{-i\omega t} \ , \tag{4.8}$$

the above approximations allow us to recast Eqs. (4.4) as an eigenvalue problem for the spatial part of the fields:

$$\nabla \times \left(\epsilon^{-1}(\mathbf{r}) \nabla \times \mathbf{H}(\mathbf{r}) \right) = (\omega/c)^2 \, \mathbf{H}(\mathbf{r}) \ , \tag{4.9}$$

and $\mathbf{E}$ can be obtained from $\mathbf{H}$ via

$$\omega \mathbf{E}(\mathbf{r}) = \frac{i}{\epsilon_0 \epsilon(\mathbf{r})} \nabla \times \mathbf{H}(\mathbf{r}) \tag{4.10}$$

Given a dielectric medium, as characterized by $\epsilon(\mathbf{r})$, Eqs. (4.9) and (4.10) are solved to obtain the frequency eigenstates, which are the electromagnetic waves that can propagate through the medium with a definite frequency.

The dielectric structures studied in this Chapter are obtained from two-dimensional point patterns by decorating the points with infinitely long cylinders that are oriented out of the plane. The structures are uniform in the direction normal to the plane, which we call the z direction. Because of this symmetry, the eigenstates have zero momentum along z. They can be separated into two distinct sets of polarizations: (i) states in which $\mathbf{H}$ is parallel to z (*transverse electric* (TE) states); and (ii) states in which $\mathbf{E}$ is parallel to z (*transverse magnetic* (TM) states). Here, we study only the TM spectrum.

4.7 Appendix: Effectively localized states: localized *versus* extended

This Appendix reports on two studies that explore to what extent the effectively localized states are truly extended or localized. The studies presented here do not lead to definitive conclusions, but are intended to inform and guide how further studies might be performed. A couple notes on terminology: Because only effectively localized states are discussed here, we drop the "effectively localized" descriptor. Moreover, all states of a given type (e.g., ST_1 type, Z_1 type) are said to form a *miniband*.

Observing that the states within a miniband are degenerate would support the hypothesis that the states are localized and not extended. In Appendix 4.7.1, we ex-

amine whether the states within a miniband have a measurable difference in frequency. We identify and estimate the uncertainty stemming from discretization of the unit cell to numerically solve Maxwell's equations for the photonic bandstructure. The band width (i.e., the difference between the maximum and minimum eigenfrequencies in a miniband) is also estimated. We observe that the uncertainty is typically larger than the band width and, therefore, the frequencies of states within the miniband cannot be discriminated from one another (if the differences are theoretically nonzero). The results are also consistent with the states forming a miniband being degenerate in frequency.

There are some effectively localized states in which the electric field is concentrated on a single SVE site. We refer to such states as *single site* (SS) states. There are other effectively localized states in which the field is distributed over multiple SVE sites. Such states are referred to as *multiple site* (MS) states. A characteristic feature of a localized state is an exponential falloff of the energy density from the localized site. In Appendix 4.7.2, we check whether the exponential falloff is observed in examples of SS and MS states to determine to what extent the states are localized. The results show that both SS and MS states are composed of exponentially localized field configurations, which are centered on individual SVE sites.

4.7.1 Degenerate states in minibands

To determine whether the frequencies of a set of states forming a miniband can be discriminated from one another, we need an estimate of the numerical uncertainty stemming from the procedure used to compute the bandstructure. In this Appendix, we estimate the uncertainty that stems from the fact that, when numerically solving Maxwell's equations, an initial step is to discretize the unit cell into a grid of pixels.

The number of pixels $N \times N$ per unit cell, which we call the *resolution*, is a simulation parameter that can be changed. In the $N \to \infty$ limit (assuming the

pixels are uniformly distributed in the unit cell), the pixelated unit cell approaches the ideal unit cell. However, for all simulations, N is necessarily finite. Therefore, the discretized unit cell is always an approximation of—and never equal to—the analytically defined unit cell. This approximation leads to some amount of numerical uncertainty in the computed values of frequency ω. We call this the *uncertainty from resolution* and denote it by $d\omega$.

We denote the frequency range of a miniband (i.e., the difference between the largest and smallest frequencies in a miniband) by $\Delta\omega$ and call it the *band width*. To resolve the frequency differences between states within a miniband—if the states are not degenerate—the uncertainty $d\omega$ must be less than $\Delta\omega$, i.e.,

$$\Delta\omega > d\omega \ . \tag{4.11}$$

However, as we show below, our estimates indicate that $d\omega/\Delta\omega \sim 10^2$. Therefore, within the uncertainties, the observations are consistent with the states forming a miniband being degenerate in frequency.

Uncertainty from resolution

We obtain an estimate of the uncertainty from resolution $d\omega$ using the following procedure: We first choose an LI class γ and make a rendition (i.e., choose a set of phases γ_i and degree of approximant). Next, we compute the bandstructure of this rendition, first using 512×512 pixels in the unit cell. Let ω^i_{512} denote the ith largest eigenfrequency. We then compute the bandstructure of the same rendition, now using 1024×1024 resolution. Let ω^i_{1024} denote the ith largest eigenfrequency computed at 1024×1024 resolution. The relative change $\delta\omega^i$ in the computed values of the frequencies

$$\delta\omega^i \equiv \frac{\omega^i_{521} - \omega^i_{1024}}{\omega^i_{1024}} \tag{4.12}$$

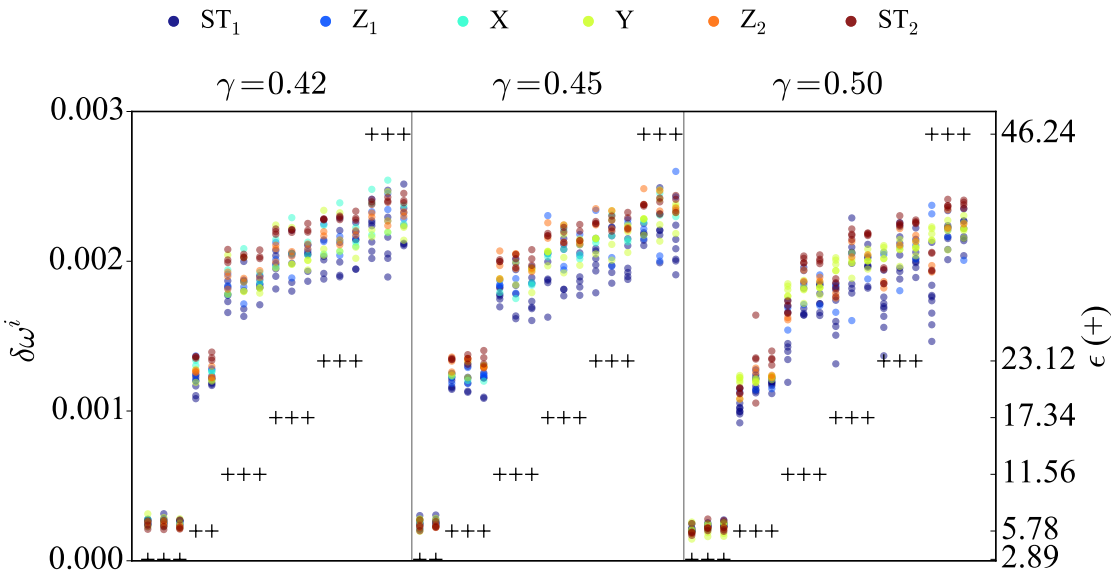

Figure 4.10: **Estimating the uncertainty from resolution** $d\omega$**.** For a fixed rendition from LI class γ and with dielectric constant ϵ, the bandstructure is computed, first at 512×512 resolution, then at 1024×1024 resolution. The relative change in the frequencies $\delta\omega^i$ (defined in Eq. (4.12)) for states in the minibands is shown here (colored circles, left vertical axis). Each position along the horizontal axis corresponds to a fixed rendition from an LI class γ and with dielectric constant ϵ. The LI class is labeled above each subpanel. The dielectric constant is shown as a +, with values along the right vertical axis.

gives an estimate of $d\omega/\omega$.

We compute $\delta\omega^i$ for all of the states lying in the minibands. We repeat this calculation for three LI classes ($\gamma = 0.42, 0.45, 0.50$), three renditions from each LI class, and six values of the dielectric constant ϵ. The results are shown in Fig. 4.10.

We observe that all of the values of $\delta\omega^i$ are less than 0.3%. This upper bound gives a conservative estimate of $d\omega/\omega$:

$$\frac{d\omega}{\omega} \sim 3 \times 10^{-3} \ . \tag{4.13}$$

Using a typical frequency of these states $\omega \sim 0.3$ (in units of $2\pi c/a$), we obtain an estimate of the absolute uncertainty from resolution $d\omega$ (the main result):

$$d\omega = \left(\frac{d\omega}{\omega}\right)\omega \sim \left(3 \times 10^{-3}\right) 0.3 \sim 10^{-3} \ . \tag{4.14}$$

There are some additional observations that can be made from Fig. 4.10: The relative change in frequency $\delta\omega^i$ is always positive. Therefore, as the resolution increases, the computed values of ω systematically decrease. Such a systematic trend is consistent with the values of ω converging from above as the resolution increases. We also observe that, for the same dielectric constant, there does not appear to be any systematic difference in $\delta\omega^i$ between different LI classes or between different renditions from the same LI class. However, as ϵ increases, there appears to also be an increase (on average) in $\delta\omega^i$.

Band width

We now turn to an estimate the band width $\Delta\omega$. Our procedure is as follows: We first choose an LI class γ, make a rendition (i.e., choice of degree of approximant and choice of phases γ_i whose sum is γ), and compute the bandstructure. The bandstructure will, in general, contain minibands. For each miniband, the band width $\Delta\omega$ is computed by subtracting the minimum frequency in the miniband from the maximum frequency in the miniband. The band widths are plotted in Fig. 4.11, where different rows correspond to the different minibands. Each position along the horizontal axis corresponds to one rendition. Each miniband is divided into subpanels according to the number of SVEs n in the rendition of the miniband type (e.g., for the ST_1 miniband shown in the topmost plot, n is the number of ST_1 sites). Within each subpanel, the value of n is shown, and the renditions are ordered according to increasing $\Delta\omega$.

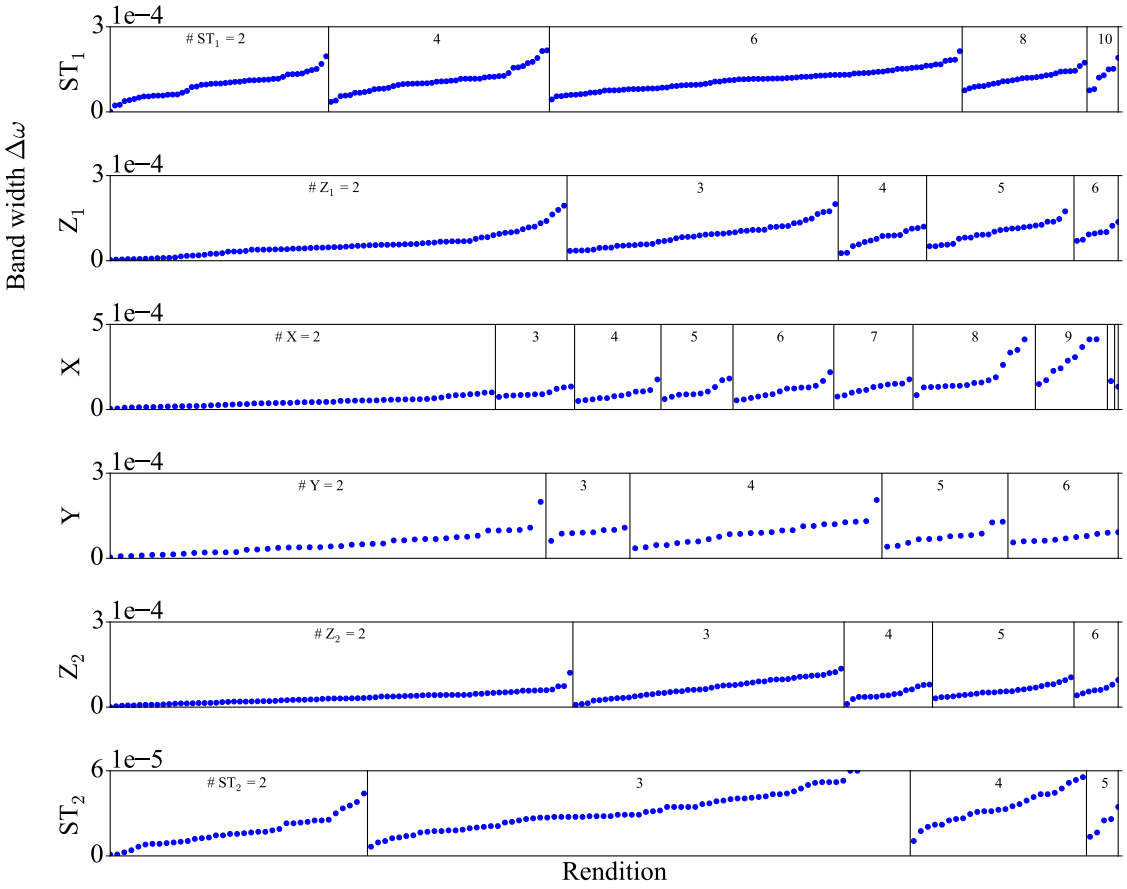

Figure 4.11: **Estimating band width $\Delta\omega$.** For a fixed rendition from LI class γ, the bandstructure is computed. For each miniband, we compute the band width $\Delta\omega$ (i.e., the difference between the maximum and minimum eigenfrequencies in the miniband). This is repeated for several renditions from four LI classes ($\gamma = 0.38, 0.42, 0.45, 0.50$). Shown here are the band widths $\Delta\omega$. The different rows correspond to the different minibands. Each row has been divided into subpanels according to the number of SVE sites n of the miniband type (e.g., for the first row, n is the number of ST_1 sites and, for the second row, n is the number of Z_1 sites). The values of n are shown at the top of each subpanel. Within each subpanel, the renditions are ordered according to increasing $\Delta\omega$.

The minibands—with the possible exception of the X miniband—have a band width $\Delta\omega$ that does not systematically increase as the number of SVEs increases. Moreover, it appears that

$$\Delta\omega \sim 10^{-4} \ . \tag{4.15}$$

(The ST_2 band is an exception, which has band width 10^{-5}.)

We have estimated the uncertainty due to finite resolution (pixelization) to be $d\omega \sim 10^{-3}$ and the band width to be $\Delta\omega \sim 10^{-4}$. Our estimates show that the uncertainty is greater than the band width. Thus, the frequencies of different states within a given miniband cannot be discriminated from one another. The results are consistent with the states forming a miniband being degenerate in frequency. Initial studies using increased resolutions up to 2048×2048 show that $\Delta\omega$ decreases with resolution, which is also consistent with the minibands comprising degenerate states.

4.7.2 Exponentially localized electric-field energy density

A characteristic feature of a localized state is an exponential falloff of the energy density from the localized site. In this Appendix, we check whether the exponential falloff is observed in examples of SS and MS states to determine to what extent the states are localized. Three states are examined. The states are frequency eigenstates of the same rendition (i.e., the same phases γ_i and same approximant) of LI class $\gamma = 0.45$.

We first establish notation. Let $E^2(\mathbf{r})$ be the electric-field energy density of a frequency eigenstate from a miniband, where $\mathbf{r}$ denotes the position in the unit cell. Let $\mathbf{x}$ denote the position of the central vertex of one of the sites of the SVE type corresponding to the miniband. We compute the maximum value of the energy density

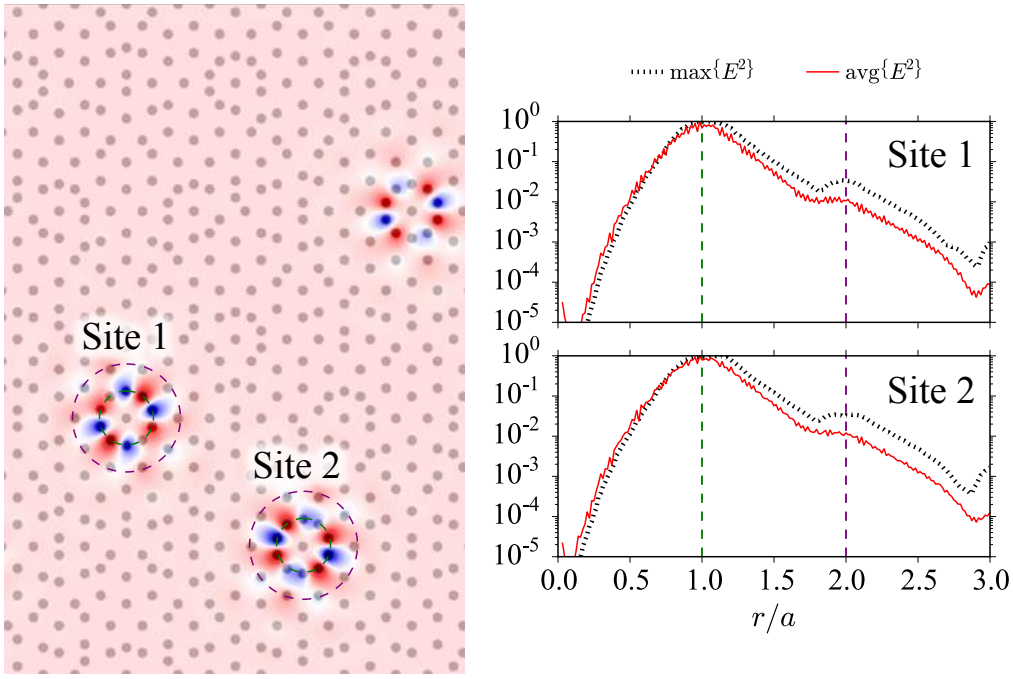

Figure 4.12: **Electric-field energy density E^2 of an ST_1 MS state *versus* distance r from central vertex of ST site.** The distance r is in units of the tile edge length a. (Left) The electric field distribution in unit cell for an MS state from the ST_1 miniband, overlaid on the point pattern. Blue/red/white correspond to negative/positive/zero field. (Upper Right) The maximum value of E^2 at distance r from Site 1 is shown as a red, solid line. This quantity is defined in Eq. (4.16). The average value of E^2 at distance r from Site 1 is shown as a black, dotted line. This quantity is defined in Eq. (4.17). Vertical dashed lines denote $r/a = 1$ (green, dashed), which is where the first nearest neighbors are located, and $r/a = 2$ (purple, dashed), which is roughly where the second nearest neighbors are located. Dashed circles with radii $r/a = 1, 2$ and centered at Site 1 are shown in the Left panel. (Lower Right) Same quantities as plotted in the the Upper Right panel but for Site 2.

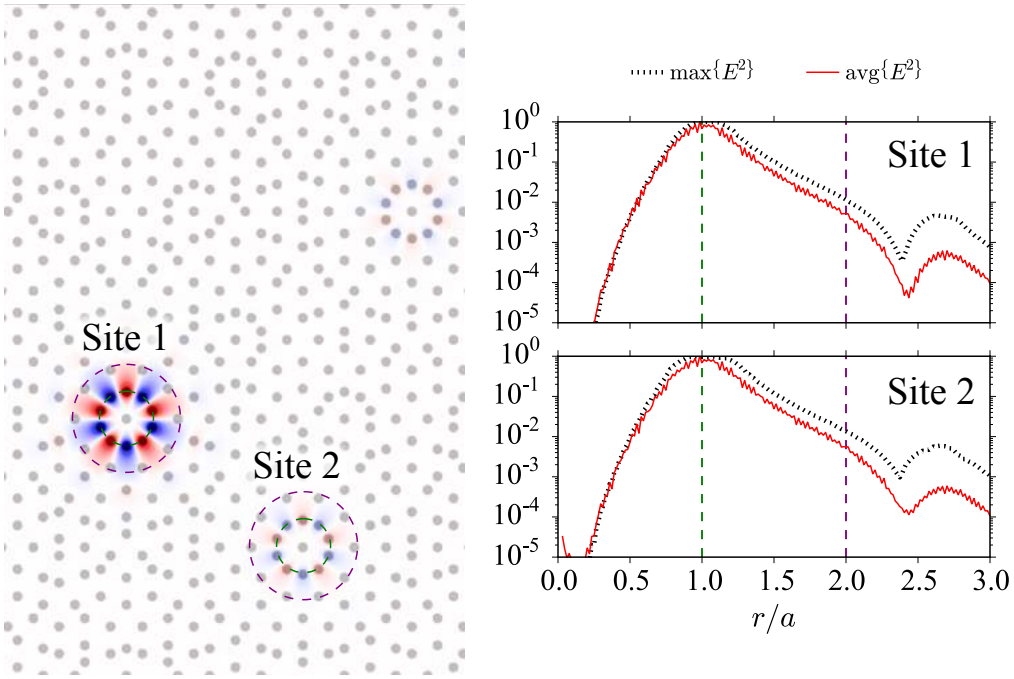

Figure 4.13: **Electric-field energy density E^2 of an ST_2 SS state *versus* distance r from central vertex of ST site.** Quantities that are described in the Fig. 4.12 caption are presented here for an ST_2 SS state.

$E^2(\mathbf{r})$ around a circle of radius r centered at $\mathbf{x}$

$$\max_{r=|\mathbf{r}-\mathbf{x}|} \left\{E^2(\mathbf{r})\right\} \ , \tag{4.16}$$

as well as the average value of the energy density around the circle of radius r centered at $\mathbf{x}$:

$$\operatorname{avg}_{r=|\mathbf{r}-\mathbf{x}|} \left\{E^2(\mathbf{r})\right\} \ . \tag{4.17}$$

The first state we consider is an ST_1 MS state. Its electric field distribution $E(\mathbf{r})$ is shown in the left panel of Fig. 4.12. There are three ST sites in this rendition and the field is non-negligible on each site. For illustrative purposes, we show the quantities

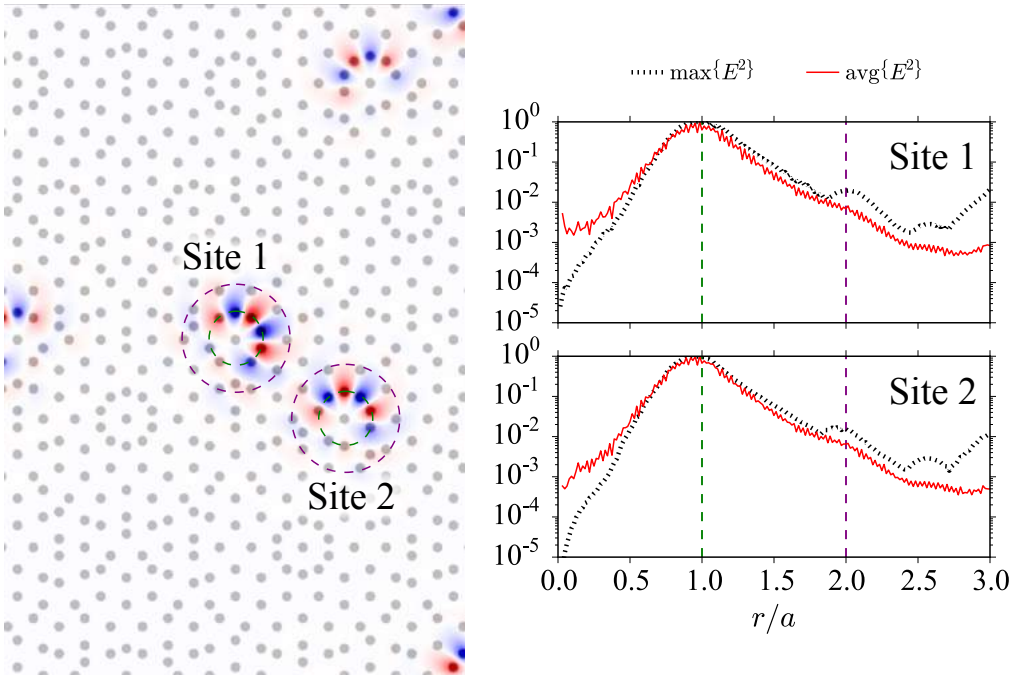

Figure 4.14: **Electric-field energy density E^2 of an X MS state *versus* distance r from central vertex of X site.** Quantities that are described in the Fig. 4.12 caption are presented here for an X MS state.

defined in Eq. (4.16) and Eq. (4.17) evaluated (right panel of Fig. 4.12) at two of the three ST sites. The maximum energy density at distance r, computed according to Eq. (4.16), is shown as red solid lines versus r. The average energy density at distance r, computed according to Eq. (4.17), is shown as black, dotted lines. Both quantities have been normalized so that the peak value is set to one.

In Fig. 4.12, we observe that the maximum and average values of E^2 peak around $r/a \approx 1$, which is where the first nearest neighbors are located. The values drop to $\lesssim 1\%$ of the peak values by $r/a \approx 2$ and $\lesssim .01\%$ of the peak values by $r/a \approx 3$. There appears to initially be a log-linear falloff as r/a increases from $r/a = 1$. There is then a flattening around $r/a = 2$, which roughly corresponds to the positions of

the second nearest neighbors. Finally, at $r/a \gtrsim 2$, there appears to a be a faster than log-linear falloff. The curves appear to be viritually identical for the two sites. The observed log-linear behavior and the observed similarities of the curves for the two ST sites both suggest that the energy density is exponentially localized on individual ST sites. For both sites, the background energy density, which we take to be the peak energy density in a region at the top left of the unit cell far removed from the ST sites, is $\sim 10^{-6}$ (on the normalized scale).

The analysis is repeated for an ST_2 SS state. Its electric field distribution $E(\mathbf{r})$ is shown in the left panel of Fig. 4.13. The right panels here contain the same quantities that were evaluated above in the right panels of Fig. 4.12. We consider the energy density profiles around the same two ST sites as before. In Fig. 4.13, we continue to observe a log-linear falloff of the energy density. The degree of flattening around $r/a \approx 2$ is less than for the ST_1 states. Instead of the second resonance that was observed at $r/a \approx 2$ in Fig. 4.12, there is now a second resonance around $r/a \approx 2.5$. Interestingly, despite the fact that the power of $E(\mathbf{r})$ is largely concentrated around Site 1 and not on Site 2, the normalized profiles of the curves appear to be virtually identical. As with the ST_1 states, the log-linear behavior and similarities of the curves for the two ST sites suggest that the energy density is exponentially localized on individual ST sites. For Site 1, the background energy density, which is computed in the same way as it was for the ST_1 MS state, is $\sim 10^{-6}$ (on the normalized scale). For Site 2, the background is $\sim 10^{-4}$.

The third state we examine is an X MS state. Its electric field distribution $E(\mathbf{r})$ is shown in the left panel of Fig. 4.14. There are four X sites in this rendition and the field is non-negligible on each site. We repeat the procedure to compute Eq. (4.16) and Eq. (4.17) for two of the sites, the results of which are contained in the right panel of Fig. 4.14. There are some similarities with the ST_1 and ST_2 states. For example, (i) the energy density peaks at the position of the first nearest neighbors $r/a = 1$, (ii)

there is a falloff for $r/a > 1$ that is initially log-linear, and (iii) the curves are virtually identical for the two X sites. There are also some differences. There appears to be both a resonance at $r/a \approx 2$ and a resonance at $r/a \approx 2.5$. Moreover, the curves turn upward around $r/a \approx 2.75$. The midpoint between the two sites lies approximately at $r/a \approx 2.5$, which suggests that the upturn in the energy density is simply due to the fact that the two X sites are adjacent. Altogether, the observations for the X sites are consistent with the energy density being exponentially localized on individual X sites. For both sites, the background energy density, which we take to be the peak energy density in a region at the bottom left of the unit cell far removed from the X sites, is $\sim 10^{-5}$ (on the normalized scale).

The above analysis suggests that the frequency eigenstates—both SS and MS—are composed of exponentially localized configurations centered on individual SVE sites.

4.8 Appendix: Decorations and air-localized states

In this Appendix, we present results showing that the presence of effectively localized states persists upon changing the decoration of the tiling. Two further choices of decoration are studied, one in which the scatterers are placed at tile centers, and one in which the scatterers are placed at the centroids of the Delaunay-triangulated tiling. The latter construction can be performed simply as follows: Take a tile (fat or skinny) and draw perpendicular bisectors from each edge, extending into the interior of the tile, until the bisectors each encounter another bisector. (Because the rhombus tiles are not squares, there will never be a point of intersection between more than two bisectors). At that point of intersection, place a scatterer. By this construction, every tile will contain two scatterers.

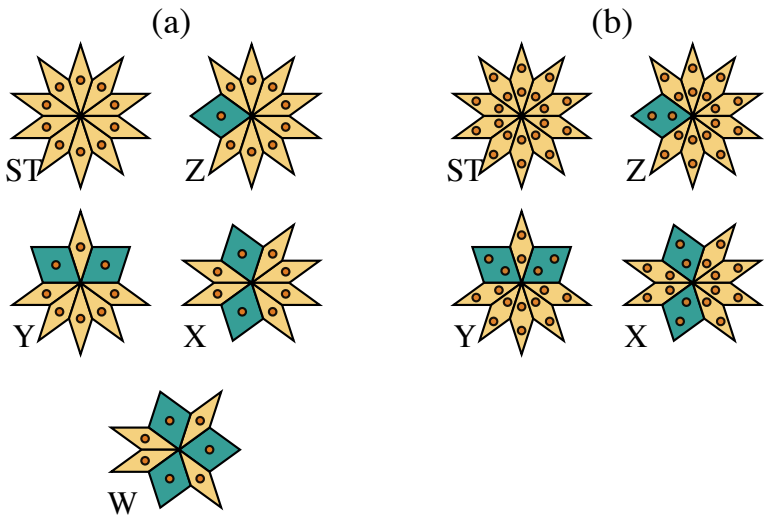

Figure 4.15: SVEs for center-decorated structures (left) and for Delaunay-decorated structures (right). Overlaid on the SVEs are the scatterer configurations.

Following the same procedure as discussed in Section 4.3 to calculate the TM bandstructure, we find that both center-decorated structures and Delaunay-decorated structures have effectively localized states. The X, Y, Z and ST vertex environments continue to be SVEs. The center-decorated structures have one additional SVE in the W vertex environment. The decorated SVEs are shown in Fig. 4.15. We also find analogous counting formulae for the new structures.

We continue to observe effectively localized states lying in the fundamental bandgap in which the field is concentrated in the *dielectric* component. However, there is an additional novelty in the center-decorated structures. There are states in which the field is concentrated in the *air* component. Representative examples of these "air-localized states" are shown in Fig. 4.16b, where they are labeled with asterisks (*). The frequencies of the air-localized states lie near the upper edge of the fundamental bandgap. This is intuitively expected; typically, states below the fundamental bandgap have an electric field distribution that is concentrated in the dielectric component, whereas states above the bandgap have field concentrated in the air component.

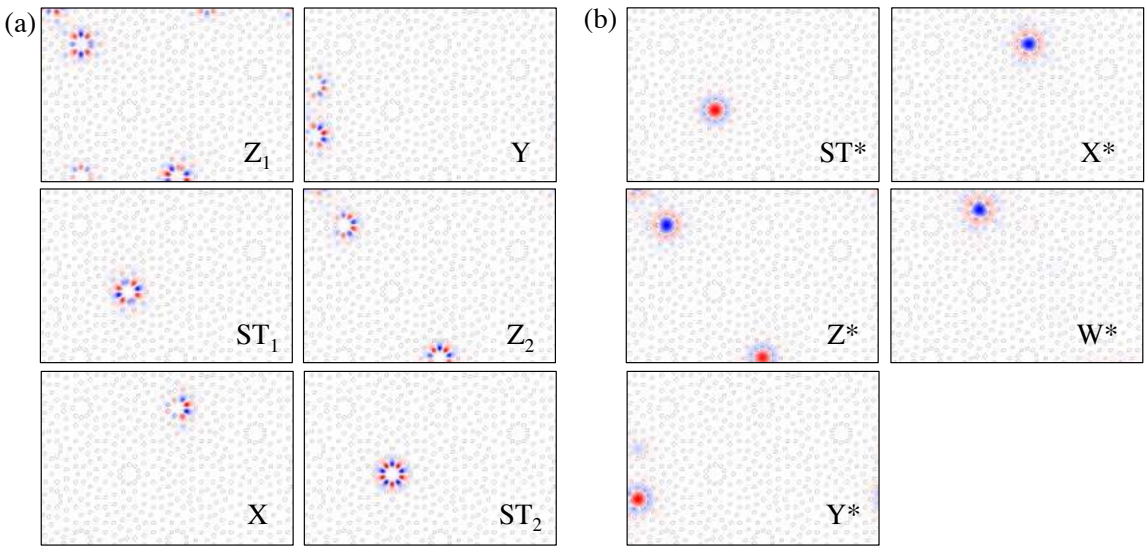

Figure 4.16: **Representative examples of effectively localized states in center-decorated structures.** (a) Examples of states that have electric field concentrated in the *dielectric* component (i.e., within scatterers). (b) Examples of states that have electric field concentrated in the *air* component (i.e., between scatterers). Blue/red/white correspond to negative/positive/zero field.

Chapter 5

Conclusion and Outlook

Throughout this thesis, we have focused on recent studies of natural quasicrystals and quasicrystal tilings. Now, in this Chapter, we reflect upon the main conclusions from these studies to see what they suggest about future developments.

In Chapter 2, we presented direct evidence from fragment 126A of the Khatyrka meteorite that shows cross-cutting relationships and redox reaction between Al-Cu-Fe alloys and silicate melt. The new evidence clearly demonstrates that some Al-Cu-Fe alloys (including quasicrystals) formed prior to an impact event a few 100 Ma. The alloy phases may even have formed as early as 4.564 Ga, which would place them among the oldest condensed phases in the Solar System. The new evidence settles the question about the natural origin of the Al-Cu phases and places the focus squarely on the main scientific quandary, namely, *how did the metallic Al and Cu first form and come together?* Resolving this question requires new and previously unrecognized processes in the early Solar System. Our earlier discoveries of the first observed Al-bearing Fe-Ni alloy minerals (steinhardtite and decagonite) have already confronted the conventional thinking of planetary structure: their existence suggests that Al may be a contributor to the anomalously low density of the Earth's core, which is thought to be predominantly Fe-Ni. Before the discoveries of steinhardtite and decagonite,

such a proposal would have been unthinkable because natural metallic Al was not thought to exist at all!

The results from Chapter 2 also have implications for our understanding of the stability and formation of quasicrystals. Some of the quasicrystals in Khatyrka formed during the most recent impact event a few 100 Ma and have been pristinely preserved to the present day. Among these is the as-yet-unnamed icosahedral phase of Al-Cu-Fe. The formation of this new quasicrystalline phase during the impact event is consistent with the hypothesis that shock conditions are sufficient for forming quasicrystals. This hypothesis was supported by the Asimow shock recovery experiment, which led to the production of a novel quinary icosahedral quasicrystal. Shock-synthesis of quasicrystals is vastly different from the established metallurgical techniques for growing quasicrystals, e.g., rapid quench or conventional solidification. The unanticipated discoveries of novel quasicrystals in Khatyrka and in the shock experiment indicate that we do not yet fully know or understand all of the mechanisms through which quasicrystals form. We expect that ongoing investigations of Khatyrka and other rocks and meteorites will reveal additional novel phases and, possibly, new quasicrystals. Such discoveries would inform us about novel routes for quasicrystal synthesis and would deepen our understanding of quasicrystal stability and formation.

In Chapters 3 and 4, we uncovered unexpected structural and physical differences between local isomorphism classes of quasicrystals. One may have thought that the degree of hyperuniformity does not vary with LI class, but as we showed in Chapter 3, this is clearly not true. The degree of hyperuniformity does vary with LI class, and, moreover, the variation appears to be largely determined by the local structure (e.g., by the Voronoi area distribution). In Chapter 4, we showed that photonic quasicrystal heterostructures derived from a continuous set of LI classes have effectively localized TM states in the fundamental bandgap. We also found that the Penrose LI class—by far the most heavily studied LI class of pentagonal quasicrystals—is the one LI

class that does not have effectively localized states. This exemplifies how systematic ignorance of the continuum of LI classes could lead one to overlook potentially interesting physics. In a broader context, our results demonstrate that the physical and structural properties of the full continuum of LI classes—beyond a select subset of LI classes—warrants further study. While our studies of local isomorphism classes have specifically been on pentagonal quasicrystal tilings, the notion of local isomorphism classes applies generally to all quasicrystals. For example, it is known that among icosahedral quasicrystals, only one LI class can be generated by the direct projection method from six-dimensions with a standard window. We expect that new and useful physical properties remain to be discovered among the continuum of LI classes. These discoveries will come at a time when continued innovations in fabrication techniques allow for greater flexibility in the design and production of perfect quasicrystalline structures.

Bibliography

1. Shechtman, D., Blech, I., Gratias, D. & Cahn, J. W. Metallic Phase with Long-Range Orientational Order and No Translational Symmetry. *Physical Review Letters* **53,** 1951–1953 (1984).

2. Kittel, C. & Holcomb, D. F. Introduction to solid state physics. *American Journal of Physics* **35,** 547–548 (1967).

3. Shechtman, D. & Blech, I. The microstructure of rapidly solidified Al_6Mn. *Metallurgical and Materials Transactions A* **16,** 1005–1012 (1985).

4. Stephens, P. W. & Goldman, A. I. Sharp diffraction maxima from an icosahedral glass. *Physical review letters* **56,** 1168 (1986).

5. Pauling, L. Apparent icosahedral symmetry is due to directed multiple twinning of cubic crystals. *Nature* **317,** 512–514 (1985).

6. Pauling, L. So-called icosahedral and decagonal quasicrystals are twins of an 820-atom cubic crystal. *Physical review letters* **58,** 365 (1987).

7. Pauling, L. Icosahedral quasicrystals of intermetallic compounds are icosahedral twins of cubic crystals of three kinds, consisting of large (about 5000 atoms) icosahedral complexes in either a cubic body-centered or a cubic face-centered arrangement or smaller (about 1350 atoms) icosahedral complexes in the β-tungsten arrangement. *Proceedings of the National Academy of Sciences* **86,** 8595–8599 (1989).

8. Levine, D. & Steinhardt, P. J. Quasicrystals: A New Class of Ordered Structures. *Physical Review Letters* **53,** 2477–2480 (Dec. 1984).

9. Steinhardt, P. J. Quasicrystals: a brief history of the impossible. *Rendiconti Lincei* **24,** 85–91 (2013).

10. Levine, D. & Steinhardt, P. J. Quasicrystals. I. Definition and structure. *Physical Review B* **34,** 596–616 (July 1986).

11. Socolar, J. E. S. & Steinhardt, P. J. Quasicrystals. II. Unit-cell configurations. *Physical Review B* **34,** 617–647 (1986).

12. Steinhardt, P. J. & DiVincenzo, D. P. *Quasicrystals: the state of the art; 2nd ed.* (World Scientific, Singapore, 1999).

13. Janot, C. *Quasicrystals: a primer* (OUP Oxford, 2012).

14. Penrose, R. The role of aesthetics in pure and applied mathematical research. *The Institute of Mathematics and its Applications Bulletin* **10,** 266–271 (1974).

15. Tsai, A.-P., Inoue, A. & Masumoto, T. A Stable Quasicrystal in Al-Cu-Fe System. *Japanese Journal of Applied Physics* **26,** L1505–L1507 (1987).

16. Tsai, A.-P. Discovery of stable icosahedral quasicrystals: progress in understanding structure and properties. *Chemical Society Reviews* **42,** 5352–5365 (2013).

17. Bancel, P. A. in *Quasicrystals: the state of the art* (eds DiVincenzo, D. & Steinhardt, P. J.) 17–55 (World Scientific, Singapore, 1991).

18. Henley, C. in *Quasicrystals: the state of the art* (eds DiVincenzo, D. & Steinhardt, P. J.) 429–524 (World Scientific, Singapore, 1991).

19. Steurer, W. & Deloudi, S. Fascinating quasicrystals. *Acta Crystallographica Section A: Foundations of Crystallography* **64,** 1–11 (2008).

20. Bindi, L, Steinhardt, P. J., Yao, N & Lu, P. J. Natural Quasicrystals. *Science* **324,** 1306–1309 (June 2009).

21. Bindi, L., Steinhardt, P. J., Yao, N. & Lu, P. J. Icosahedrite, $Al_{63}Cu_{24}Fe_{13}$, the first natural quasicrystal. *American Mineralogist* **96,** 928–931 (2011).

22. Bindi, L. *et al.* Evidence for the extraterrestrial origin of a natural quasicrystal. *Proceedings of the National Academy of Sciences* **109,** 1396–1401 (2012).

23. MacPherson, G. J. *et al.* Khatyrka, a new CV3 find from the Koryak Mountains, Eastern Russia. *Meteoritics & Planetary Science* **48,** 1499–1514 (Aug. 2013).

24. Lin, C. *et al.* Evidence of cross-cutting and redox reaction in Khatyrka meteorite reveals metallic-Al minerals formed in outer space. *Scientific Reports* (To Appear).

25. Ma, C., Lin, C., Bindi, L. & Steinhardt, P. J. Hollisterite (Al_3Fe), kryachkoite $(Al,Cu)_6(Fe,Cu)$, and stolperite (AlCu): Three new minerals from the Khatyrka CV3 carbonaceous chondrite. *American Mineralogist* **102,** 690–693 (Mar. 2017).

26. Bindi, L., Lin, C., Ma, C. & Steinhardt, P. J. Collisions in outer space produced an icosahedral phase in the Khatyrka meteorite never observed previously in the laboratory. *Scientific Reports* **6,** 38117 (Dec. 2016).

27. Asimow, P. D. *et al.* Shock synthesis of quasicrystals with implications for their origin in asteroid collisions. *Proceedings of the National Academy of Sciences* **113,** 7077–7081 (June 2016).

28. Lin, C., Steinhardt, P. J. & Torquato, S. Hyperuniformity variation with quasicrystal local isomorphism class. *Journal of Physics: Condensed Matter* **29** (2017).

29. Torquato, S. & Stillinger, F. H. Local density fluctuations, hyperuniformity, and order metrics. *Physical Review E* **68** (2003).

30. Zachary, C. E. & Torquato, S. Hyperuniformity in point patterns and two-phase random heterogeneous media. *Journal of Statistical Mechanics: Theory and Experiment* **2009,** P12015 (2009).

31. Torquato, S. Hyperuniformity and its generalizations. *Physical Review E* **94** (2016).

32. Florescu, M., Torquato, S. & Steinhardt, P. J. Complete band gaps in two-dimensional photonic quasicrystals. *Physical Review B* **80,** 155112 (Oct. 2009).

33. Florescu, M., Torquato, S. & Steinhardt, P. J. Designer disordered materials with large, complete photonic band gaps. *Proceedings of the National Academy of Sciences* **106,** 20658–20663 (Dec. 2009).

34. Hejna, M., Steinhardt, P. J. & Torquato, S. Nearly hyperuniform network models of amorphous silicon. *Physical Review B* **87,** 245204 (2013).

35. Zhang, G, Stillinger, F. & Torquato, S. The Perfect Glass Paradigm: Disordered Hyperuniform Glasses Down to Absolute Zero. *Scientific Reports* **6** (2016).

36. Steinhardt, P. J. & Bindi, L. Once upon a time in Kamchatka: the search for natural quasicrystals. *Philosophical Magazine* **91,** 2421–2426 (2011).

37. Steinhardt, P. J. & Bindi, L. In search of natural quasicrystals. *Reports on Progress in Physics* **75,** 092601 (Aug. 2012).

38. Bindi, L. & Steinhardt, P. J. The discovery of the first natural quasicrystal. *Elements* **8,** 13–14 (2012).

39. Bindi, L. & Steinhardt, P. J. The quest for forbidden crystals. *Mineralogical Magazine* **78,** 467–482 (Apr. 2014).

40. Wolchover, N. In a Grain, a Glimpse of the Cosmos. *Quanta Magazine* (2014).

41. Lu, P. J., Deffeyes, K., Steinhardt, P. J. & Yao, N. Identifying and indexing icosahedral quasicrystals from powder diffraction patterns. *Physical Review Letters* **87,** 275507 (2001).

42. Clayton, R. N., Onuma, N. & Mayeda, T. K. A classification of meteorites based on oxygen isotopes. *Earth and Planetary Science Letters* **30,** 10–18 (1976).

43. MacPherson, G. J. in *Treatise on Geochemistry* 139–179 (Elsevier, 2014).

44. Mcsween Jr., H. Y. Petrographic variations among carbonaceous chondrites of the Vigarano type. *Geochimica et Cosmochimica Acta* **41,** 1777–1790 (Dec. 1977).

45. Weinbruch, S., Palme, H., Müller, W. F. & El Goresy, A. FeO-rich rims and veins in Allende forsterite: Evidence for high temperature condensation at oxidizing conditions. *Meteoritics* **25,** 115–125 (June 2012).

46. Krot, A. N., Scott, E. R. D. & Zolensky, M. E. Mineralogical and chemical modification of components in CV3 chondrites: Nebular or asteroidal processing? *Meteoritics* **30,** 748–775 (June 2012).

47. Scott, E. R. D. & Krot, A. N. in *Treatise on Geochemistry* 65–137 (Elsevier, 2014).

48. Ebel, D. S. *et al.* Abundance, major element composition and size of components and matrix in CV, CO and Acfer 094 chondrites. *Geochimica et Cosmochimica Acta* **172,** 322–356 (Jan. 2016).

49. Brearley, A. J. & Jones, R. H. Chondritic meteorites. *Reviews in Mineralogy and Geochemistry* **36,** 1–398 (1998).

50. Bindi, L. *et al.* Natural quasicrystal with decagonal symmetry. *Scientific Reports* **5,** 9111 (Mar. 2015).

51. Bindi, L. *et al.* Steinhardtite, a new body-centered-cubic allotropic form of aluminum from the Khatyrka CV3 carbonaceous chondrite. *American Mineralogist* **99,** 2433–2436 (Nov. 2014).

52. Ma, C., Lin, C., Bindi, L. & Steinhardt, P. J. Discovery of new Al-Cu-Fe minerals in the Khatyrka CV3 meteorite (Abstract 6017). *79th Annual Meeting of the Meteoritical Society.*

53. Grossman, L., Beckett, J. R., Fedkin, A. V., Simon, S. B. & Ciesla, F. J. Redox conditions in the solar nebula: Observational, experimental, and theoretical constraints. *Reviews in Mineralogy and Geochemistry* **68,** 93–140 (2008).

54. Hollister, L. S. *et al.* Redox reactions between Cu-Al metal and silicates in the Khatyrka meteorite (Abstract 2394). *Lunar and Planetary Science Conference XLVI.*

55. Hollister, L. S. *et al.* Impact-induced shock and the formation of natural quasicrystals in the early solar system. *Nature Communications* **5,** 1306 (June 2014).

56. Ma, C. *et al.* Ahrensite, γ-Fe_2SiO_4, a new shock-metamorphic mineral from the Tissint meteorite: Implications for the Tissint shock event on Mars. *Geochimica et Cosmochimica Acta* **184,** 240–256 (July 2016).

57. Ohtaka, O., Tobe, H. & Yamanaka, T. Phase equilibria for the Fe_2SiO_4-Fe_3O_4 system under high pressure. *Physics and Chemistry of Minerals* **24,** 555–560 (Oct. 1997).

58. Meier, M. M. M. *et al.* Shedding Light on the Origin of the Quasicrystal-bearing Khatyrka Meteorite (Abstract 5035). *78th Annual Meeting of the Meteoritical Society.*

59. Meier, M. M. M. *et al.* Cosmic-Ray Exposure and Shock Degassing Ages of the Quasicrystal-Bearing Khatyrka Meteorite (Abstract 1226). *Lunar and Planetary Science Conference XLVII.*

60. Stöffler, D., Keil, K. & Edward R D, S. Shock metamorphism of ordinary chondrites. *Geochimica et Cosmochimica Acta* **55,** 3845–3867 (Dec. 1991).

61. Rubin, A. E. Metallic copper in ordinary chondrites. *Meteoritics* **29,** 93–98 (June 2012).

62. Tomkins, A. G. What metal-troilite textures can tell us about post-impact metamorphism in chondrite meteorites. *Meteoritics & Planetary Science* **44,** 1133–1149 (Jan. 2010).

63. Xie, X. & Chen, M. *Suizhou Meteorite: Mineralogy and Shock Metamorphism* (Springer Berlin Heidelberg, Berlin, Heidelberg, 2016).

64. Stagno, V. *et al.* Icosahedral AlCuFe quasicrystal at high pressure and temperature and its implications for the stability of icosahedrite. *Scientific Reports* **4,** 2477 (July 2014).

65. Stagno, V. *et al.* Quasicrystals at extreme conditions: The role of pressure in stabilizing icosahedral $Al_{63}Cu_{24}Fe_{13}$ at high temperature. *American Mineralogist* **100,** 2412–2418 (Nov. 2015).

66. Ramsay, J. G. *Folding and fracturing of rocks* (McGraw-Hill, 1967).

67. Fredriksson, K. & Kerridge, J. F. Carbonates and Sulfates in CI Chondrites: Formation by Aqueous Activity on the Parent Body. *Meteoritics* **23,** 35–44 (June 2012).

68. Jarosewich, E. Chemical analyses of meteorites: A compilation of stony and iron meteorite analyses. *Meteoritics* **25,** 323–337 (June 2012).

69. Shi, N. *et al.* Naquite, FeSi, a new mineral species from Luobusha, Tibet, Western China. *Acta Geologica Sinica* **86,** 533–538 (3 2012).

70. Keil, K., Berkley, J. L. & Fuchs, L. H. Suessite, Fe_3Si, a new mineral in the North Haig ureilite (Abstract 154). *43rd Annual Meeting of the Meteoritical Society* (1980).

71. Zuxiang, Y. Two new minerals gupeiite and xifengite in cosmic dusts from Yanshan. *Acta Petrologica Mineralogica et Analytica* **3,** 231–238 (1984).

72. Hamann, C., Stöffler, D. & Reimold, W. U. Interaction of aluminum projectiles with quartz sand in impact experiments: Formation of khatyrkite (CuAl2) and reduction of SiO2 to Si. *Geochimica et Cosmochimica Acta* **192,** 295–317 (Nov. 2016).

73. Chen, M., Sharp, T. G., El Goresy, A., Wopenka, B. & Xie, X. The Majorite-Pyrope + Magnesiowustite Assemblage: Constraints on the History of Shock Veins in Chondrites. *Science* **271,** 1570–1573 (Mar. 1996).

74. Fiske, P. S. *et al.* Pseudotachylites Generated in Shock Experiments: Implications for Impact Cratering Products and Processes. *Science* **270,** 281–283 (Oct. 1995).

75. Hamann, C., Hecht, L., Ebert, M. & Wirth, R. Chemical projectile–target interaction and liquid immiscibility in impact glass from the Wabar craters, Saudi Arabia. *Geochimica et Cosmochimica Acta* **121,** 291–310 (Nov. 2013).

76. Tomeoka, K., Yamahana, Y. & Sekine, T. Experimental shock metamorphism of the Murchison CM carbonaceous chondrite. *Geochimica et Cosmochimica Acta* **63,** 3683–3703 (Nov. 1999).

77. Berman, R. G. Internally-Consistent Thermodynamic Data for Minerals in the System Na_2O-K_2O-CaO-MgO-FeO-Fe_2O_3-Al_2O_3-SiO_2-TiO_2-H_2O-CO_2. *Journal of Petrology* **29,** 445–522 (Apr. 1988).

78. Ottonello, G., Princivalle, F. & Della Giusta, A. Temperature, composition, and f_{O_2} effects on intersite distribution of Mg and Fe2+ in olivines. *Physics and Chemistry of Minerals* **17,** 301–312 (Sept. 1990).

79. Saadi, N., Harmelin, M., Faudot, F. & Legendre, B. Enthalpy of formation of the $Al_{0.63}Cu_{0.25}Fe_{0.12}$ icosahedral phase. *Journal of non-crystalline solids* **153-154,** 500–503 (1993).

80. Boesenberg, J. S. & Hewins, R. H. An experimental investigation into the metastable formation of phosphoran olivine and pyroxene. *Geochimica et Cosmochimica Acta* **74,** 1923–1941 (Mar. 2010).

81. Van Roosbroek, N. *et al.* Immiscible silicate liquids and phosphoran olivine in Netschaëvo IIE silicate: Analogue for planetesimal core–mantle boundaries. *Geochimica et Cosmochimica Acta* **197,** 378–395 (Jan. 2017).

82. Tsai, A.-P., Inoue, A. & Masumoto, T. New decagonal Al–Ni–Fe and Al–Ni–Co alloys prepared by liquid quenching. *Materials transactions, JIM* **30,** 150–154 (1989).

83. Gayle, F. W., Shapiro, A. J., Biancaniello, F. S. & Boettinger, W. J. The Al-Cu-Fe phase diagram: 0 to 25 At. pct Fe and 50. *Metallurgical Transactions A* **23,** 2409–2417 (1992).

84. Zhang, L., Schneider, J. & Lück, R. Phase transformations and phase stability of the AlCuFe alloys with low-Fe content. *Intermetallics* **13,** 1195–1206 (Nov. 2005).

85. Gratias, D. *et al.* The phase diagram and structures of the ternary AlCuFe system in the vicinity of the icosahedral region. *Journal of non-crystalline solids* **153,** 482–488 (1993).

86. Bowen, N. L. & Schairer, J. F. The system MgO-FeO-SiO_2. *American Journal of Science* **s5-29,** 151–217 (Feb. 1935).

87. Lindholm, M. A thermodynamic description of the Fe-Cr-Si system with emphasis on the equilibria of the sigma (Σ) phase. *Journal of Phase Equilibria* **18,** 432–440 (Sept. 1997).

88. Murray, J. L. The aluminium-copper system. *International Metals Reviews* **30,** 211–234 (July 2013).

89. Massalski, T. B., Okamoto, H., Subramanian, P. R. & Kacprzak, L. *Binary alloy phase diagrams, vol. 3* (ASM International, 1990).

90. Essene, E. J. & Fisher, D. C. Lightning Strike Fusion: Extreme Reduction and Metal-Silicate Liquid Immiscibility. *Science* **234,** 189–193 (Oct. 1986).

91. Rowan, L. R. & Ahrens, T. J. Observations of impact-induced molten metal-silicate partitioning. *Earth and Planetary Science Letters* **122,** 71–88 (Mar. 1994).

92. Meibom, A. *et al.* Shock melts in QUE 94411, Hammadah al Hamra 237, and Bencubbin: Remains of the missing matrix? *Meteoritics & Planetary Science* **40,** 1377–1391 (Jan. 2010).

93. Bischoff, A. & Stöffler, D. Shock metamorphism as a fundamental process in the evolution of planetary bodies: Information from meteorites. *European Journal of Mineralogy* **4,** 707–755 (4 1992).

94. Zhang, J., Williams, D. B. & Goldstein, J. I. The microstructure and formation of duplex and black plessite in iron meteorites. *Geochimica et Cosmochimica Acta* **57,** 3725–3735 (Aug. 1993).

95. Ma, C. & Rossman, G. R. Barioperovskite, $BaTiO_3$, a new mineral from the Benitoite Mine, California. *American Mineralogist* **93,** 154–157 (Jan. 2008).

96. Ma, C. & Rossman, G. R. Tistarite, Ti_2O_3, a new refractory mineral from the Allende meteorite. *American Mineralogist* **94,** 841–844 (May 2009).

97. De Bruijn, N. G. Algebraic theory of Penrose's non-periodic tilings of the plane. I. *Indagationes Mathematicae (Proceedings)* **84,** 39–52 (1981).

98. De Bruijn, N. G. Algebraic theory of Penrose's non-periodic tilings of the plane. II. *Indagationes Mathematicae (Proceedings)* **84,** 53–66 (1981).

99. Ingersent, K. & Steinhardt, P. J. Matching rules and growth rules for pentagonal quasicrystal tilings. *Physical Review Letters* **64,** 2034–2037 (1990).

100. Oğuz, E. C., Socolar, J. E. S., Steinhardt, P. J. & Torquato, S. Hyperuniformity of quasicrystals. *Physical Review B* **95** (2017).

101. Kim, J. & Torquato, S. Effect of window shape on the detection of hyperuniformity via the local number variance. *Journal of Statistical Mechanics: Theory and Experiment* **2017,** 013402 (2017).

102. Pavlovitch, A. & Kléman, M. Generalised 2D Penrose tilings: structural properties. *Journal of Physics A: Mathematical and General* **20,** 687–702 (1987).

103. Zobetz, E. & Preisinger, A. Vertex frequencies in generalized Penrose patterns. *Acta Crystallographica Section A Foundations of Crystallography* **46,** 962–970 (1990).

104. Henley, C. L. Sphere packings and local environments in Penrose tilings. *Physical Review B* **34,** 797–816 (1986).

105. Entin-Wohlman, O., Kléman, M. & Pavlovitch, A. Penrose tiling approximants. *Journal de Physique* **49,** 587–598 (1988).

106. Joannopoulos, J. D., Johnson, S. G., Winn, J. N. & Meade, R. D. *Photonic Crystals: Molding the Flow of Light* (Princeton University Press, 2011).

107. Johnson, S. G. & Joannopoulos, J. D. Block-iterative frequency-domain methods for Maxwell's equations in a planewave basis. *Optics express* **8,** 173–190 (2001).

108. Rechtsman, M. C., Jeong, H.-C., Chaikin, P. M., Torquato, S. & Steinhardt, P. J. Optimized Structures for Photonic Quasicrystals. *Physical Review Letters* **101,** 073902 (Aug. 2008).

109. Tokihiro, T., Fujiwara, T. & Arai, M. Exact eigenstates on a two-dimensional Penrose lattice and their fractal dimensions. *Physical Review B* **38,** 5981–5987 (9 1988).

110. Repetowicz, P., Grimm, U. & Schreiber, M. Exact eigenstates of tight-binding Hamiltonians on the Penrose tiling. *Physical Review B* **58,** 13482 (1998).

111. Wang, K. Structural effects on light wave behavior in quasiperiodic regular and decagonal Penrose-tiling dielectric media: A comparative study. *Physical Review B* **76** (2007).

112. Wang, K. Light localization in photonic band gaps of quasiperiodic dielectric structures. *Physical Review B* **82** (2010).

113. Wang, Y., Hu, X., Xu, X., Cheng, B. & Zhang, D. Localized modes in defect-free dodecagonal quasiperiodic photonic crystals. *Physical Review B* **68** (2003).

114. Gauthier, R. C. & Mnaymneh, K. FDTD analysis of 12-fold photonic quasicrystal central pattern localized states. *Optics Communications* **264,** 78–88 (2006).

115. Wang, K. Light wave states in two-dimensional quasiperiodic media. *Physical Review B* **73,** 235122 (June 2006).

116. Maciá, E. Exploiting aperiodic designs in nanophotonic devices. *Reports on Progress in Physics* **75,** 036502 (2012).

117. Altug, H., Englund, D. & Vučković, J. Ultrafast photonic crystal nanocavity laser. *Nature Physics* **2,** 484–488 (2006).

118. El-Kady, I., Reda Taha, M. M. & Su, M. F. Application of photonic crystals in submicron damage detection and quantification. *Applied Physics Letters* **88,** 253109 (2006).

119. Fujiwara, T., Yamamoto, S. & de Laissardière, G. T. Band structure effects of transport properties in icosahedral quasicrystals. *Physical Review Letters* **71,** 4166–4169 (Dec. 1993).

120. Levi, L. *et al.* Disorder-Enhanced Transport in Photonic Quasicrystals. *Science* **332,** 1541–1544 (June 2011).

121. Schwartz, T., Bartal, G., Fishman, S. & Segev, M. Transport and Anderson localization in disordered two-dimensional photonic lattices. *Nature* **446,** 52–55 (2007).

122. Rockstuhl, C., Peschel, U. & Lederer, F. Correlation between single-cylinder properties and bandgap formation in photonic structures. *Optics letters* **31,** 1741–1743 (2006).

123. Lidorikis, E., Sigalas, M., Economou, E. N. & Soukoulis, C. Tight-binding parametrization for photonic band gap materials. *Physical review letters* **81,** 1405 (1998).

124. Della Villa, A. *et al.* Band Gap Formation and Multiple Scattering in Photonic Quasicrystals with a Penrose-Type Lattice. *Physical Review Letters* **94,** 183903 (May 2005).

125. Batten, R. D., Stillinger, F. H. & Torquato, S. Classical disordered ground states: Super-ideal gases and stealth and equi-luminous materials. *Journal of Applied Physics* **104,** 033504 (2008).

126. Torquato, S., Zhang, G & Stillinger, F. Ensemble theory for stealthy hyperuniform disordered ground states. *Physical Review X* **5,** 021020 (2015).

127. Torquato, S. (private communication).